Enhanced Solar Energy Harvesting by Metasurface Photoelectrodes

Ludwig Hüttenhofer

München 2022

Enhanced Solar Energy Harvesting by Metasurface Photoelectrodes

Ludwig Hüttenhofer

Dissertation
to obtain the doctoral degree of natural sciences (Dr. rer. nat.)
at the Faculty of Physics
of the Ludwig-Maximilians-Universität München

submitted by
Ludwig Hüttenhofer
from München

München, 26/11/2021

First referee: Prof. Dr. Stefan A. Maier
Second referee: Prof. Dr. Isabelle Staude
Date of oral examination: 26/01/2022

Verbesserte Nutzung von Sonnenenergie durch Metaoberflächen-Photoelektroden

Ludwig Hüttenhofer

Dissertation
zur Erlangung des Doktorgrades der Naturwissenschaften (Dr. rer. nat.)
an der Fakultät für Physik
der Ludwig-Maximilians-Universität München

vorgelegt von
Ludwig Hüttenhofer
aus München

München, den 26.11.2021

Erstgutachter: Prof. Dr. Stefan A. Maier
Zweitgutachter: Prof. Dr. Isabelle Staude
Tag der mündlichen Prüfung: 26.01.2022

Contents

List of Figures

List of Tables

List of Abbreviations

AE	anapole excitation
CE	counter electrode
CPD	contact potential difference
FDTD	finite difference time domain
HER	hydrogen evolution reaction
HOAE	higher oder anapole excitation
IPCE	incident-photon-to-current conversion efficiency
IQE	internal quantum efficiency
LR	lattice resonance
MFE	metasurface-to-film enhancement factor
OER	oxygen evolution reaction
PEC	photoelectrochemical
PEF	photo-enhancement factor
RE	reference electrode
SC	semiconductor
SCPC	semiconductor photocatalyst
SPV	surface photovoltage
WE	working electrode

Zusammenfassung

Optisch resonante Nanostrukturen haben die Entwicklung photonischer Anwendungen vorangetrieben, da sie in der Lage sind, Licht auf der Nanoskala stark zu konzentrieren. Weil dielektrische Resonatoren typischerweise unterhalb ihrer Bandlücke angeregt werden, um optische Verluste zu minimieren, blieb die Verwendung solcher Nanoantennenkonzepte zur Absorptionsverstärkung weitgehend unerforscht. Diese Arbeit erläutert die Entwicklung von Nanoantennen aus photokatalytischen Dielektrika und demonstriert deren verbesserte Lichtabsorption. Nach einer Darstellung des theoretischen Hintergrunds der nichtradiativen Anapolanregungen (AE) und der spezifischen, experimentellen Methoden dieser Arbeit, wird diese Grundidee von einzelnen Partikeln auf die photoelektrochemische Charakterisierung von Metaoberflächen-Elektroden aufskaliert.

Zunächst werden AE in einzelnen Nanoscheiben aus substöchiometrischem Titandioxid (TiO_{2-x}) eingesetzt. Die resultierende photokatalytische Verstärkung wird durch die Silberreduktionsreaktion auf TiO_{2-x} nachgewiesen. Mit der Möglichkeit, die optischen Eigenschaften von TiO_{2-x} durch die Konzentration von Sauerstoffleerstellen zu verändern, wird das Zusammenspiel zwischen dem komplexen Brechungsindex und der anapolunterstützten Feldkonzentration zur Absorptionsverbesserung diskutiert. Photoelektroden benötigen große Flächen mit eng beieinander liegenden Nanoresonatoren, um hohe chemische Ausbeuten zu erzielen. Daher folgt auf die Einzelpartikelstudie eine Untersuchung der Kopplungsmechanismen in rechteckigen Anordnungen von Nanoscheiben aus amorphen Galliumphosphid (a-GaP). Transmissionsexperimente zeigen, dass die maximale Absorption von sichtbarem Licht in a-GaP erreicht wird, wenn die Partikelperiodizität die spektrale Überlagerung der kollektiven Gitterresonanz mit der AE bedingt. Eine Analyse der Kopplung in ein- und zweidimensionalen Anordnungen mit polarisationsabhängigen Messungen sowie numerischen Simulationen ermöglicht es, zwischen Wechselwirkungen parallel und senkrecht zur Anregungspolarisationsachse zu unterscheiden und deren Stärke zu auszuwerten. Ausgehend von den optischen Eigenschaften kleinflächiger Anordnungen wird ein Verfahren zur Herstellung großflächiger a-GaP Photoelektroden mittels Stempel-Lithographie entwickelt. Dies ermöglicht kosteneffizienten und hohen Probendurchsatz, wobei die nanophotonischen Zustände präzise erhalten bleiben. Photoelektrochemische Messungen unter Wasserstoffentwicklungsbedingungen und Sonnenlicht zeigen eine Erhöhung des Gesamtphotostroms um 5,7 im Vergleich zu einem a-GaP Dünnschichtfilm.

Diese Arbeit bietet eine Anleitung für das photonische Design und die Herstellung von Photoelektroden mit nahezu vollständiger Nutzung des sichtbaren Sonnenlichts.

Summary

Optically resonant nanostructures accelerated the development of photonic applications, driven by their ability to strongly confine light on the nanoscale. Since dielectric resonators are typically operated below their bandgap to minimize optical losses, the usage of dielectric nanoantenna concepts for absorption enhancement has largely remained unexplored. This thesis explains the engineering of nanoantennas composed of photocatalytic dielectrics and demonstrates their increased light harvesting capability. After outlining the theoretical background of nonradiative anapole excitations (AEs) and the specific experimental methods applied in this thesis, this basic idea is upscaled from single particles to photoelectrochemical characterization of large-scale metasurface electrodes.

Initially, AEs are employed in single nanodisks of oxygen-vacancy-rich titanium dioxide (TiO_{2-x}). The arising photocatalytic enhancement is monitored using silver reduction reaction on TiO_{2-x}. With the freedom of changing the optical properties of TiO_{2-x} through tuning the abundance of oxygen vacancy states, the interplay between complex refractive index and the AE-assisted field confinement for absorption enhancement is discussed. Photocatalytic devices require large areas with closely spaced nanoresonators for sizable chemical yields. Therefore, the single particle study is followed by an investigation of coupling mechanisms in rectangular arrays of amorphous gallium phosphide (a-GaP) nanodisks that support the AE. Transmission experiments show that maximum visible light absorption by the a-GaP is achieved by tuning the array periodicities such the collective lattice resonance spectrally overlaps with the AE of a single particle. An analysis of coupling in one- and two-dimensional arrays with polarization-dependent measurements and numerical simulations allows to discriminate between coupling interactions parallel and perpendicular to the excitation polarization axis and evaluate their strengths. Familiarized with the optical properties of small-scale nanodisk arrays, a design procedure for large-scale nanofabrication of a-GaP photoelectrodes using imprint lithography is developed. With this, cost-effective, high sample throughput is achieved while retaining the precise signature of the engineered photonic states. Photoelectrochemical measurements under hydrogen evolution reaction conditions and sunlight illumination reveal the contributions of the respective resonances and demonstrate an overall photocurrent enhancement of 5.7, compared to an a-GaP thin film.

Overall, this thesis provides a manual for photonic design and fabrication of photoelectrodes with nearly full visible solar light harvesting capability.

"sometimes you measure a sample,
sometimes a sample measures you..."

Chapter 1

Introduction

1.1 Research Motivation

The discovery to use the energy stored in chemical bonds of fossil fuels established the beginning of the modern age. Nowadays, fossil fuels are under severe criticism owing to the negative environmental impact of their production and combustion [1] as well as clustering of market power in resource-rich regions. [2] The storage of energy in the chemical bonds of dihydrogen (H_2) constitutes an attractive alternative to fossil fuels: The "combustion" of H_2 in a fuel cell produces only water and the initial product for H_2 production, *i.e.* H_2O, is an globally abundant resource. Apart from the environmental aspects, H_2 as energy carrier surpasses fossil fuels in the conventional form of *e.g.* gasoline by means of gravimetric energy density by a factor of approximately three, as displayed in Figure 1.1. Current developments of liquid organic hydrogen carriers (LOHC) tackle the logistic challenges of transportation and storage of H_2 due to its relatively low volumetric energy density. [3, 4]

A crucial step towards a sustainable energy supply involving H_2 is its production. Current industrial mass scale production of H_2 is still based on fossil fuel combustion by steam-reforming of methane. [6] However, this fails to address an emission minimized energy supply scenario. The sun is the earths natural energy supplier, suggesting the combination of established photovoltaics with electrolysis. This two-stage solar to chemical energy conversion is an emerging technology, currently addressing the storage of excessive power into hydrogen. [7] The first-stage, solar-to-electric energy conversion efficiency $\eta_{S\rightarrow E}$ needs to be multiplied by the second stage electric-to-chemical conversion efficiency $\eta_{E\rightarrow C}$ to obtain the total device performance η_{tot}:

$$\eta_{\text{tot}} = \eta_{S\rightarrow E} \times \eta_{E\rightarrow C} \tag{1.1}$$

While extensive research on enhancing solar-to-electric energy conversion efficiency is conducted and truly delivers success on a fast pace, η_{tot} will always be limited by $\eta_{S\rightarrow E}$ and the high costs involved. [8] Furthermore, it is clear from thermodynamics that the transformation between different forms of energy ($S \rightarrow E \rightarrow C$) causes additional conversion losses.

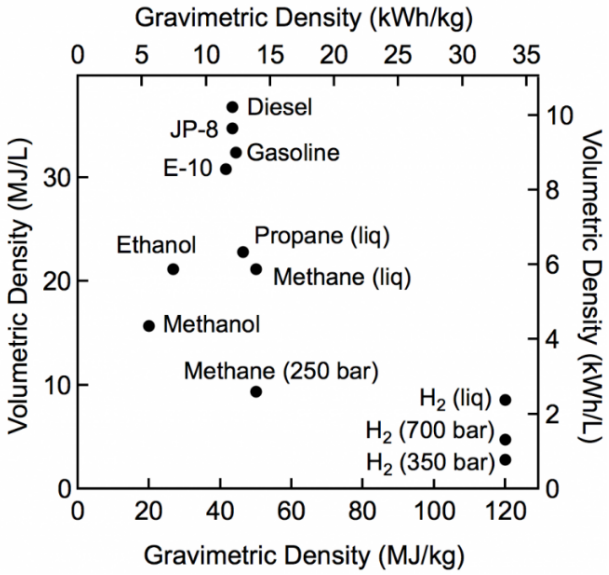

Figure 1.1: Energy storage per weight and volume of conventional fuels and dihydrogen (H_2) in gaseous and liquid phase. Figure taken from [5].

Therefore, it is obvious to invoke an opportunity to directly convert solar into chemical energy such:

$$\eta_{\text{tot}} = \eta_{S \rightarrow C} \tag{1.2}$$

This concept is provided by *photocatalysis*. According to the International Union of Pure and Applied Chemistry this process is defined by: [9]

"*a change in the rate of a chemical reaction or its initiation under the action of ultraviolet, visible or infrared radiation in the presence of a substance – the photocatalyst – that absorbs light and is involved in the chemical transformation of the reaction partners*".

Hereby, the photocatalyst is the crucial unit that acts as energy converter. Whereas the material constituting the photocatalyst is not specified, the first discovery of photocatalytic water splitting by Fujishima and Honda in 1972 [10] drew the attention to semiconductors: Oxygen evolution reaction was observed on a TiO_2 photoelectrode under UV irradiation. Semiconductors efficiently generate electron-hole pairs under absorption of light with minimized dissipation. This constituting the research field of *semiconductor photocatalysis*.

Figure 1.2 displays the research activity trend on photocatalysis from 1968 to present. The correlation with the crude oil price suggests that its volatility is the main driver for the research activity development, that reached a exponential increase in 1990. Together with the growing awareness of man-made climate change, this shows the necessity of an alternative, sustainable energy supply by "green hydrogen". In the context of this accelerating exploration, photocatalysis has frequently been reported as *the holy grail* for closing the carbon cycle. [11] However, the limited capability of established semiconductor photocata-

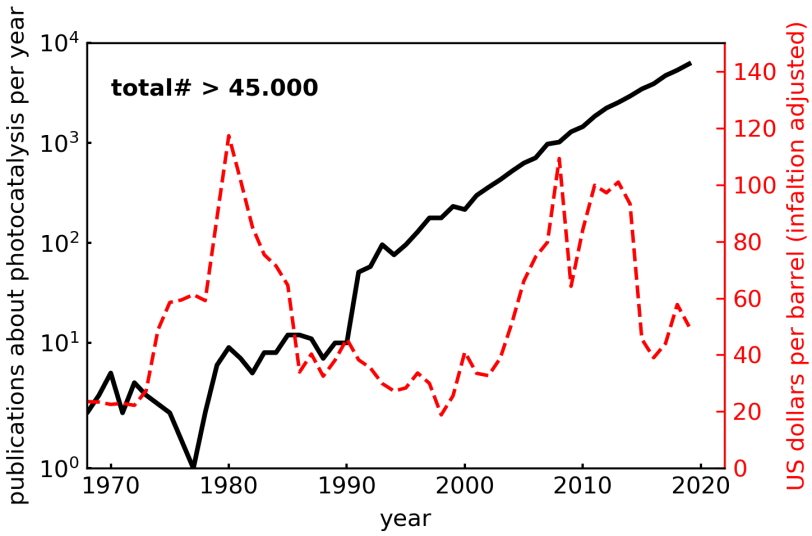

Figure 1.2: Publications about photocatalysis per year on a logarithmic scale together with the crude oil price. Data taken from www.webofknowledge.org

lysts to absorb visible sunlight is the main obstacle on the way to their commercial use. [12]

This work investigates how the absorption of semiconductor photocatalysts can be extended from UV light throughout the visible solar spectrum by means of dielectric, nanophotonic engineering. The following sections take the reader from the basics of semiconductor photocatalysis through fundamental limitations to this research work, providing a broad literature review at the level of materials optimization as well as at the level of similar studies on light trapping for energy conversion applications.

1.2 Principles of Semiconductor Photocatalysis

This section starts with the explanation of the fundamentals of semiconductor photocatalysis and consecutively elucidates the main efficiency loss mechanisms. From these, the focus is on the low semiconductor (SC) solar light absorption whose tackling is the main motivation of the thesis. Because the field is very broad and can also be treated from a more chemical perspective, kinetic aspects like surface properties of the catalyst-electrolyte interface are omitted. Much more, the section aims to concisely guide the reader to the main topic of the thesis, *i.e.* absorption enhancement of SC photocatalysts (SCPC) with nanophotonic engineering. A more complete treatment of the field can be found in references [13][14][15][16].

1.2.1 Fundamental Processes

To split a molecule of H_2O into H_2 and $½\,O_2$ a free energy change of $\Delta G = 237.2\,\mathrm{kJ/mol}$ is required, which corresponds to $q\Delta E^\circ = 1.23\,\mathrm{eV}$ per electron transferred. [13] In electrolysis, this energy is provided by an external voltage source, whereas in photocatalysis this is allocated by photons with a wavelength $\lambda < h \cdot c/q\Delta E^\circ \approx 1000\,\mathrm{nm}$. To convert the photon into potential energy, a SC with a bandgap $E_{\mathrm{gap}} > 1.23\,\mathrm{eV}$ can be employed, in which electron-hole pairs are excited across the valence and conduction band. Figure 1.3 a) depicts the photocatalytic conversion process. A photocatalyst particle being immersed in an electrolyte solution (here water) is irradiated by light with energy $h\nu$. If $h\nu > E_{\mathrm{gap}}$ the excited free charge carriers can diffuse the solid-liquid interface and either reduce $H^+ \rightarrow H_2$ or oxidize $OH^- \rightarrow O_2$. In the case of water splitting the reduction and oxidation reaction is frequently denoted as hydrogen (HER) and oxygen evolution reaction (OER), respectively. Eventually, the photon energy is stored in chemical form of molecular bonds.

In addition, the bandgap of the SC must not only exceed 1.23 eV, but the valence and conduction band edge energy also need to be aligned properly with the redox potential of the electrolyte. Figure 1.3 b) shows a band diagram of the of the solid-liquid interface. For a thermodynamically feasible charge carrier transfer from the SC to the electrolyte the band edge energies have to straddle the redox potential. This extra energy is called overpotential and causes that a suitable SC needs to exhibit a bandgap of 1.6-2.4 eV to effectively drive water splitting. [13]

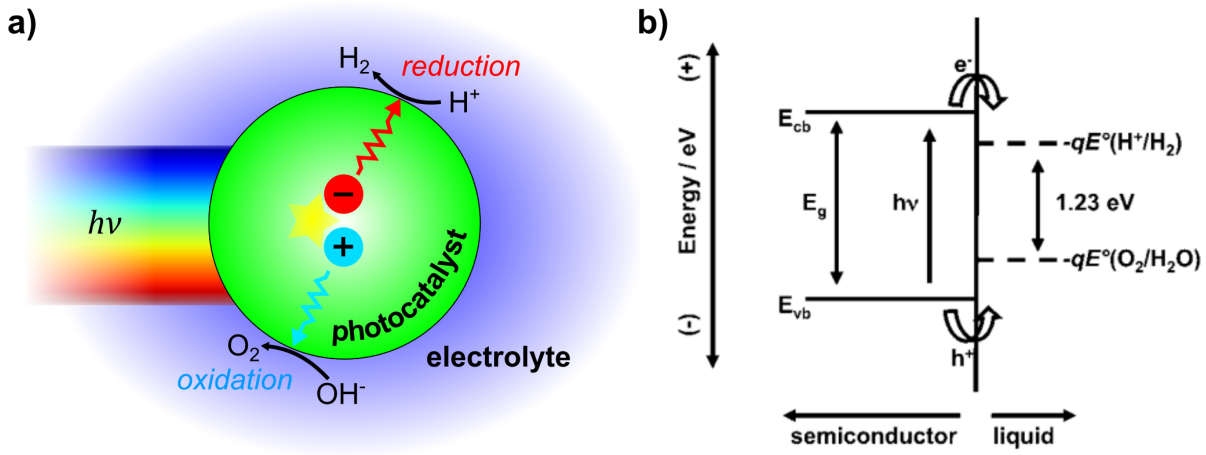

Figure 1.3: Scheme of the basic principle of semiconductor photocatalysis: a) The photocatalyst is immersed in an electrolyte solution. Upon irradiation of energy $h\nu$ excited charge carriers mitigate to the photocatalyst and trigger a reduction or oxidation reaction. Scheme is adapted from [17]. b) Band diagram of the interface of the semiconductor and the electrolyte (liquid). To enable water splitting the redox potential locates inside the valence and conduction band edges to facilitate charge transfer to the electrolyte. Figure is taken from [13].

1.2.2 Loss Mechanisms and Material Constrains

During the conversion from photon to chemical energy there are inherent losses that are responsible for the limitations of photocatalytic efficiencies. In general, the energy losses in the process stem either from a failure to utilize a photon in a desired redox process or a partial loss of its energy. [17] These mechanisms are illustrated in consecutive steps in Figure 1.4 a).

Below Bandgap Photons (1) Photons with insufficient energy to excite electrons over the bandgap are not absorbed by the SC and therefore cannot contribute to the process. This is a major loss channel for the utilization of solar energy. As an example, this accounts for the strong efficiency limitation of the most prominent SC photocatalyst TiO_2 having a bandgap of 3.2 eV and thus, not using over 95% of the sunlight. [18]

Thermalization (2) Photons with an energy exceeding the bandgap excite electrons to above conduction band states. The excess energy of the electron dissipates into thermal energy that is lost in the process. The theory behind the trade-off between reducing the bandgap energy and thermalization losses is described by the Shockley-Queisser limit, showing an instructive parallel to photovoltaic efficiency constrains. [19, 13]

Charge Carrier Recombination (3) Electron-hole pair must exhibit a sufficiently long diffusion length in order to not recombine during the migration to the solid-liquid interface. Typically, crystal defects and phonons act as trapping or scattering centers thereby favoring fast recombination in the bulk. This loss channel is difficult to optimize because the charge carrier diffusion length is an inherent material property. However, increasing the solid/liquid interface surface area constitutes a way to reduce these losses, which is an advantage of nano-sized photcatalysts. [20, 17]

Overpotential (4) As mentioned above, the overpotential is a necessity but it imposes an inherent loss channel. It can be minimized by exploring materials with suitable band edge alignments. [21]

Despite the mentioned energy losses, the SCPC has to exhibit high stability under the reaction conditions. The sum of these constrains leads to a highly nontrivial material choice of a suitable SCPC, as depicted in Figure 1.4 b). Transition metal oxides typically show good stability but have large bandgaps, leading to low visible light absorption and large overpotentials. Other oxides have unsuitable band positions such they can only drive one half reaction photochemically, like WO_3 and α-Fe_2O_3. The excellent SCPCs CdS and CdSe suffer from from photocorrosion, thereby degrading quickly under reaction conditions. [22, 16] In additional economic point of view, the SCPC should also be cost-effective, scalable and non-toxic. [23]

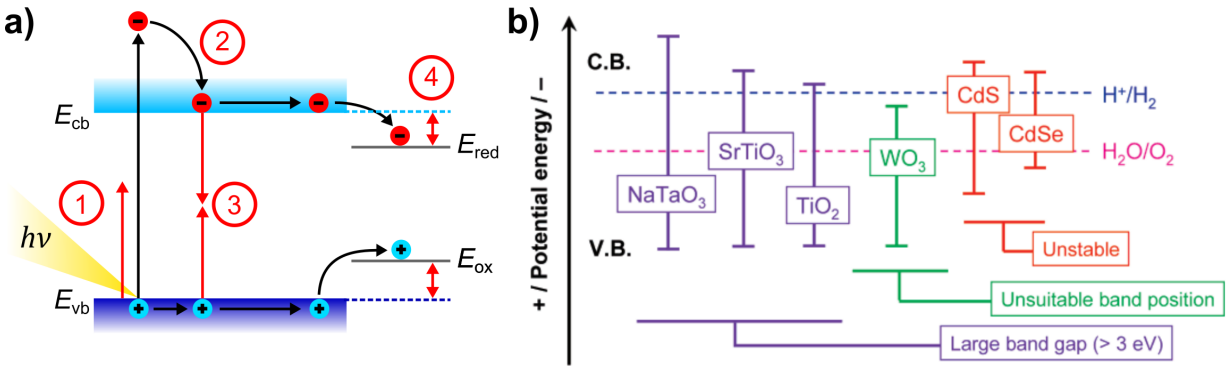

Figure 1.4: Band diagram elucidating loss channels during the conversion from photon to chemical energy: 1) Below bandgap photons 2) thermalization 3) charge carrier recombination and 4) overpotential. Figure adapted from [17]. b) Scheme for material constrains for an optimal semiconductor photocatalyst. Figure taken from [22].

1.2.3 Semiconductor Photocatalyst Optimization

In state-of-the-art research, there are four main approaches to create a good SC PC system, outlined in Figure 1.5. First, material bulk modification in terms of crystal structure or doping can extend the absorption edge of large bandgap SCs from the UV throughout the visible optical regime. [24, 25, 26, 27, 28, 29] In addition, n-doping (p-doping) leads to upward (downward) band banding in the SC at the solid/liquid interface, thereby allowing for unbiased charge carrier transfer and photovoltage generation. [13] Second, low energy photons can be used in large bandgap SCs by attaching nanoparticles with a plasmonic resonances in the visible to NIR. The generated charge carriers are injected into the SC conduction and valence bands such their potential energy is preserved for the catalytic reaction. Another effect is a local near-field enhancement at the nanoparticle-SCPC contact. However, new energy losses arise from dissipation in the plasmonic particle and a low charge carrier injection efficiency into the SC. [30, 31, 32, 33] Third, the addition of a protective coatings offers the possibility to stabilize sensitive SCPCs with otherwise suitable band structure properties. [34, 35, 36] This also called passivation layer – in most cases TiO_2 – can also induce a surface potential difference, thereby favoring charge transfer into the electrolyte, similar to the effect of material doping related band bending. [35, 34, 37] Fourth, A large field of research deals with the artificial synthesis of new materials to tailor the band structure, surface properties and stability for photocatalytic applications. [22, 23, 21, 38] Last, the method explored in this work lies within the approach of nanophotonic engineering, which aims for electromagnetic field confinement into the SCPCs. [39, 40] The following section describes previous studies of this field, which are based on dielectric material systems, and ultimately motivates the usage of nonradiating dielectric nanophotonics.

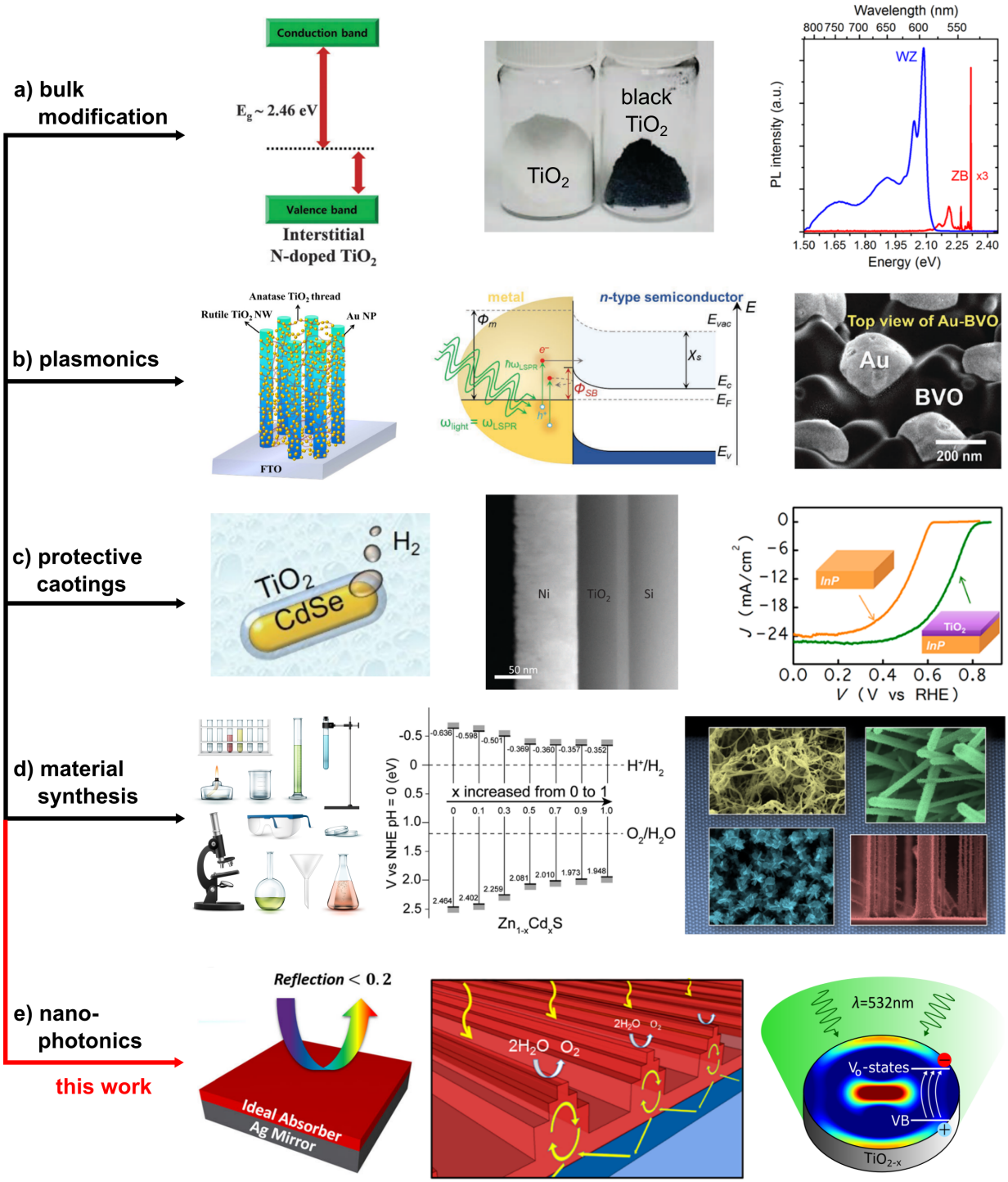

Figure 1.5: Current research routes for semiconductor photocatalyst optimization: a) Bulk material modification by doping, defect creation and crystal order change. b) Combination with plasmonic particles. c) Surface passivation of unstable photcatalysts with protective coatings. d) Material synthesis for bandgap and surface property engineering. e) Electromagnetic field confinement by nanophotonic engineering in semiconductor photocatalysts. Figures taken from: a) [28, 41, 42], b) [43, 30, 44], c) [36, 34, 37], d) [45, 46, 20] and e) [40, 39, 47]

1.3 Photonic Engineering in Photocatalytic Nanostructres

Solar energy is the most abundant source of energy and it is convenient to store it for high demand periods in the form of chemical bonds of hydrogen. However, chemically stable SCPCs for energy conversion typically have large bandgaps and thus, weak absorption of solar light. Figure 1.6 shows the absorption onsets of various SCPSs together with the terrestrial solar spectrum. Fe_2O_3 (haematite) is a broadband visible light absorber with a bandgap of $\approx 2.1\,\text{eV}$. However, the photocatalytic performance of the material is limited by its extremely short charge carrier diffusion diffusion length smaller than 5 nm. [48]. Cu_2O and GaP appear to be good absorbers with suitable band positions. However, both materials suffer from photocorrosion in aqueous electrolytes. [49, 34] In addition, GaP has an indirect bandgap and thus, weak absorption for $\lambda > 450\,\text{nm}$. Similarly, WO_3 has a bandgap of 2.6 eV with an absorption onset at 470 nm and no overpotential for the reduction reaction. [14] TiO_2 is a stable material under reaction conditions with suitable band positions for water splitting. But with a bandgap of 3.2 eV, only the UV portion of the solar spectrum is absorbed.

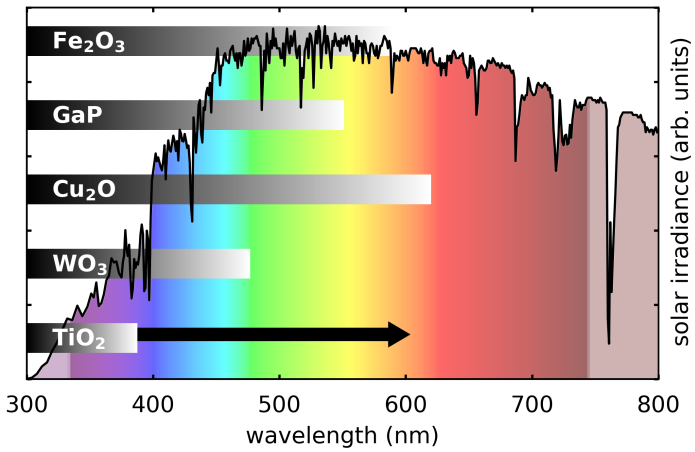

Figure 1.6: Terrestrial solar spectrum and absorption onsets of various SCPCs.

The application of photonic engineering aims for the enhancement and/or the extension of the absorption edge of SCPCs with weak solar light harvesting capabilities while maintaining the stability and the surface properties of the material. Instead of bulk modification or combination with plasmonic particles, here, the absorption increase is achieved by local enhancement of the electromagnetic field in the SCPC volume. It is instructive to consider the absorbed electrical power P_{abs} in an absorber volume V:

$$P_{\text{abs}} = \frac{\pi c}{\lambda} \cdot 2nk \cdot \int |E|^2 d\text{V} \tag{1.3}$$

with n and k being the real and imaginary part of the refractive index $\tilde{n}$, respectively, and E the electric field inside V. It is clear that P_{abs} is maximized by either increasing k, as done by bulk material modification, or increasing $|E|^2$. The latter can be achieved by photonic engineering:

Light Trapping by Interference in Ultrathin Films This strategy proposed by Dotan et al. [50] employs optical cavities comprising ultrathin absorbing films on reflective substrates serving as current collectors and back reflectors that give rise to interference between the forward- and backward-propagating waves, as illustrated schematically in Figure 1.7. This enhances the absorption by increasing the photon lifetime and thus, the electric field intensity in the film, reaching maximum absorption in the cavity resonance modes. For normal incidence on an ideal cavity the first resonance mode occurs in quarter-wave films, that is, when the film thickness (d) is a quarter of the wavelength λ of the light inside the film. Here, $\lambda = \lambda_0/\tilde{n}_2$, where λ_0 is the wavelength in vacuum and $\tilde{n}_2$ is the refractive index of the film. The quarter-wave condition takes into account the π phase shifts on reflection from the surface of the film and from the film/substrate interface, and another π phase shift on traversing the film forth and back. Consequently, the first-order reflection is in anti-phase with the higher-order reflections, thereby suppressing the intensity of the back-reflected light.

Moreover, the light intensity increases near the surface owing to constructive interference between the forward- and backward-propagating waves. In the referenced study, the absorbing film was Ti-doped α-Fe_2O_3, which is a chemically stable and visible light absorbing SCPC but small charge carrier diffusion length. Because the prepared photoanodes strongly absorb visible light within the ultrathin α-Fe_2O_3 film with thickness of 26 nm, rapid electron-hole recombination is suppressed and the photocurrent could be increased by 2.6 compared to a thin film without back-reflector. In addition, the photocurrent was also larger than using much thicker films.

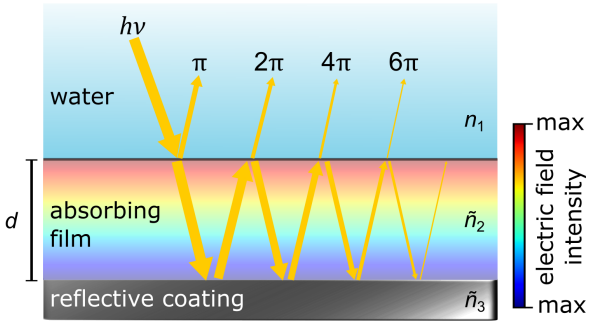

Figure 1.7: Schematic illustration of the light propagating in a quarter-wave ($d = \lambda/4$, for normal incidence) absorbing film on a back-reflector substrate. Figure adapted from [50].

Slow Photons in Photonic Crystals Three dimensional structuring of matter with a periodicity that is in the length scale of light waves is the signature of photonic crystals (Fig. 1.8 a). The arsing periodic dielectric contrast causes coherent Bragg diffraction which forbids light with certain energies to propagate through the material in a particular crystallographic direction. [51] This gives rise to a photonic band gap, as depicted in

the dispersion plot of Figure 1.8 b), whose spectral position of the edges depend on the periodicity of the photonic crystal. Light with energies within the photonic bandgap is reflected back. At the frequency edges of the photonic bandgap, photons propagate with strongly reduced group velocity, hence, they are called slow photons. Effectively, at these so called stop bands the propagation of light is transformed into standing waves. The frequency edges form either above or below the photonic bandgap, therefore denoted as blue and red edge, respectively. Slow photons from the red edge be used to for local electric field enhancement because – in contrast to the blue edge – the amplitude maxima of the standing wave localize in the high dielectric matter. If the energy of the slow photons from the red edge overlaps with the absorbance of the material, then an enhancement of the absorption can be expected. In 2006, Ozin et al. [52] proposed the application of this concept to anatase TiO_2 to enhance the UV absorption tail of the material. The TiO_2 photonic crystal with the red edge of the photonic bandgap tuned to 345 nm exhibited a two-fold enhancement of methylene blue degradation rate with respect to non-periodic nanocrystalline film.

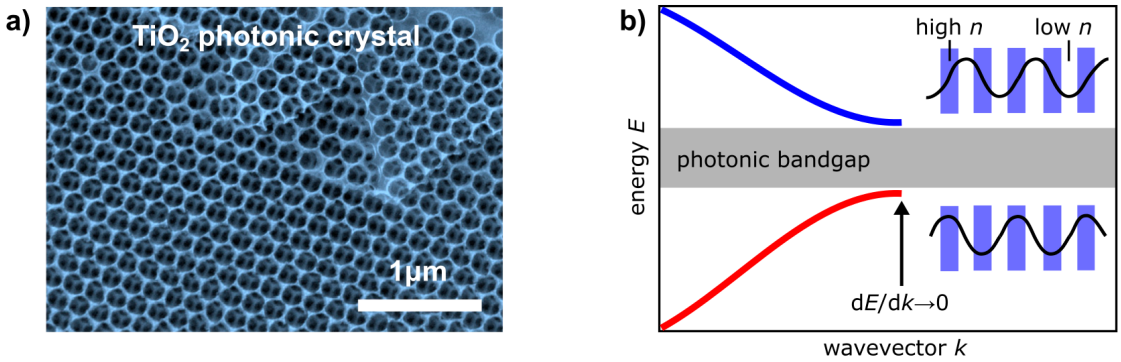

Figure 1.8: a) Field-emission scanning electron microscopy image of a TiO_2 inverse opal photonic crystal. Image taken from [53] b) Diagram of nonlinear dispersion around the photonic bandgap. As the group velocity approaches zero on the red edge the standing wave amplitude maxima localize within the high dielectric domains. Figure taken from [51].

Plasmonic Perfect Absorbers The first experimental proof of near-unity IR absorption in a metameterial was demonstrated by Landy et al. using a metallic electric ring ring resonator which is dielectrically spaced from a cut wire. [54] The variation of the geometry of this building blocks allows for manipulating resonances in electric permittivity and magnetic permeability independently. Therefore, it is possible to absorb both the incident electric and magnetic field and the spectral matching of both resonances leads to theoretically perfect absorption. Since then, a variety of perfect absorber material systems emerged. [55] One class of perfect absorbers are plasmonic based, in which metallic nanopartices (NPs) are are crafted onto a dielelectric film supported by a metallic mirror layer. Using the electric and magnetic dipolar resonances of periodically arranged plasmonic Au nanoparticels (NPs) on a Al_2O_3-Au layer stack, narrow near-IR absorption over 90% could be measured by Hao et al. [56]

By depositing Au NPs with an inhomogeneous size distribution onto a SiO_2 slab broadband visible light absorption was demonstrated in reference [58]. A similar plasmonic based broadband visible light perfect absorber system was realized as a photoanode by Tao et al. using TiO_2 as dielectric layer and maximize the absorption therein. [57] A scheme of the material stack is shown in Figure 1.9. With this technique, they achieved nearly full visible light absorption within a thin, low-loss TiO_2 layer and a 20-fold enhancement of photocurrent was observed under broad band illumination with $\lambda > 400\,\text{nm}$ compared to a bare film.

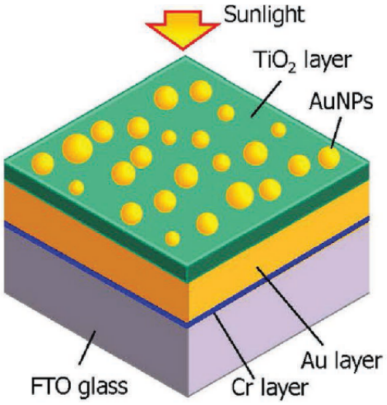

Figure 1.9: Material system of a plasmonic/TiO_2 based perfect absorber photoelectrode. Figure taken from [57].

Metasurfaces with Dipolar Resonances This ansatz strongly points towards the explored concept of this work and was investigated by Wu et al. [59] In their experimental demonstration periodic large arrays of sub-wavelength sized TiO_2 nanoblocks were fabricated, shown in Figure 1.10. These metasurfaces support fundamental electric and magnetic Mie-modes (see sec. 2.2), that cause spectrally tunable, norrow band far-field reflection in the visible regime, from which strong near-fields inside the particles are inferred. The TiO_2 of metasurfaces is than transformed to "black TiO_2" by reversible H^+-implantation, effectively setting the bulk complex refractive index to non-zero. Thus, the confined electric energy is absorbed by electron-hole pair generation. The enhanced photocatalytic effect is demonstrated by means of ≈ 18 times faster Ag^+ photoreduction rate from a $AgNO_3$ solution by the black TiO_2 metasurface under white light illumination compared to a black TiO_2 film. This method is described in more detail in section 3.3 and is also employed in the work presented in chapter 4.

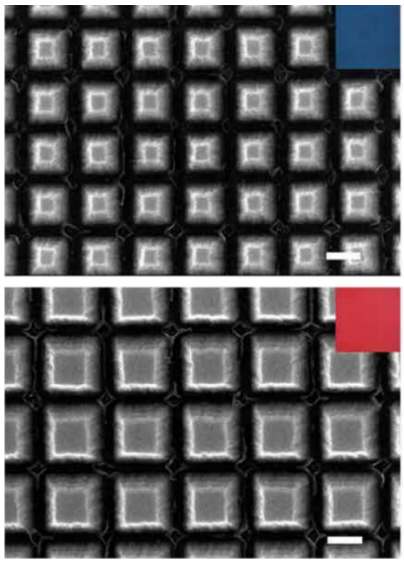

Figure 1.10: TiO_2 metasurfaces with increasing periodicity from top to bottom. The inset squares indicate the respective color of reflection. The scale bar corresponds to 200 nm. Figure taken from [59].

Nonradiative Nanophotonics If dielectric materials with high refractive index n are shaped into particles of diameter $d \approx \lambda/n$, strong optical response features occur due to the excitation of electric (ED) and magnetic dipole (MD) resonances. Figure 1.11 a) shows the simulated scattering cross section σ_{scat} of a silicon nanopillar with 200 nm radius and 260 nm height. [60] The total σ_{scat} is governed by the sum of the ED and MD resonances.

The orientation of the ED and MD moments inside the nanopillar under plane wave illumination are demonstrated in Figure 1.11 b). The spectral position of these photonic modes can be widely tuned by the refractive index, the geometry and the arrangement of particles, thereby allowing for tailoring a plethora of optical functionalities. [61, 62]

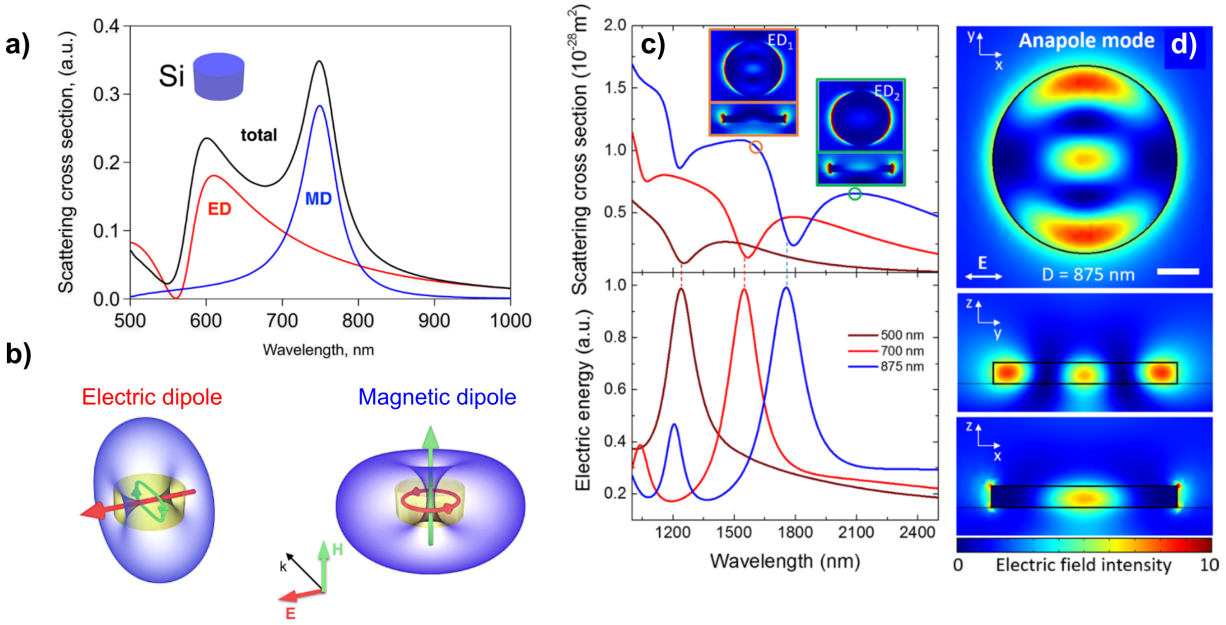

Figure 1.11: a) Simulated scattering cross section of a silicon nanopillar and its contribution from the electric (ED) and magnetic (MD) dipole resonance. b) Orientation of the ED and TD moments inside the nanodisk under plane wave illumination. Figure taken from [60]. c) The upper panel shows simulated scattering cross section of Ge nanodisks in the IR of different diameter with the corresponding electric energy spectra in the lower panel. The minima of scattering coincide with the maxima of electric energy. d) Simulated near-fields of the anapole excitation. Figure taken from [63].

A special case of optical responses of dielectric nanophotonic particles are nonradiative excitations. Whereas ED and MD resonances scatter most photon energy by radiative damping, nonradiative excitations enable the confinement of the incident light into subwavelength volumes. Two examples are bound-states-in-the-continuum and the anapole excitation (AE). [64, 65] The use of the AE for photocatalysis improvement constitutes the key approach of this work because of its characteristic property of light confinement into the particle volume. Figure 1.11 c) shows the simulated σ_{scat} spectra of Ge nanodisks with different radii together with the electric energy $W_{\mathrm{E}} = \frac{n^2}{2} \int |E|^2 dV$. [63] The minimum of σ_{scat} corresponds to a maximum of W_{E} and the spectral position of these extrema is highly tunable by the nanodisk diameter. Figure 1.11 d) displays the simulated electric near-field intensity at the AE with linearly x-polarized excitation and illustrates the $|E|^2$ maxima inside the Ge nanodisk in contrast to the ED resonances, where the electric field is confined only at the surface. The physical origin of the AE will be outlined in detail in chapter 2.2. Considering equation 1.3, it becomes obvious that the AE related electric

field enhancement can be employed to increase P_{abs} in wavelength regimes, in which the SCPC has low values of k, *i.e.* weak absorption. One important note has to be made: If $k = 0$, no energy is absorbed. This implies that the proposed approach is *not* capable to turn a fully transparent material absorbtive. Much more, the use of the AE is suitable to enhance light harvesting in materials with weak absorption onsets in the visible, *e.g.* by an indirect bandgap and defect or doping related electronic transitions.

In addition, nanostructuring of SCPCs comes along with further advantages for photocatalysis, demonstrated in Figure 1.12. As explained in section 1.2, photoexcited charge carriers need to migrate from their excitation site to the SCPC surface to be available for a chemical reaction. Their ability to migrate is limited by the diffusion length l_{d}, which is an inherent material property with typical values from 5-50 nm. [15, 66, 30] This is the reason why increasing the SCPC thickness absorption enhancement for overall absorption enhancement is useless: Charge carriers photoexcited outside the near surface volume limited by l_{d} (indicated by the dark green area in Fig. 1.12) will recombine before reaching the surface. A nanodisk geometry increases the probability for charge carriers to reach the surface within l_{d} and before recombination. Specifically, the AE absorption enhancement in a nanodisk can provide the same overall absorption as a muliple times thicker film but most volume is near surface. A further advantage is the increase of the absolute surface area and thus a denser loading of reactive sites per unit area.

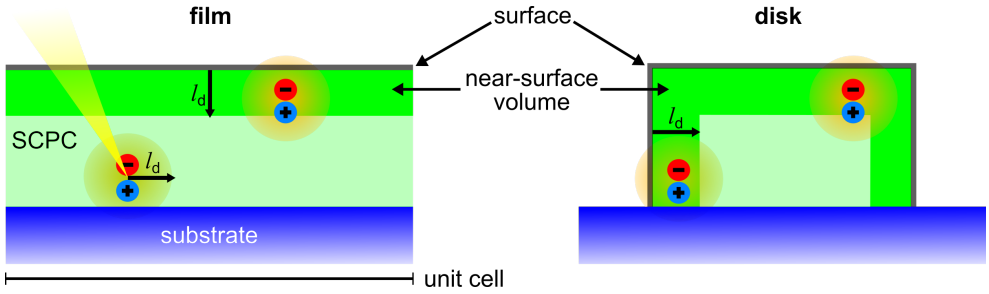

Figure 1.12: Scheme of charge carrier diffusion in the cross sections of left) a planar SCPC thin film and right) a nanodisk on a unit cell scale. The charge carriers need to reach the SCPC surface within their diffusion length l_{d} which is facilitated with a higher probability by the nanodisk. Thus, l_{d} limits the near-surface volume.

Chapter 2

Theory

The last chapter explained how non-radiative nanophotonics can be applied in the frame of semiconductor photocatalysis. The following chapter goes into more detail of light propagation in nanophotonic particles. First, a numerical method is outlined which served as the main tool for the design of the nanoresonators and conclusions about the internal photonic modes. Second, the simulation results are compared to first principle calculations to reveal the anapole condition in a nanosphere and -disk.

2.1 FDTD-Simulations

In this research work, the objects under investigation typically have similar or smaller dimensions as the wavelength of the probing light. For this reason, the laws of macroscopic optics cannot be fully applied. Furthermore, light propagation through microstructured matter with inhomogeneous optical properties cannot trivially be calculated by Maxwell's equations. This is why numerical approximations are necessary which are provided by finite difference time domain (FDTD) simulations, whose basic principle is outlined now after reference [67].

Mathematical Background of FDTD

The task is to solve the scalar wave equation, for simplicity in one dimension,

$$\frac{\partial^2 u}{\partial t^2} = c^2 \frac{\partial^2 u}{\partial x^2} \tag{2.1}$$

with $u = u(x,t)$ being the propagating wave solutions in $+x$ and $-x$ direction. The solution to this equations are well known, but their explicit form is unpractical for computational solving of electromagnetic propagation in complex structures of matter. The method of finite differences is based on the dicretization of time and space, and can be undertood by considering a Taylor's series expansion of $u(x, t_\mathrm{n})$ about the space point x_i to the space

point $x_\mathrm{i} + \Delta x$, keeping time fixed at t_n:

$$u(x_\mathrm{i}+\Delta x)\Big|_{t_\mathrm{n}} = u\Big|_{x_\mathrm{i},\,t_\mathrm{n}} + \Delta x \cdot \frac{\partial u}{\partial x}\bigg|_{x_\mathrm{i},\,t_\mathrm{n}} + \frac{(\Delta x)^2}{2} \cdot \frac{\partial^2 u}{\partial x^2}\bigg|_{x_\mathrm{i},\,t_\mathrm{n}} + \frac{(\Delta x)^3}{6} \cdot \frac{\partial^3 u}{\partial x^3}\bigg|_{x_\mathrm{i},\,t_\mathrm{n}} + \frac{(\Delta x)^4}{24} \cdot \frac{\partial^4 u}{\partial x^4}\bigg|_{\xi_1,\,t_\mathrm{n}} \tag{2.2}$$

The same is carried out for $x_\mathrm{i} - \Delta x$ and the sum of $u(x_\mathrm{i} + \Delta x)\big|_{t_\mathrm{n}}$ and $u(x_\mathrm{i} - \Delta x)\big|_{t_\mathrm{n}}$ reads in a rearranged form:

$$\frac{\partial^2 u}{\partial x^2}\bigg|_{x_\mathrm{i},\,t_\mathrm{n}} = \frac{u^\mathrm{n}_{\mathrm{i}+1} - 2u^\mathrm{n}_\mathrm{i} + u^\mathrm{n}_{\mathrm{i}-1}}{(\Delta x^2)} + O\left[(\Delta x^2)\right] \tag{2.3}$$

arriving at the space derivative of $u(x,t)$ of equation 2.1 with substitution of $u(x_\mathrm{i} \pm \Delta x) \rightarrow u_{\mathrm{i}\pm1}$ due to discretization of space. Equivalently, the time derivative is given by:

$$\frac{\partial^2 u}{\partial t^2}\bigg|_{x_\mathrm{i},\,t_\mathrm{n}} = \frac{u^{\mathrm{n}+1}_\mathrm{i} - 2u^\mathrm{n}_\mathrm{i} + u^{\mathrm{n}-1}_\mathrm{i}}{(\Delta t^2)} + O\left[(\Delta t)^2\right] \tag{2.4}$$

Inserting both derivatives into equation 2.1, neglecting the Taylor series reminder and solving for the latest value of u at grid point i, one obtains:

$$u^{\mathrm{n}+1}_\mathrm{i} \cong (c\Delta t)^2 \left(\frac{u^\mathrm{n}_{\mathrm{i}+1} - 2u^\mathrm{n}_\mathrm{i} + u^\mathrm{n}_{\mathrm{i}-1}}{(\Delta x)^2}\right) + 2u^\mathrm{n}_\mathrm{i} - u^{\mathrm{n}-1}_\mathrm{i} \tag{2.5}$$

This is a fully explicit second-order accurate expression for $u^{\mathrm{n}+1}_\mathrm{i}$ in that all wave quantities on the right-hand side are known; that is, they were obtained during the previous time steps, n and n−1. Repetition of equation 2.5 over the problem space constitutes the numerical FDTD solution of the scalar wave equation.

A practical implementation of a set of finite-difference equations for the time dependent Maxwell's curl equations was introduced by Kane S. Yee in 1966 for lossless media. [68] Due to its mathematical robustness modern simulation softwares are still based on his method, which can be summarized after reference [67] as follows:

1. The Yee algorithm solves for both electric and magnetic field in time and space using coupled Maxwell's curl equations, rather than solving for the electric (or magnetic) field alone with a wave equation.

2. As illustrated in Figure 2.1 a), the Yee algorithm centers its $\vec{E}$ and $\vec{H}$ components in 3D space so that every $\vec{E}$ component is surrounded by four circulating $\vec{H}$ components and vice versa.

3. As depicted in 2.1 b), the Yee algorithm also centers its $\vec{E}$ and $\vec{H}$ components in time, in what is termed a *leapfrog* arrangement. All of the $\vec{E}$ computations in the modeled space are completed and stored in memory for a particular time point using previously stored $\vec{H}$ data. Then, all of the $\vec{H}$ computations in the space are completed and stored in memory using the $\vec{E}$ data just computed and so on. This process continues until time stepping is concluded.

Following this fundamental basis any function $u(\mathrm{i}\Delta x, \mathrm{j}\Delta y, \mathrm{k}\Delta z) = u^{\mathrm{n}}_{\mathrm{i,j,k}}$ can be evaluated at a discrete point in the grid and at a discrete time, where Δx, Δy and Δz are, respectively the lattice space increments in the x, y and z coordinate directions, and i, j and k are integers.

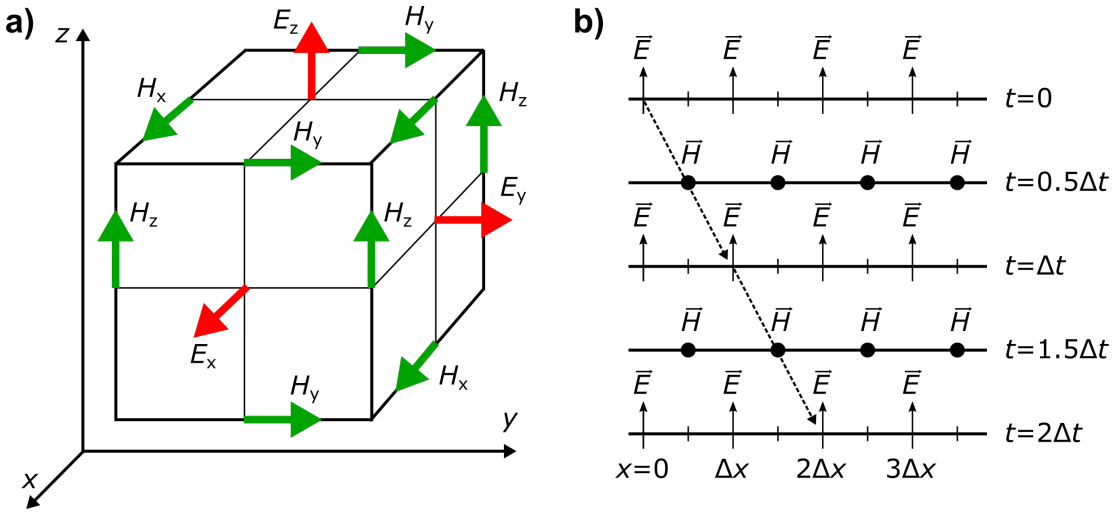

Figure 2.1: Schematic presentation of the Yee algorithm: a) Position of electric (red) and magnetic (green) field vector components about a cubic cell of the Yee space lattice. [67] Figure adapted from [68]. b) Space-time chart of the Yee algorithm for a one-dimensional wave propagation example showing the use of central differences for the space derivatives and leapfrog for the time derivatives. Figure adapted from [67].

One on of the greatest challenges of the FDTD method has been the efficient and accurate solution of electromagnetic wave interaction problems in unbounded regions. [67] For such problems, an absorbing boundary condition must be introduced to rule out unphysical reflections from the simulation region boundaries. The most common method of a highly effective absorber-material was introduced by Berenger in the form of perfectly matched layer (PML) boundary conditions. [69] The principle can be explained by considering a transversal electric z-polarized plane wave propagating through a lossless half-space (1) with angular frequency ω, impinging on a lossy half space (2) with electric conductivity σ and magnetic loss σ^* at an angle θ relative to normal incidence. Enforcing the continuity of tangential fields across the half space interface leads to the expression of the reflection coefficient Γ:

$$\Gamma = \frac{\frac{\beta_{1_x}}{\omega\epsilon_1} - \frac{\beta_{2_x}}{\omega\epsilon_2(1+\sigma/i\omega\epsilon_2)}}{\frac{\beta_{1_x}}{\omega\epsilon_1} + \frac{\beta_{2_x}}{\omega\epsilon_2(1+\sigma/i\omega\epsilon_2)}} \tag{2.6}$$

with

$$\beta_{1_x} = k_1 \cos\theta \qquad \text{half space 1} \tag{2.7}$$

$$\beta_{2_x} = \left((k_2)^2(1+\sigma/i\omega\epsilon_2)(1+\sigma^*/i\omega\mu_2) - (\beta_{2_y})^2\right)^{1/2} \qquad \text{half space 2} \tag{2.8}$$

For normal incidence ($\theta = 0$) and introducing the impedance η_i the reflection coefficient reduces to:

$$\Gamma = \frac{\eta_1 - \eta_2}{\eta_1 + \eta_2} \tag{2.9}$$

By setting $\epsilon_1 = \epsilon_2$ and $\mu_1 = \mu_2$ and further enforce the condition

$$\sigma^*/\mu_1 = \sigma/\epsilon_1 \rightarrow \sigma^* = \sigma\mu_1/\epsilon_1 = \sigma(\eta_1)^2 \tag{2.10}$$

leads to $\Gamma = 0$, a reflectionless half space interface for normal incidence. It can also be shown that the propagation through half space 2 is dispersion free. [67]

To achieve minimum boundary reflections from oblique incident waves, Berenger introduced the field-splitting modification of Maxwell's equations. The idea is the splitting of the incident wave into its parallel and perpendicular components, thus reestablishing minimized reflection as from normally incident waves. Whereas this is the basis of PML boundary conditions, further optimization methods have been developed, which are well explained in reference [67].

Usage of FDTD

The FDTD simulations used in this work were carried out with the software *Lumerical FDTD Solutions*. Although its FDTD implementation has been extensively optimized to address modern computational capabilities and user requirements, it still based on the previously explained principles of Yee's algorithm. In practice of this work, a simulation setup consist of five basic elements that are also visualized in Figure 2.2:

FDTD region A 3D space that is spatially discretized in to $(\Delta x)^3$. The size of Δx determines the accuracy of the results but also strongly affects the simulation time.

Structures The objects under investigation are placed into the FDTD region and resemble the experimental setup. Each substructure has to be specified with regard to its geometry and optical properties, *i.e.* its complex refractive index $\tilde{n}$.

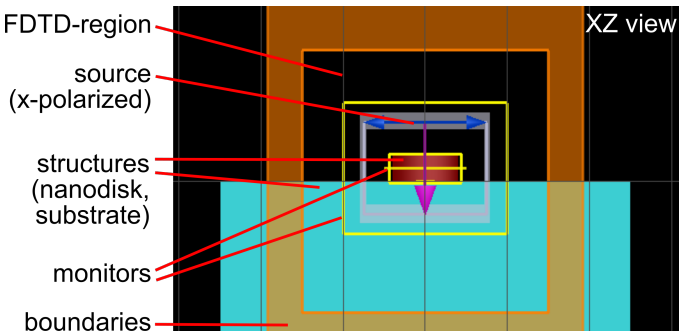

Figure 2.2: Side view demonstration of a typical FDTD setup for the simulation of scattering and absorption cross-sections for a nanodisk (red) on an SiO_2 substrate (blue).

Source To simulate electromagnetic propagation a light source is implemented in the FDTD region. In the simplest case, this is provided by a plane wave source with a given frequency. If a spectral dependence of the results (*e.g.* a spectrum) is required the simulation is carried out for multiple frequencies.

Monitors To calculate the optical response of the structures one needs to define spaces in the FDTD region in which the electromagnetic field of the volume elements is evaluated. These 2D or 3D spaces are monitors and provide the simulation output by visualizing electromagnetic near-fields and transmitted energies that in turn reveal the optical response by the structures.

Boundaries As previously explained, these regions limit the FDTD space and are either chosen as PML for single particle analysis or periodic for simulations of infinite arrays.

There are two specific advantages using FDTD in nanophotonic research:

First, simulations enable the design of nanostructures with desired optical responses without a primary need for fabrication of samples. This is especially useful if the parameter space for the nanostructure geometry design is rather unexplored. FDTD facilitates a strong limitation if this parameter space and therefore reduces fabrication effort, which otherwise is extensively time and resource consuming. However, an experimental validation of the simulated results is required. They can differ significantly because of inadequate resembling of the experimental conditions, uncertainties of the refractive index input data and over-idealization of the experimental system, *i.e.* a plane wave source, sharp edges of structure primitives, perfect material interfaces etc.
Second, once a good agreement between simulation and experiment is achieved, FDTD allows for the instructive connection between macroscopic, measurable quantities (*e.g.* scattering, transmission) and their microscopic origin from the electromagnetic near-fields inside the nanostructure, which cannot be accessed by simple microscopy due to the diffraction limit. One method to measure these near-fields is scanning near-field optical microscopy (SNOM). [70] However, this is often incompatible with an arbitrary sample geometry.

Figure 2.3 demonstrates how the mentioned advantages are implemented in the conception of the research projects of this work. A hypothesis or idea is to be verified experimentally and eventually should be realized for an application. The verification requires the measurement of a fabricated sample whose design can be assessed with FDTD. It is important to determine in advance a comparative quantity that can be simulated and experimentally resembled adequately, which was typically scattering or transmission spectra in this work. Once this quantity reaches sound agreement between simulation and measurement, it is justified to draw conclusions from the macroscopic signal to the internal electromagnetic modes of the nanoparticle that are responsible for the optical response. After this validation one can proceed to applications or iterate for further optimization of the desired optical properties.

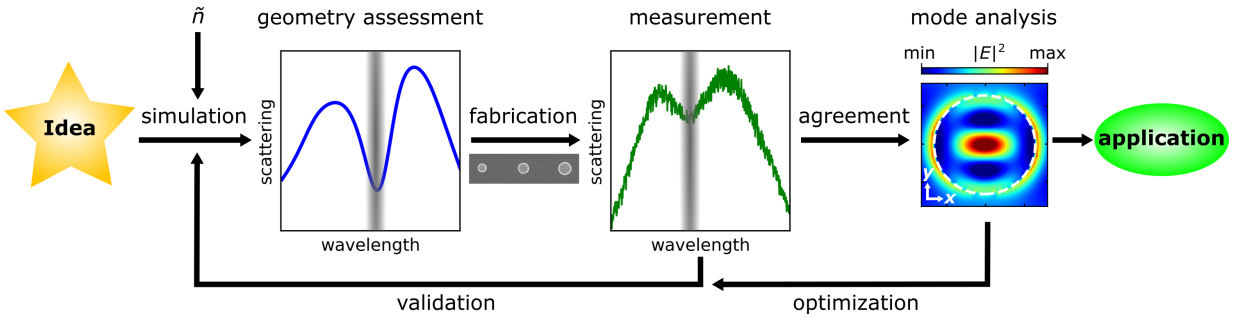

Figure 2.3: Chart presenting a typical workflow for project development as applied in this work with the example of scattering spectra as comparative quantity between simulation and measurement.

2.2 From Mie-Theory to the Anapole State

The anapole state is a nonradiative excitation produced by the intricate interplay of multiple photonic modes inside a illuminated particle and their destructive interference of the far-field scattering. [65] The following derivation demonstrates that the anapole state is inherent from first principle calculations of the optical response of a spherical particle. This formalism was established by Gustav Mie in 1908 [71] for metallic particles, but can be applied without loss of generality for different refractive indices of the particle and surrounding medium. With this approach, it is demonstrated that the condition for the anpole state is fulfilled in a dielectric sphere, but an experimental detection by the far-field scattering is obstructed due to the scattering from superposing higher order electric and magnetic resonances. This constrain could be overcome by changing the particle geometry from sphere to a flat disk, whose response is dominated by lowest order electric dipolar and toroidal modes. However, Mie-Theory becomes even more complex for non-spherical particles. Fortunately, with the help of multipolar decomposition and scattering spectra from FDTD simulations, it will be shown that the anapole condition is also fulfilled in a disk geometry with a unambiguous, experimentally detectable scattering signal. Ultimately, the state is associated with a strong enhancement of the internal electric fields, which in turn leads to increased absorption and thus, higher photocatalytic activity of the material.

The outlined framework follows the comprehensive derivation shown by Craig F. Bohren and Donald R. Huffman. [72] If not familiar with this topic, the reader is recommended to revisit the first chapters of this book. The goal of the following calculations is to determine the internal and scattered fields ($\boldsymbol{E}_{\mathrm{int}}$ and $\boldsymbol{E}_{\mathrm{scat}}$, respectively) of a spherical, lossless and dielectric particle upon irradiation of a plane, incident wave $\boldsymbol{E}_{\mathrm{i}}$, as depicted in Figure 2.4. The foundation for the solution is laid by the macroscopic Maxwell equations

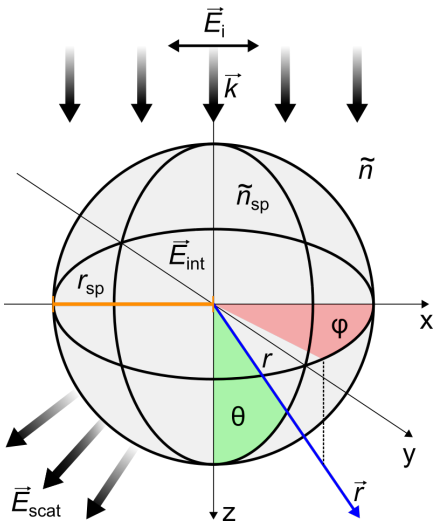

Figure 2.4: Spherical coordinate system centered on a sphere of radius r_{sp} and refractive index $\tilde{n}_{sp}$. The surrounding medium has a refractive index of $\tilde{n}$. The incident, internal and scattered electric fields are denoted as E_i, E_{int} and E_{scat}, respectively.

in non-dispersive, linear and isotropic media with time harmonic fields:

Gauss' law of electricity: $$\vec{\nabla} \cdot \vec{D} = \rho \tag{2.11}$$

Gauss' law of magnetism: $$\vec{\nabla} \cdot \vec{B} = 0 \tag{2.12}$$

Law of Faraday: $$\vec{\nabla} \times \vec{E} = i\omega\mu\vec{H} \tag{2.13}$$

Law of Ampère: $$\vec{\nabla} \times \vec{H} = -i\omega\epsilon\vec{E} \tag{2.14}$$

Permittivity: $$\epsilon = \epsilon_0\epsilon_r \tag{2.15}$$

Permeability: $$\mu = \mu_0\mu_r \tag{2.16}$$

with the wave equation:

$$\vec{\nabla}^2\vec{E} + \frac{\omega^2}{c^2}\epsilon\vec{E} = 0 \tag{2.17}$$

where ω is the angular frequency and c the speed of light. In general, all field solutions $\vec{E}$ must satisfy the wave equation and need to be divergence free:

$$\left(\vec{\nabla}^2 + \frac{\omega^2}{c^2}\epsilon\right)\vec{E} = 0 \tag{2.18}$$

$$\vec{\nabla} \cdot \vec{E} = 0 \tag{2.19}$$

To avoid a direct solution of the full vectorial wave equation, the problem is reduced to solving a scalar wave equation term. Towards this end, a vector field $\vec{M}$ is constructed from a scalar field ψ multiplied with the arbitrary vector $\vec{b}$:

$$\vec{M} = \vec{\nabla} \times (\vec{b} \cdot \psi) \tag{2.20}$$

Through this construction $\vec{M}$ also satisfies the vectorial wave equation:

$$\left(\vec{\nabla}^2 + \frac{\omega^2}{c^2}\epsilon_\mathrm{i}\right)\vec{\nabla}\times(\vec{b}\cdot\psi) \stackrel{!}{=} 0 \tag{2.21}$$

$$\rightarrow \vec{\nabla}\times\left[\vec{b}\cdot\underbrace{\left((\vec{\nabla}^2\psi + \frac{\omega^2}{c^2}\epsilon_\mathrm{i}\psi\right)}_{\stackrel{!}{=}0}\right] \stackrel{!}{=} 0 \tag{2.22}$$

It is convenient to solve this problem in rotational symmetry, so $\vec{b}$ is chosen as the radial vector $\vec{r}$ leading to the scalar wave equation in spherical coordinates:

$$\frac{1}{r^2}\frac{\partial}{\partial r}\left(r^2\frac{\partial\psi}{\partial r}\right) + \frac{1}{r^2\sin\theta}\frac{\partial}{\partial\theta}\left(\sin\theta\frac{\partial\psi}{\partial\theta}\right) + \frac{1}{r^2\sin\theta}\frac{\partial^2\psi}{\partial^2\phi} + \frac{\omega^2}{c^2}\epsilon_\mathrm{i}\psi = 0 \tag{2.23}$$

ψ can be solved by separation of variables:

$$\psi(r,\theta,\phi) = R(r)\cdot\Theta(\theta)\cdot\Phi(\phi) \tag{2.24}$$

Inserting equation 2.24 into 2.23 yields the product of three separate equations for r, ϕ, and θ:

$$\psi_\mathrm{emn} = \cos(m\phi)\cdot P_\mathrm{n}^\mathrm{m}(\cos\theta)\cdot z_\mathrm{n}(kr) \tag{2.25}$$

$$\psi_\mathrm{omn} = \sin(m\phi)\cdot P_\mathrm{n}^\mathrm{m}(\cos\theta)\cdot z_\mathrm{n}(kr) \tag{2.26}$$

with P_n^m being the associated Legendre function of the first kind with degree n and order m and the spherical Bessel functions z_n, which are specified later. The scalar fields can now be used to generate vector spherical harmonics:

$$\vec{M}_\mathrm{emn} = \vec{\nabla}\times(\vec{r}\psi_\mathrm{emn}) \tag{2.27}$$

$$\vec{M}_\mathrm{omn} = \vec{\nabla}\times(\vec{r}\psi_\mathrm{omn}) \tag{2.28}$$

$$\vec{N}_\mathrm{emn} = \frac{\vec{\nabla}\times\vec{M}_\mathrm{emn}}{k} \tag{2.29}$$

$$\vec{N}_\mathrm{omn} = \frac{\vec{\nabla}\times\vec{M}_\mathrm{omn}}{k} \tag{2.30}$$

With this, an x-polarized incident plane wave in spherical coordinates

$$\vec{E}_\mathrm{i} = E_0 e^{ikr\cos\theta}\cdot\vec{e}_\mathrm{x} \tag{2.31}$$

with

$$\vec{e}_x = \sin\theta\,\cos\phi\,\vec{e}_r + \cos\theta\,\cos\phi\,\vec{e}_\theta - \sin\phi\,\vec{e}_\phi \tag{2.32}$$

can be expanded into vector spherical harmonics:

$$\vec{E}_{\mathrm{i}} = \sum_{m=0}^{\infty}\sum_{n=0}^{\infty}\left(B_{\mathrm{emn}}\vec{M}_{\mathrm{emn}} + B_{\mathrm{omn}}\vec{M}_{\mathrm{omn}} + A_{\mathrm{emn}}\vec{N}_{\mathrm{emn}} + A_{\mathrm{omn}}\vec{M}_{\mathrm{omn}}\right) \tag{2.33}$$

The boundary condition between sphere and surrounding medium imposes to following continuity equation:

$$(\vec{E}_{\mathrm{i}} + \vec{E}_{\mathrm{s}} + \vec{E}_{\mathrm{int}}) \times \vec{e}_r = 0 \tag{2.34}$$

and analogously for $\vec{H}_{i,s,int}$. The boundary conditions, the orthogonality of the vector harmonics, and the expansion of the incident field dictate the form of the expansions for the incident and scattered field as well as the field inside the sphere:

$$\vec{E}_{\mathrm{i}} = \sum_{n=0}^{\infty} E_{\mathrm{n}}\left(\vec{M}^{(1)}_{\mathrm{o1n}} - i\vec{N}^{(1)}_{\mathrm{e1n}}\right) \tag{2.35}$$

$$\vec{E}_{\mathrm{scat}} = \sum_{n=0}^{\infty} E_{\mathrm{n}}\left(ia_{\mathrm{n}}\vec{N}^{(3)}_{\mathrm{e1n}} - b_{\mathrm{n}}\vec{M}^{(3)}_{\mathrm{o1n}}\right) \tag{2.36}$$

$$\vec{E}_{\mathrm{int}} = \sum_{n=0}^{\infty} E_{\mathrm{n}}\left(c_{\mathrm{n}}\vec{M}^{(1)}_{\mathrm{o1n}} - id_{\mathrm{n}}\vec{N}^{(1)}_{\mathrm{e1n}}\right) \tag{2.37}$$

The superscript (1) denotes the use of $j_n(kr)$ as spherical Bessel function in ψ, (3) indicates the use of the spherical Hankel function $h^{(1)}_{\mathrm{n}}(kr)$ and $E_{\mathrm{n}} = i^{\mathrm{n}}E_0(2\mathrm{n}+1)/\mathrm{n}(\mathrm{n}+1)$. Introducing the size parameter $x = kr_{\mathrm{sp}} = 2\pi\tilde{n}_{\mathrm{sp}}r_{\mathrm{sp}}/\lambda$ with the relative refractive index $m = \tilde{n}_{\mathrm{sp}}/\tilde{n}$ the expansion coefficients for the scattered field are given by:

$$a_{\mathrm{n}} = \frac{m^2 j_{\mathrm{n}}(mx)\,[xj_{\mathrm{n}}(x)]' - j_{\mathrm{n}}(x)\,[mxj_{\mathrm{n}}(mx)]'}{m^2 j_{\mathrm{n}}(mx)\left[xh^{(1)}_{\mathrm{n}}(x)\right]' - h^{(1)}_{\mathrm{n}}(x)\,[mxj_{\mathrm{n}}(mx)]'} \tag{2.38}$$

$$b_{\mathrm{n}} = \frac{j_{\mathrm{n}}(mx)\,[xj_{\mathrm{n}}(x)]' - j_{\mathrm{n}}(x)\,[mxj_{\mathrm{n}}(mx)]'}{j_{\mathrm{n}}(mx)\left[xh^{(1)}_{\mathrm{n}}(x)\right]' - h^{(1)}_{\mathrm{n}}(x)\,[mxj_{\mathrm{n}}(mx)]'} \tag{2.39}$$

The index n should not be confused with the refractive index $\tilde{n}$. The permeability of the sphere and the surrounding medium was set to unity, resembling in the experimental setups of this work. For the fields inside the sphere the expansion coefficients take up the form:

$$c_{\mathrm{n}} = \frac{j_{\mathrm{n}}(x)\left[xh^{(1)}_{\mathrm{n}}(x)\right]' - h^{(1)}_{\mathrm{n}}(x)\,[xj_{\mathrm{n}}(x)]'}{j_{\mathrm{n}}(mx)\left[xh^{(1)}_{\mathrm{n}}(x)\right]' - h^{(1)}_{\mathrm{n}}(x)\,[mxj_{\mathrm{n}}(mx)]'} \tag{2.40}$$

$$d_{\mathrm{n}} = \frac{mj_{\mathrm{n}}(x)\left[xh^{(1)}_{\mathrm{n}}(x)\right]' - mh^{(1)}_{\mathrm{n}}(x)\,[xj_{\mathrm{n}}(x)]'}{m^2 j_{\mathrm{n}}(mx)\left[xh^{(1)}_{\mathrm{n}}(x)\right]' - h^{(1)}_{\mathrm{n}}(x)\,[mxj_{\mathrm{n}}(mx)]'} \tag{2.41}$$

The macroscopic quantity of the scattering cross section C_{scat} can now be derived by integrating the Pointing vector of the scattered fields $\vec{S}_{\mathrm{scat}} = \frac{1}{2}\mathrm{Re}\{\vec{E}_{\mathrm{scat}} \times \vec{H}^*_{\mathrm{scat}}\}$ over the area A of a sphere with arbitrary radius larger than the radius of the scattering sphere:

$$W_{\mathrm{scat}} = \int_A \vec{S}_{\mathrm{scat}} \cdot \vec{e}_r \mathrm{d}A \tag{2.42}$$

$$C_{\mathrm{scat}} = \frac{W_{\mathrm{scat}}}{I_{\mathrm{i}}} = \frac{2\pi}{k^2} \sum_{n=0}^{\infty} (2\mathrm{n}+1) \left(|a_{\mathrm{n}}|^2 + a_{\mathrm{n}}|^2\right) \tag{2.43}$$

$$\sigma_{\mathrm{scat}} = \frac{C_{\mathrm{scat}}}{A_{\mathrm{cs}}} \tag{2.44}$$

with W_{scat} being the net rate of scattered energy through A and I_{i} the incident irradiance. The ratio between C_{scat} and the geometrical cross section of the scattering sphere $A_{\mathrm{cs}} = r_{\mathrm{sp}}^2 \pi$ is the dimensionless scattering efficiency σ_{scat}.

For the visualization of the derivation of Mie-scattering, the previously published code from C. Bohren and D. R. Huffman [72] was used in a Python environment (Herbert Kaiser, University of Konstanz, Germany) using the recurrence series for the Bessel functions proposed by W. J. Wiscombe [73].

Figure 2.5 a) shows the first order Mie coefficients $|a_1|$, $|d_1|$ of the scattered and internal fields, respectively, as a function of sphere radius, which enters through the size parameter x, at a wavelength of $\lambda = 550\,\mathrm{nm}$. To compare the results with reference [65], the refractive index of the sphere is $\tilde{n}_{\mathrm{sphere}} = 4$ without losses ($k = 0$). It is remarkable that there is a size parameter condition for which the scattering from the lowest order electric dipolar mode vanishes ($r_{\mathrm{sp}} = 102\,\mathrm{nm}$). This minimum is accompanied by a maximum of the internal electric dipolar fields represented by $|d_1|$. Figure 2.5 b) displays the scattering efficiency σ_{scat} in the spectral domain for a sphere with radius $r = 102\,\mathrm{nm}$. σ_{scat} is calculated for the first order electric dipolar fields ($b_1 = 0$) as well as to second order for electric and magnetic multipoles. As expected, a scattering minimum at λ =550 nm arises for $\sigma_{\mathrm{scat}}(a_1)$, which is superimposed by scattering maxima from the higher order Mie modes. In addition, Figure 2.5 b) shows the electric energy W_{el} inside the sphere from the lowest order internal electric fields normalized to W_{el} of a sphere with the same refractive index as the surrounding medium ($n = 1$): [65]

$$E_{\mathrm{int}} \propto d_1 \cdot N^{(1)}_{\mathrm{e11}} \tag{2.45}$$

$$W_{\mathrm{el}}^{\mathrm{norm.}} = \frac{\frac{\tilde{n}_{\mathrm{sp}}^2}{2} \int |d_1 N^{(1)}_{\mathrm{e11}}|^2 \mathrm{d}V_{\mathrm{sphere}}}{\frac{\tilde{n}^2}{2} \int |\underbrace{d_1(\tilde{n}=1)}_{=1} N^{(1)}_{\mathrm{e11}}|^2 \mathrm{d}V_{\mathrm{sphere}}} \tag{2.46}$$

$$\rightarrow W_{\mathrm{el}}^{\mathrm{norm.}} = \tilde{n}_{\mathrm{sp}}^2 |d_1|^2 \tag{2.47}$$

Figure 2.5 b) clearly reveals the condition of the anapole, which is a minimum in far-field scattering together with a spectrally close maximum of electric energy inside the scattering

particle. Furthermore, by reinvoking equation 1.3, it becomes clear that the anapole state is ideally suited to increase the absorption in a particle because it leads to a strong enhancement of $|E_{\mathrm{int}}|^2$. At this point, a clear assignment of the maxmimum of $W_{\mathrm{el}}(\lambda = 570\,\mathrm{nm})$ to the anapole state is hindered by the presence of a multitude of higher order modes that arise due to the spherical geometry of the particle.

The anapole state can also be identified through a different approach using the spatially discretized electric field $\vec{E}(\lambda, \vec{r})$ calculated with a FDTD simulation. From $\vec{E}(\lambda, \vec{r})$ the currents are obtained by

$$\vec{J}(\lambda, \vec{r}) = -\frac{2i\pi c\epsilon_0}{\lambda}(\tilde{n}^2 - 1)\vec{E}(\lambda, \vec{r}) \tag{2.48}$$

The far-field scattering contributions of the electric, magnetic and toroidal dipolar moments (ED, MD, TD respectively) follow directly, taking the underlying equations for the multipolar decomposition from table 2.1. [74, 75, 76] In practice, the integrals for the calculation for the dipolar moments turn into sums over the discretized volume elements of the particle.

Dipole Type	Dipolar Moment	Far-field scattering power
Electric	$P(\lambda) = \frac{\lambda}{2i\pi c}\int J(\lambda, \vec{r})dV$	$I_{\mathrm{P}}(\lambda) = \frac{32c}{3}\left(\frac{\pi}{\lambda}\right)^4 \lvert P(\lambda)\rvert^2$
Magnetic	$M(\lambda) = \frac{1}{ic}\int \vec{r} \times \vec{J}(\lambda, \vec{r})dV$	$I_{\mathrm{M}}(\lambda) = \frac{32c}{3}\left(\frac{\pi}{\lambda}\right)^4 \lvert M(\lambda)\rvert^2$
Toroidal	$T(\lambda) = \frac{1}{10c}\int\{[\vec{r}\cdot\vec{J}(\lambda, \vec{r})]\vec{r} - 2r^2\vec{J}(\lambda, \vec{r})\}dV$	$I_{\mathrm{T}}(\lambda) = \frac{128c}{3}\left(\frac{\pi}{\lambda}\right)^6 \lvert T(\lambda)\rvert^2$

Table 2.1: Mathematical expressions of fundamental dipolar moments and corresponding far-field scattering power

The far-field scattering contributions from the ED, MD and TD in a dielectric sphere with refractive index of $\tilde{n} = 4$ are shown in Figure 2.5 c). Analogously to $\sigma_{\mathrm{scat}}(a_{\mathrm{n}})$, the ED exhibts a minimum at $\lambda \approx 550\,\mathrm{nm}$. The simultaneous presence of the TD indicates the condition of the anapole state because this leads to the destructive interference of far-field scattering. This can be deduced from electric field plot in the equatorial cross section of the disk in the x-y-plane (Fig. 2.5 c, inset). The phase of the fields at the edges are π-shifted with respect to the center. The non-zero constribution of the MD at the anapole state impedes a vanishing scattering at the anapole condition in a spherical particle geometry. The FDTD simulated σ_{scat} replicate the scattering minimum at 550 nm (Fig. 2.5 d). But also higher order modes dictate the scattering behavior of the sphere, as also present in the Mie calculations. Again, σ_{scat} is correlated with the electric energy inside the sphere, which is normalized by W_{el} of a sphere of the same radius and $n = 1$. The situation becomes easier by changing the particle geometry to a flat disk. On the one hand, this would impose further mathematical workout to derive the internal and scattered fields by Mie theory.

On the other hand, the FDTD based multipolar decomposition in a flat disk demonstrates suppression of the MD and higher order modes while replicating the anapole condition at $\lambda = 550\,\mathrm{nm}$ by the minimum of the ED and the onset of the TD (Fig. 2.5 e). This allows for a clear discrimination of the contributions of the fundamental dipolar moments to the total scattering efficiency and electric energy. In analogy to the FDTD sphere, σ_{scat} and W_{el} of the disk are correlated in Figure 2.5 f). The anapole condition from the lowest order Mie modes is reproduced and the total scattering minimum can be clearly assigned to the maximum of electric energy inside the disk.

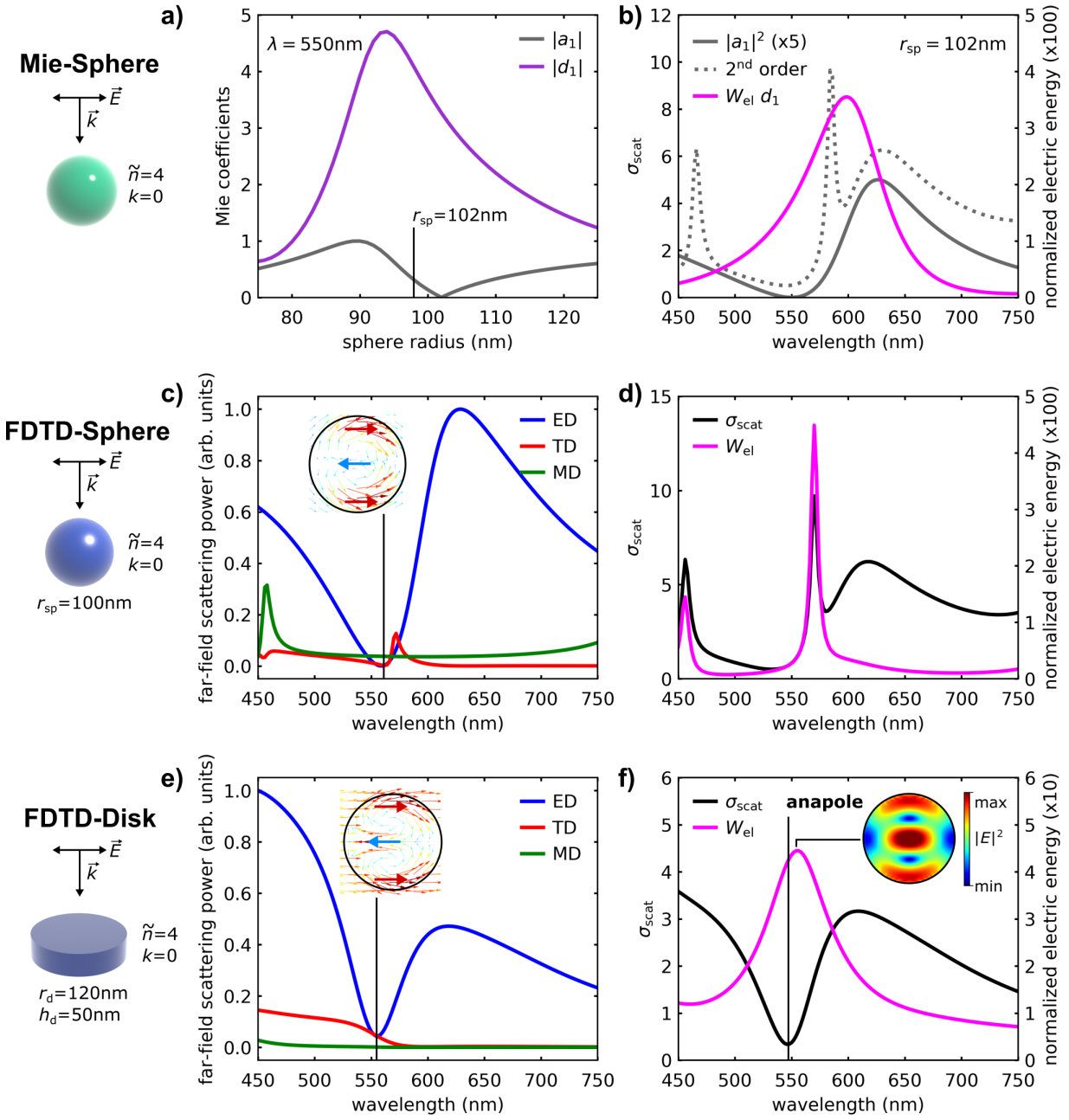

Figure 2.5: a) Lowest order Mie coefficients for the scattered ($|a_1|$) and internal ($|d_1|$) electric dipolar fields as a function of the dielectric sphere radius r. b) Scattering efficiency spectra from the first order electric dipole ($|a_1|^2$) and full Mie expansion to second order together with normalized electric energy from the internal electric dipolar field. c) Multipolar decomposition spectra of FDTD simulated electric fields in a dielectric sphere into electric (ED), toroidal (TD) and magnetic (MD) dipolar moments. Inset: Electric vector field in the equatorial plane perpendicular to the wavevector $\vec{k}$. d) FDTD simulated scattering efficiency and normalized electric energy spectra. e) and f) show the results of a dielectric disk analogously to c) and d). Inset: Electric field strength at the maximum of W_{el} at $h_d/2$.

Chapter 3

Experimental Methods

After setting out the theoretical basis for understanding Chapters 4-7, the following sections explain the specific experimental methods used therein. Experimental details, additional information on other more common methods, and descriptions of the simulation setups are given at the end of each chapter.

3.1 Photothermal Deflection Spectroscopy

A highly sensitive method to spectrally resolve weak absorption in thin films is provided by photothermal deflection spectroscopy (PDS). A description of transverse PDS is given here, a profound treatment of this technique can be found in reference [77]. The PDS measurements were carried out by Felix Eckmann from Walter-Schottky-Institute of the Technical University Munich during the collaboration for the project "Anapole Excitations in Oxygen-Vacancy-Rich TiO_{2-x} Nanoresonators: Tuning the Absorption for Photocatalysis in the Visible Spectrum". [47]

The technique is based on the effect that upon absorption of electromagnetic radiation by a given medium a fraction or all the excitation energy will be converted to thermal energy. The change in temperature in the probed medium causes a spatial gradient of the refractive index in its surrounding medium. A light beam traversing the volume directly adjacent to the probed medium is therefore deflected from its original path. The magnitude of deflection can be correlated with the change of temperature and ultimately the absorbance of the probed medium.

This is experimentally realized by transverse PDS, whose setup is depicted in Figure 3.1. A thin film on a non-absorbing substrate is placed in a glass cuvette filled with a liquid. As a requirement, the refractive index of the liquid should highly depend on temperature and it should be fully transparent over the spectral range of measurement. The sample is excited by a wavelength selective, monochromatic pump beam which causes a temperature change induces refractive index gradient in the liquid. This gradient is detected by the deflection

d of a probe laser that traverses the cuvette parallel along the surface of the sample and perpendicular to the pump laser. The deflection detected by the photodetector is directly proportional to the absorbed power of the pump laser by the sample. With calibration of the setup and known thickness of the thin film its absorption coefficient can be determined. The measurement is repeated for different wavelenghts of the pump laser resulting in an absorption spectrum of the thin film.

In the used setup, the liquid is Perfluorhexane (C_6F_{14}). The pump beam is spectrally selected from a 150 W Xe lamp, chopped with a repetition rate of 10 Hz and focused to a beam diameter of 4 mm on the film surface. The probe laser has a wavelength of 635 nm.

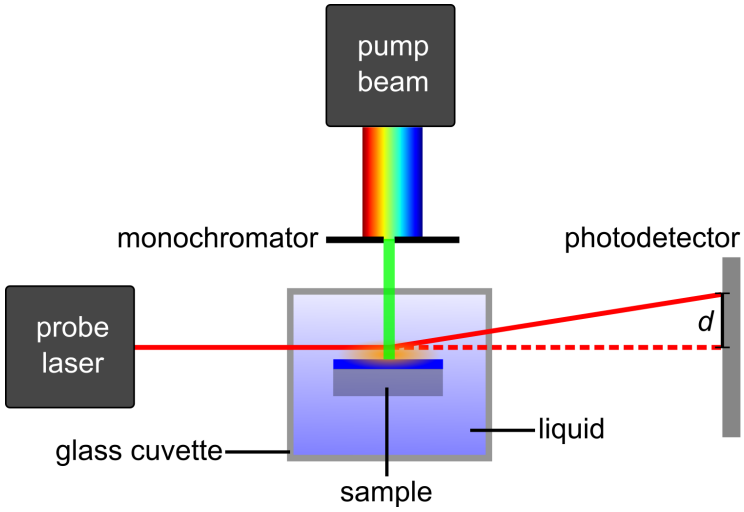

Figure 3.1: Experimental setup for transverse PDS: The sample is placed into a glass cuvette filled with a liquid exhibiting a high thermo-optic coefficient. The sample undergoes absorptive heating by the illumination of a wavelength selective pump laser. The resulting gradient of the refractive index in the liquid causes the deflection *d* of the probe beam which is measured by a photodetector.

3.2 Dark-Field Spectroscopy

As demonstrated in section 2.2, the presence of photonic modes in nanoparticles can be determined by the macroscopic physical quantity of cross section C_{scat}. Dark-field spectroscopy is the experimental method to measure C_{scat} because – in contrast to bright-field spectroscopy – it enables the separation of the illumination signal from the far-field scattering of the particle under concern. This is accomplished by illuminating the particle with a hollow cone of light provided by a condenser with two numerical apertures $\mathrm{NA}_{\mathrm{con}}^{\mathrm{outer}}$ and $\mathrm{NA}_{\mathrm{con}}^{\mathrm{inner}} \approx \mathrm{NA}_{\mathrm{con}}$, as depicted in Figure 3.2 a). The scattering signal from the particle is collected by an objective with $\mathrm{NA}_{\mathrm{obj}} < \mathrm{NA}_{\mathrm{con}}$, such the illumination signal is not detected. The collected light is collimated at the back focal plane of the objective. In a confocal setup, a lens focuses the light to a pinhole which represents the conjugated focal point of the objective. Light that passes through the pinhole is coupled to a spectrometer.

A dark-field setup can be realized in two ways: In reflection, if the condenser is integrated into the collection objective (Fig. 3.2 a). In transmission, if the condenser is located below the sample (Fig. 3.2 b). In that case a transparent substrate (*e.g.* SiO_2) is required and its thickness must not exceed the working distance of the condenser. In addition, an immersion oil with an approximate refractive index of the substrate needs to be filled between the condenser and the substrate back side to avoid undesired reflections from the refractive index contrast between air and substrate.

The experimental procedure to determine C_{scat} is reflected in equations 3.1 and 3.2 and illustrated in Figure 3.2 c) and d) with the example of TiO_2 nanodisks. In total, four spectra $I(\lambda)$ need to taken: The spectrum I_{p} from the nanodisk (particle) is corrected by the background I_{bg}. This difference is normalized by the illumination lamp spectrum I_{lamp}, which is taken on an ideal scatterer object, from which the spectrometer dark counts I_{dark} are subtracted. This fraction represents the scattering efficiency $\sigma_{\mathrm{scat}}(\lambda)$ of the nanodisk. For the calculation of the scattering cross section $C_{\mathrm{scat}}(\lambda)$, the geometrical cross section A_{p} can be determined from an SEM image.

$$\sigma_{\mathrm{scat}}(\lambda) = \frac{I_{\mathrm{p}}(\lambda) - I_{\mathrm{bg}}(\lambda)}{I_{\mathrm{lamp}}(\lambda) - I_{\mathrm{dark}}(\lambda)} \tag{3.1}$$

$$C_{\mathrm{scat}}(\lambda) = \sigma_{\mathrm{scat}}(\lambda) \cdot A_{\mathrm{p}} \tag{3.2}$$

In practice, the measurement of σ_{scat} is often sufficient, because the scattering contribution from photonic modes in the particle are interpreted from the extrema of σ_{scat}, rather than from its absolute magnitude. It should be also pointed out, that in this work experimental results of σ_{scat} are numerically resembled by *plane wave* illumination simulations. However, the sound agreement between measurements and simulations justifies that potential longitudinal modes in the particle excited by the high angle illumination do not dominate the optical response of the nanoparticles investigated here and the connection between macroscopic and microscopic quantities can be established via σ_{scat}.

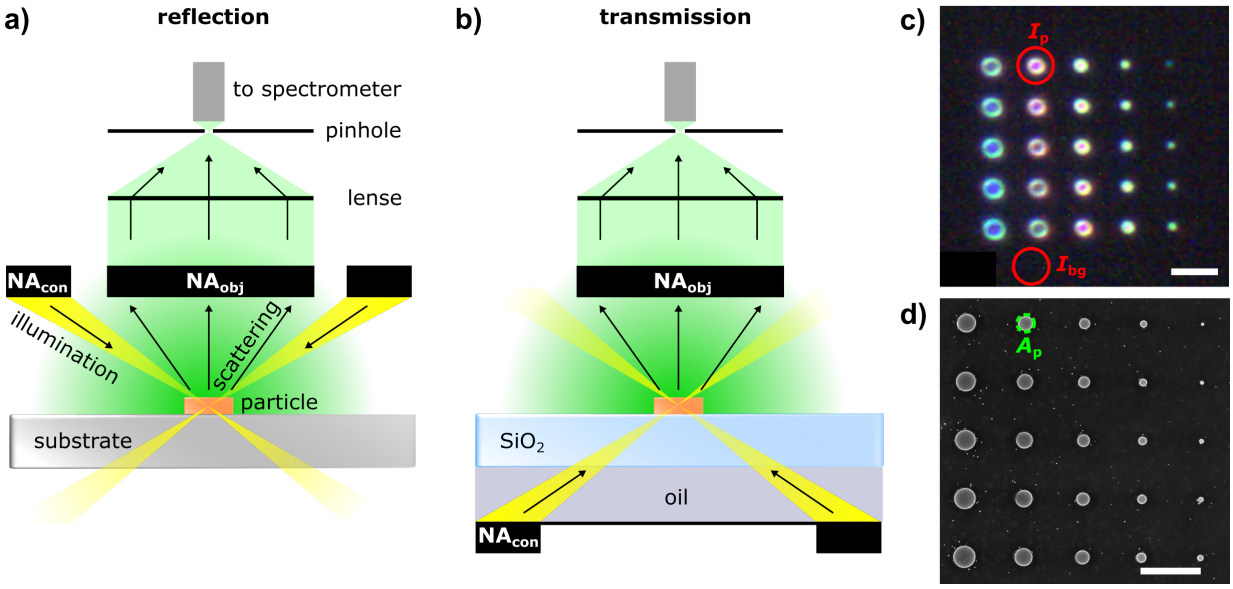

Figure 3.2: Dark-field spectroscopy setups: a) Reflection and b) transmission. c) Dark-field microscopy image of an array of TiO_2 nanodisks. The red circles indicate the spots of measurements for the determination of σ_{scat}, *i.e.* on the particle (I_{p}) and on the background (I_{bg}). d) Corresponding SEM image with A_{p} indicating the cross section of the measured nanodisk. The scale bars correspond to 3 µm.

3.3 Ag^+ Photoreduction

The photocatalytic activity of single, submicrometer particles cannot be proved by photocurrent or gaschromatographic measurements because their active surface is too small to produce detectable product yields. Therefore, a different method is required to demonstrate anopole assisted catalytic enhancement in single nanodisks: The presence of transition metal ions in the electrolyte has been shown to affect the rate of the heterogeneous photocatalytic oxidation of water. [78] As an example, Ag ions in $AgNO_3$ solution increase the OER rates of TiO_2 according to the reaction equation: 3.3 [79]

$$4Ag^+ + 2H_2O \xrightarrow[TiO_2]{h\nu > E_g} 4Ag + O_2 + 4H^+ \tag{3.3}$$

As a by-product, Ag ions are reduced and form clusters on the illuminated SCPC surface, providing evidence for photocatalytic charge transfer. [79, 80, 81, 82, 59] Due to their metallic nature, these clusters strongly scatter light and are therefore visible in dark-field microscopy. This method provides a useful indication for photocatalytic activity without requiring large active surfaces. Figure 3.3 a) shows a dark-field microscopy image of a TiO_2 film surface immersed in a 1mM $AgNO_3$ solution and illuminated point-wise with a 405 nm laser. The scattering of the Ag clusters indicates the locations where the OER has occurred.

The Ag^+ reduction reaction is highly sensitive to light with wavelengths $\lambda < hc/E_{\mathrm{t}}$, with E_{t} being the required energy of electron transitions from the valence to either the conduction

band (= E_g) or – in the case of substoichiometric TiO_2 – to defect related sub-bandgap states. This leads to uncontrolled Ag growth during dark-field illumination by a broad-band light source. This problem is solved by the insertion of a long pass filter before the dark-field condenser, which provides a spectral separation of illumination and excitation light. Figure 3.3 b) shows arrays of TiO_{2-x} nanodisks under "red dark-field" illumination. The nanodisks can be localized on the sample without initialization of Ag deposition.

To find the appropriate conditions of excitation power and time to prove preferred Ag growth on a nanodisk supporting the AE, it is convenient to monitor the reaction *in situ*. For this, a notch filter is inserted after the beam splitter and before the camera, which blocks the reflected laser light. The full setup is depicted in Figure 3.3 c). With this configuration, the nanodisks can be excited individually while controlling the Ag deposition state.

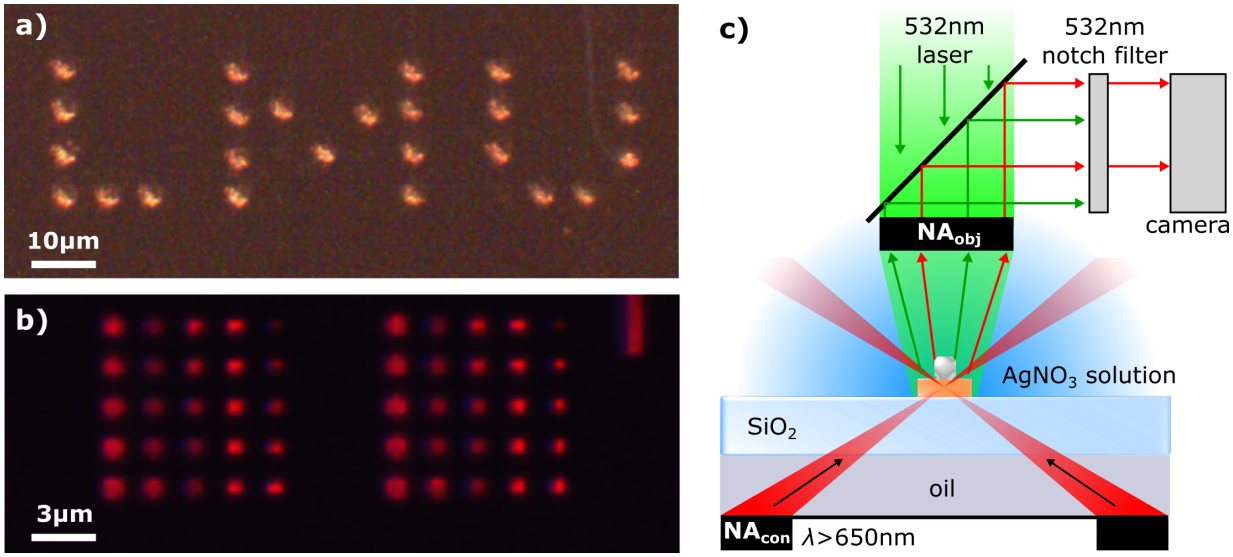

Figure 3.3: a) Photoreduced Ag clusters deposited on a TiO_2 film by a focused 405 nm laser. b) Dark-field image of TiO_2 nanodisk arrays with illumination wavelengths > 650 nm. c) Scheme of experimental setup for photoreduction of Ag^+ from a $AgNO_3$ solution with 532 nm excitation laser onto single nanodisks with *in situ* monitoring of Ag particle growth.

3.4 Photoelectrochemical Cell

The previously described method of Ag^+-photoreduction enables the proof of photocatalytic activity, but it lacks of its precise quantification. The influence of light and applied voltage on catalytic yields of large surface photoelectrodes can be determined more precisely in a photoelectrochemical (PEC) cell. The most simple form of a PEC is depicted in Figure 3.4. It consists of two electrodes, which are immersed in a electrolyte and connected through a voltage source with an amperemeter. Once voltage is applied, the negative electrode (cathode) drives the reduction and the positive electrode (anode) the oxidation of a redox reaction. The reaction yields can be either determined directly by separating the cell into a reduction and an oxidation compartment by a diaphragm and measuring the amounts of reaction products. This involves further analysis methods like gas chromatography in the case of gaseous reaction products. The indirect way is to measure the current and draw conclusions about the product yields from the required charge transfer into the electrolyte for the specific reaction. Special care needs to be taken if multiple reactions can occur under the same PEC conditions because the current cannot be assigned to a specific reaction, unless the generation ratio between multiple products is experimentally determined.

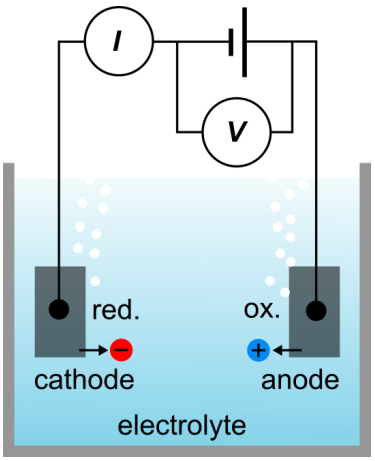

Figure 3.4: Two-electrode electrochemical cell

In a two electrode setup the potential of each electrode can only be determined relatively to each other. The catalytic yields not only depend on the potential difference between the electrodes, but also on their absolute potentials. Therefore, a reference electrode (RE) with a known potential in the used electrolyte is added to the PEC cell. By connecting the three electrodes to a potentiostat, the potentials of the cathode and anode can be controlled with respect to the RE potential. To probe the performance of a single electrode its potential is varied while that of the other is kept constant. The first is called working electrode (WE) and the latter counter electrode (CE). In the setup used in this work, the semiconductor metasurface photoelectrodes act as working electrodes (WE) and are investigated regarding their water reduction capability. A platinum mesh is used as CE together with a Ag/AgCl RE stored in 3 M KCl. The used electrolyte was 1 M $HClO_4$ with a pH = 0. The conversion from the potential against Ag/AgCl to the more comparable potential against reversible hydrogen electrode (RHE) is done according to the equation 3.4: [83]

$$E_{\mathrm{RHE}} = 0.210 + (0.0591 \times \mathrm{pH}) + E_{\mathrm{Ag/AgCl}} \tag{3.4}$$

The WEs are investigated with regard to applied voltage and illumination. Thus, there are four conditions, whose thermodynamics are presented in Figure 3.5 a) for the case of reduction with the example of a n-doped semiconductor (n-SC) WE. The n-SC has a

bandgap E_g and chemical potential μ and is immersed in a electrolyte together with a platinum CE. In dark and without bias, the equilibration of μ with the reduction potential $E_{red.}$ leads to upward band bending of the conduction (E_c) and valence (E_v) band at the solid-liquid interface. To generate current, the cathodic onset potential $V = \Delta_{red.}$ needs to be applied, such μ exceeds E_c and the conduction band is populated with electrons.

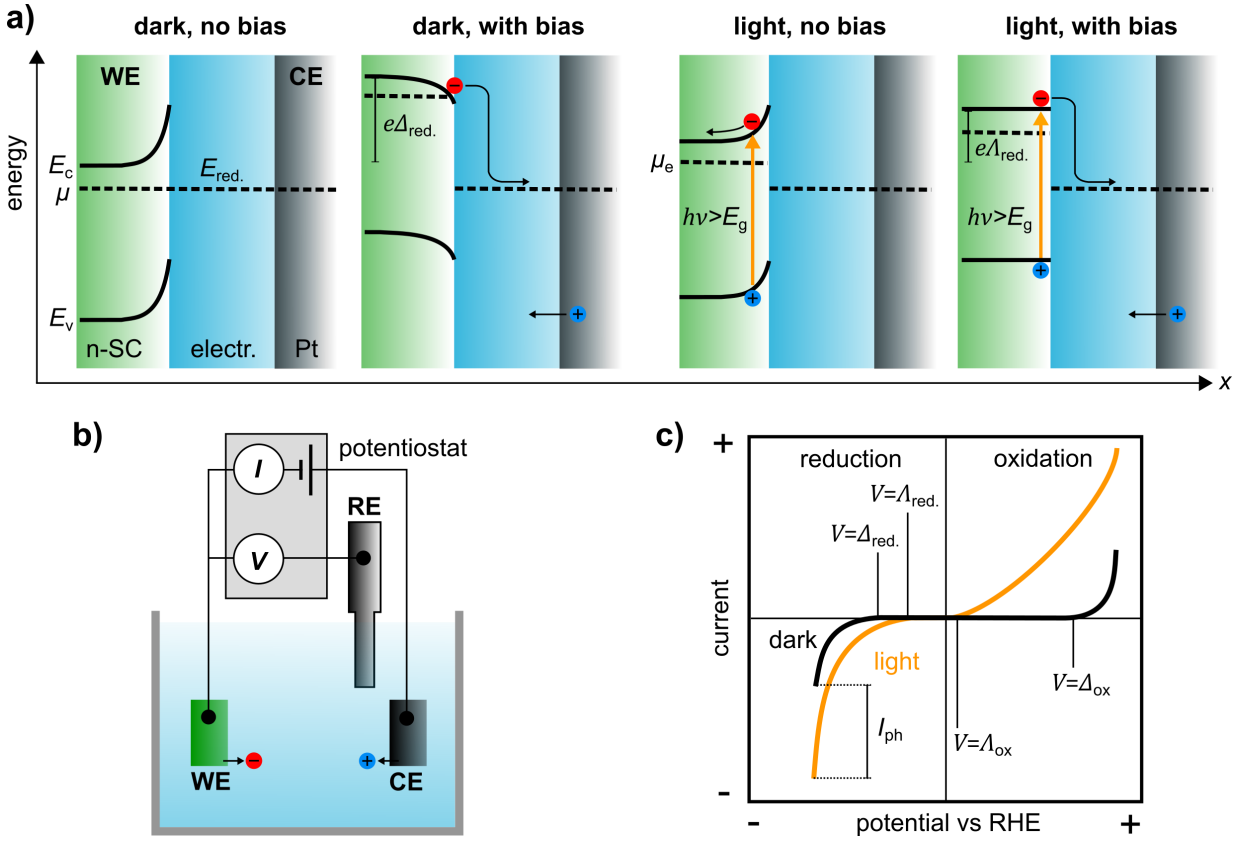

Figure 3.5: a) Thermodynamics of a PEC cell comprising a n-doped semiconductor working electrode (WE) and a platinum reference electrode (CE) immersed in an electrolyte under four conditions of on-off bias and light irradiation. b) Scheme of a three electrode PEC cell connected to a potentiostat. c) Typical *I-V* characteristics of an n-doped SC in the role of the WE in dark and under illumination. Δ and Λ denote the onset potentials for dark and light, respectively, on the reduction or oxidation side. The photocurrent is the difference between dark and light current.

Under irradiation of photons of energy $h\nu > E_g$ the excitation of electrons to the conduction band causes a charge carrier population change and thus, a splitting of the chemical potentials for holes and electrons ($\mu_e > \mu$). [13] These also called quasi-Fermi levels play an important role in processes at the SC-liquid interface, because the relative position of the quasi-Fermi level (chemical potential) with respect to that in solution yields the thermodynamic force which drives an electrochemical reaction. [84] This effect decreases the potential barrier, but photoexcited electrons still drift away from the solid-liquid interface without bias. At this point it becomes obvious, that p-type SCs, are more favourable for the photocatalytic reduction, because the bands bend downwards towards the solid-liquid interface,

which strongly reduces the onset potential, even enabling "unassisted" photocatalysis without external bias. On the other hand, n-type SCs are better suited for the photocatalytic oxidation reaction. In the presence of light, an onset potential $V = \Lambda_{\text{red.}} < \Delta_{\text{red.}}$ is necessary to achieve a flat band condition and to generate a photocurrent. The magnitude of the photocurrent in turn increases with the number of photoexcited electrons, *i.e.* with the absorbance of the material.

A scheme of the measurement setup is shown in Figure 3.5 b). The three electrodes are immersed in the electrolyte and contacted to the potentiostat. Figure 3.5 c) illustrates schematically the typical *I*-*V* characteristics of an n-doped SC in the role of the WE in dark and under illumination. The specific values of the onset potentials highly depend on the material system and the electrolyte. The difference between current with light and in dark is the photocurrent I_{ph}.

A picture and a description of the experimental PEC setup are presented in Figure 3.6. The 400 nm long pass filter prevents absorption heating of the reactor glass. The cooled water filter blocks IR irradiation such the aqueous electrolyte is not heated by the lamp.

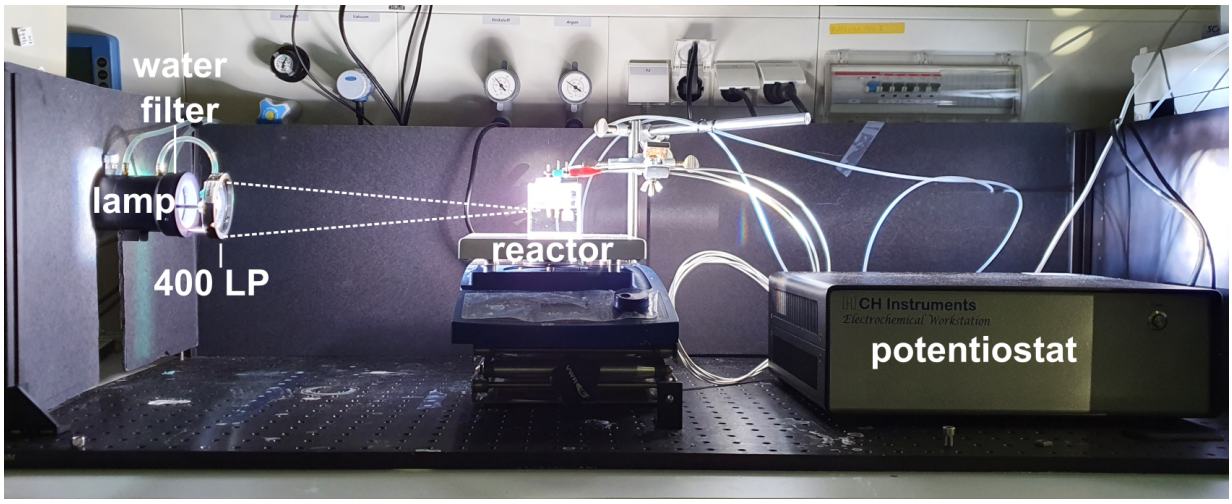

Figure 3.6: a) Photograph of photoelectrochemical setup comprising a 1000 W Hg/Xe lamp with a IR water filter and a 400 nm long pass filter. The radiant power at the reactor can be varied by changing the lamp focus. The electrodes are connected to the potentiostat.

Chapter 4

Anapole-Assisted Photoconversion on a Single TiO_{2-x} Nanoresonator

Published in:
L. Hüttenhofer, F. Eckmann, A. Lauri, J. Cambiasso, E. Pensa, Y. Li, E. Cortés, I. D. Sharp, and S. A. Maier
"Anapole Excitations in Oxygen-Vacancy-Rich TiO_{2-x} Nanoresonators: Tuning the Absorption for Photocatalyis in the Visible Spectrum"
ACS Nano 2020, 14, 2456-2464, reference [47], publisher permission see appendix B

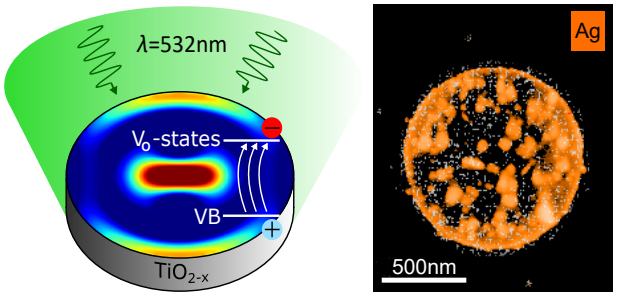

For the support of anapole excitations (AEs), TiO_2 is an applicable dielectric material also known for photocatalytic activity. Because of its wide bandgap ($>3\,$eV), optical absorption is restricted to the UV, which severely limits its efficiency for solar light harvesting. Several routes to increase the material absorption edge over the visible spectrum are discussed in section 1.2. One approach is to reduce TiO_2 to oxygen-vacancy-rich TiO_{2-x} [85, 41, 18, 86, 87, 29], which is a prominent photocatalytic material for water splitting and serves as a robust model system. At sufficiently high concentrations, the oxygen vacancies (V_O's) form a shallow defect band below the conduction band, thereby extending the absorption from the UV to the visible. [88] A facile approach for creating V_O's is annealing during synthesis or through post-treatment. [89, 90] The modification of optical properties arises from the diffusion and surface desorption of oxygen atoms, which in turn leaves oxygen vacancies in the bulk. The visible absorption of V_O's can be tuned by varying the annealing temperature, making this an instructive material to study the potential of the AE for absorption and photocatalytic enhancement.

In previous studies of anapole-assisted field confinement, low cavity losses were achieved

by employing materials with as low as possible extinction coefficient (imaginary part of the complex refractive index) k and large real part of the complex refractive index $n > 3$, such as Si or Ge in their respective transparent spectral regions. [65, 63, 91] Materials with moderate refractive index ($n < 3$) have not been fully investigated, in particular for their photocatalytic properties in absorptive regimes. This study demonstrates that the electric field confinement in dielectric nanodisks at AEs can also be used to enhance the absorption throughout the visible spectrum for the improvement of their photocatalytic activity.

4.1 The Role of the Complex Refractive Index

Figure 4.1 a) describes how the AE and damping (extinction coefficient, k) affects the absorption of the resonator. It displays the scattering and absorption efficiencies of nanodisks, $\sigma_{\mathrm{scat/abs}}$ as a function of disk radius, r_{d}, and k at the probe wavelength of $\lambda_{\mathrm{p}} = 532\,\mathrm{nm}$. λ_{p} was chosen as a representative wavelength of the spectral maximum of solar irradiation. Further settings are a constant real part of the refractive index $n = 2.4$, disk height $h_{\mathrm{d}} = 100\,\mathrm{nm}$ and aqueous environment of $n_{\mathrm{water}} = 1.33$. For constant values of k, indicated by the dashed lines in Figure 4.1 a), minima of scattering that correspond to maxima of absorption are observable, arising from the AE and its higher orders [63] (HOAE) at distinct disk radii (Fig. 4.1 b and 4.1 c). The dotted lines in Figure 4.1 b) indicate the absorption efficiencies of continuous films with the same thickness, h_{d}, exhibiting no resonant electric field confinement effect. On top of increasing film absorption with rising $k(\lambda_{\mathrm{p}})$ the (HO)AEs allow for further absorption enhancement. However, if $k(\lambda_{\mathrm{p}}) = 0$, there is no damping and the presence of the (HO)AEs does not lead to absorption enhancement. A comparison between the absorption of a disk at AE relative to a continuous film and to a disk off AE is shown in Figure 4.1 d) and σ_{abs} of the *film* and *off AE* is indicated in 4.1 b, respectively. The absorption enhancement reaches the respective maximum of 60 % and 30 % for k being close to zero.

For experimental reasons this low-k regime in TiO_{2-x} is preferable, because the contrast between (HO)AE and bare material absorption is most pronounced. It is important to notice that higher over-all absorption of the disks could be achieved with high k values. However, the goal of the research at this stage is to elaborate on the capability of anapole assisted absorption which for high k would be compromised by material dominated absorption in the resonator.

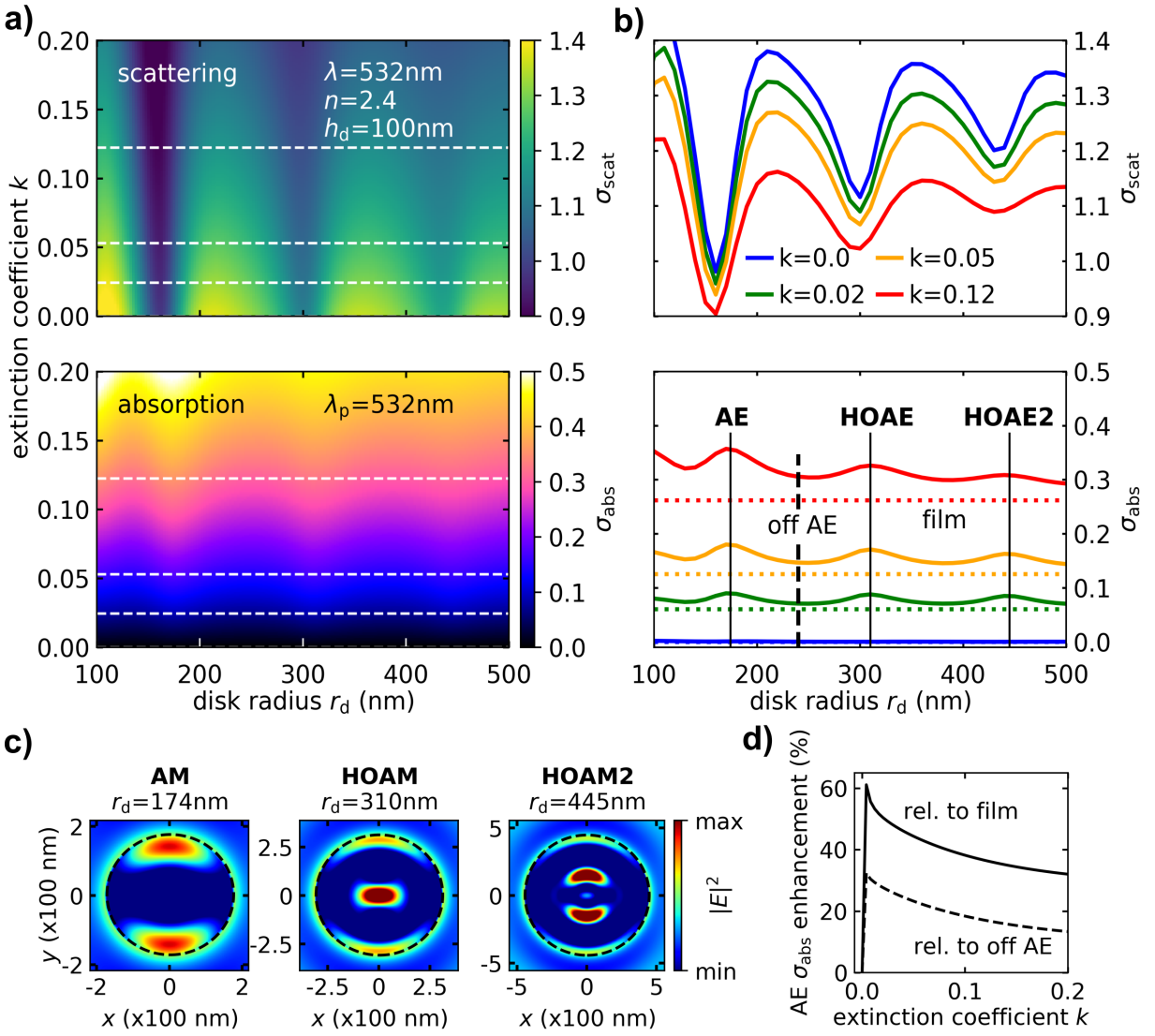

Figure 4.1: a) Simulation of scattering (top) and absorption (bottom) efficiencies of TiO_{2-x} nanodisks as a function of extinction coefficient k and disk radius r_d at the probe wavelength λ_p = 532 nm. The disks of height h_d = 100 nm have a refractive index n = 2.4 and are placed on glass in water environment. b) Cross sections through the maps on the left for different k indicated by the white dashed lines on a). The dotted lines in the lower panel represent the absorption of corresponding continuous films with the same height. The coincidence of scattering minima and absorption maxima indicates the presence of the fundamental anapole excitation (r_d =174 nm, AE) and its higher orders (r_d = 310 nm and 445 nm, HOAEs). c) shows the respective electric near-field distributions at z = 50 nm. d) AE absorption efficiency enhancement relative to a film of the same height and a disk off AE (r_d = 240 nm, see panel b) as a function of extinction coefficient k.

4.2 Optical Characterization of TiO_{2-x}-Films

Vacancy creation in TiO_2 enables the control of the extinction coefficient in the bulk. For the creation of V_O-states, TiO_2 films with thickness of 200 nm were annealed in a high vac-

uum furnace at various temperatures. Figure 4.2 a) shows absorption measurements based on photothermal deflection spectroscopy (see methods 3.1) converted into $k = \alpha \cdot \lambda/4 \cdot \pi$, with k, α and λ being the extinction coefficient, the absorption coefficient and the wavelength, respectively. The raw data of $\alpha(\lambda)$ is shown in the Figure A.1. The effect of annealing on the materials absorption is visible by eye as the films turn darker with increasing T_{an} (Fig. 4.2 b). In a detailed presentation of k over the spectral regime of interest (Fig. 4.2 c) the monotonous trend of $k(T_{\mathrm{an}})$ becomes evident. Up to $T_{\mathrm{an}} = 300\,^{\circ}\mathrm{C}$, no sizable change of the absorption in the visible range occurs. From $T_{\mathrm{an}} = 400\,^{\circ}\mathrm{C}$ there is an onset of absorption enhancement with a large jump from 600 °C to 700 °C. In Figure 4.2 c) also the laser wavelengths used for $AgNO_3$ reduction are indicated and $k(T_{\mathrm{an}}, \lambda)$ is plotted in Figure 4.2 d). The spectral characteristics of the optical absorption are consistent with previously reported V_O-related absorption in TiO_{2-x}. [87] In contrast to surface V_O's created by UV-B exposure, which suffer from vacancy healing within hours under ambient conditions due to re-oxidation [92], bulk V_O's from annealing remain stable in the material, confirmed by the detailed changes of the absorption spectra that were always measured various days after the annealing.

Raman measurements on different films, displayed in Figure 4.2 e), reveal that the creation of V_O-states is accompanied by a phase change from amorphous (as-deposited) to anatase [93, 94, 95] for $T_{\mathrm{an}} \geq 400\,^{\circ}\mathrm{C}$. It is well known that different phases of TiO_2 exhibit different refractive indices n. [96] Because the AE wavelength is not only sensitive to geometry but also to the real part of the refractive index n, this index change was measured directly using spectroscopic ellipsometry. Figure 4.2 e) shows the data from the as-deposited amorphous film compared to one annealed at 600 °C, along with the fit. The index difference between amorphous and anatase of $\Delta n \approx 0.2$ was accounted for in the finite difference time domain (FDTD) simulations and enabled to achieve good fitting of simulations to measurements. The discontinuities in the data of the annealed film arise from crack formation upon annealing at $T_{\mathrm{an}} \geq 400\,^{\circ}\mathrm{C}$ (see Fig. A.2), which complicated ellipsometry measurements, but reasonable agreement between the fit and experimental data was obtained over the UV and visible spectral range of interest in this work. In general, the possibility to tune the value of k in TiO_{2-x} offers great opportunity to tailor the absorption of dielectric resonators.

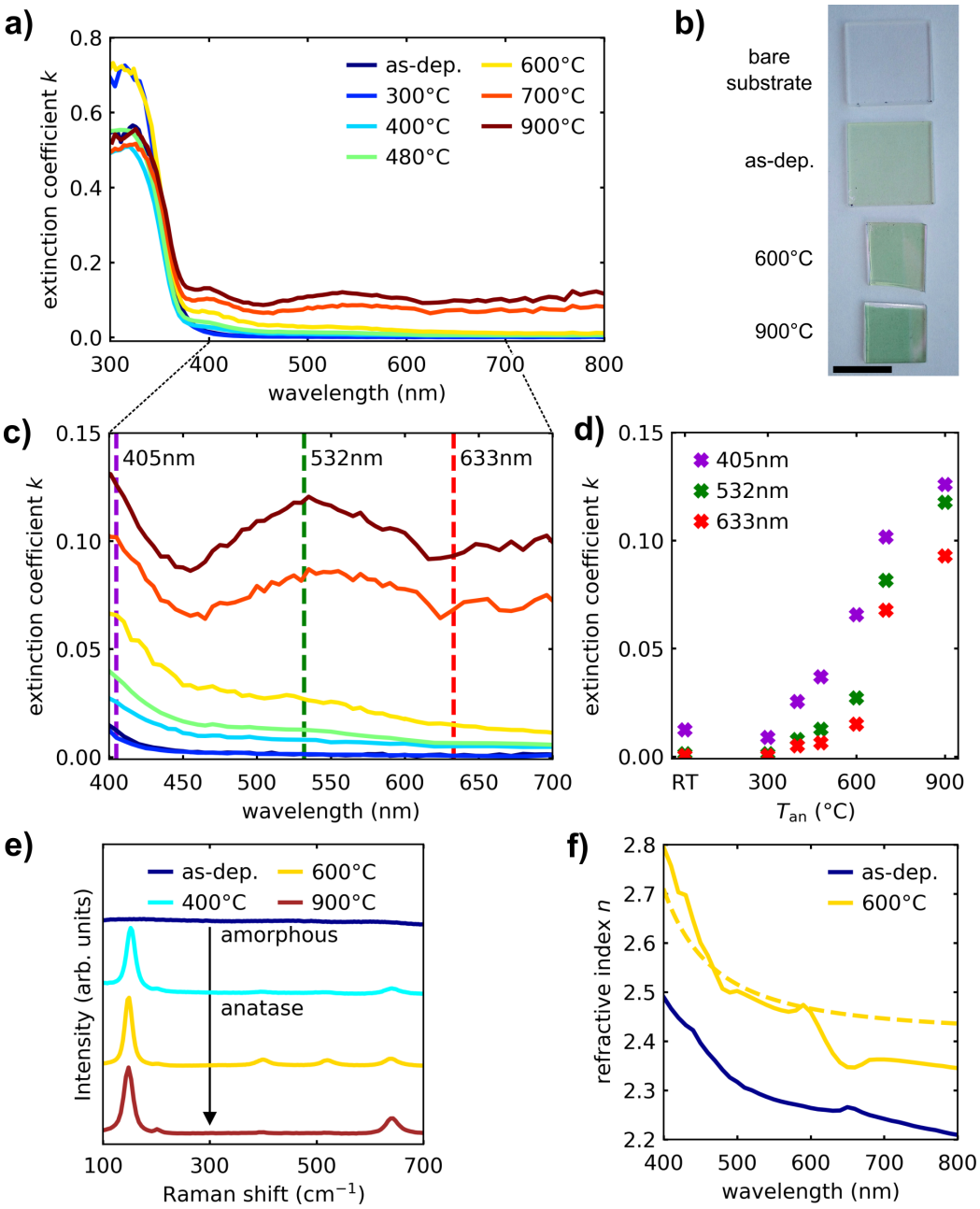

Figure 4.2: a) Extinction coefficient, k, of TiO_2-films as-deposited (as-dep.) and after annealing at various temperatures. b) Fotograph of $TiO_{2(-x)}$ films on SiO_2. Scale bar corresponds ot 5 mm. c) Zoom of a) with indicated laser wavelengths used for $AgNO_3$ reduction. d) shows the k-values at different wavelengths as a function of annealing temperature. e) Raman spectra of corresponding films: the as-deposited film is amorphous, annealing at temperatures higher than 400 °C cause a phase change to anatase. f) Refractive index n of TiO_2 before and after annealing extracted from experimental ellipsometric data with the fit used for FDTD-simulations as dashed line. The phase change leads to an increase of $\Delta n \approx 0.2$ throughout the visible spectrum.

4.3 Correlation of Oxygen-Vacancy Concentration and Photocatalytic Activity

To demonstrate that the modified absorption of the films also affects their photocatalytic activity along the visible spectrum, Ag^+ photoreduction experiments with lasers of different wavelengths but at the same power density $\rho \approx 3.5$ mW/µm^2 and excitation time 10 s were conducted (Fig. 4.3 a). The Ag^+ ions reduce by charge transfer of electrons excited to V_O-states and cluster on the surface of the material. [59] The formed Ag particles scatter red probe light under dark-field illumination, which could be visualized because a 650 nm longpass filter in the light source was inserted to separate broadband probe illumination from laser excitation.

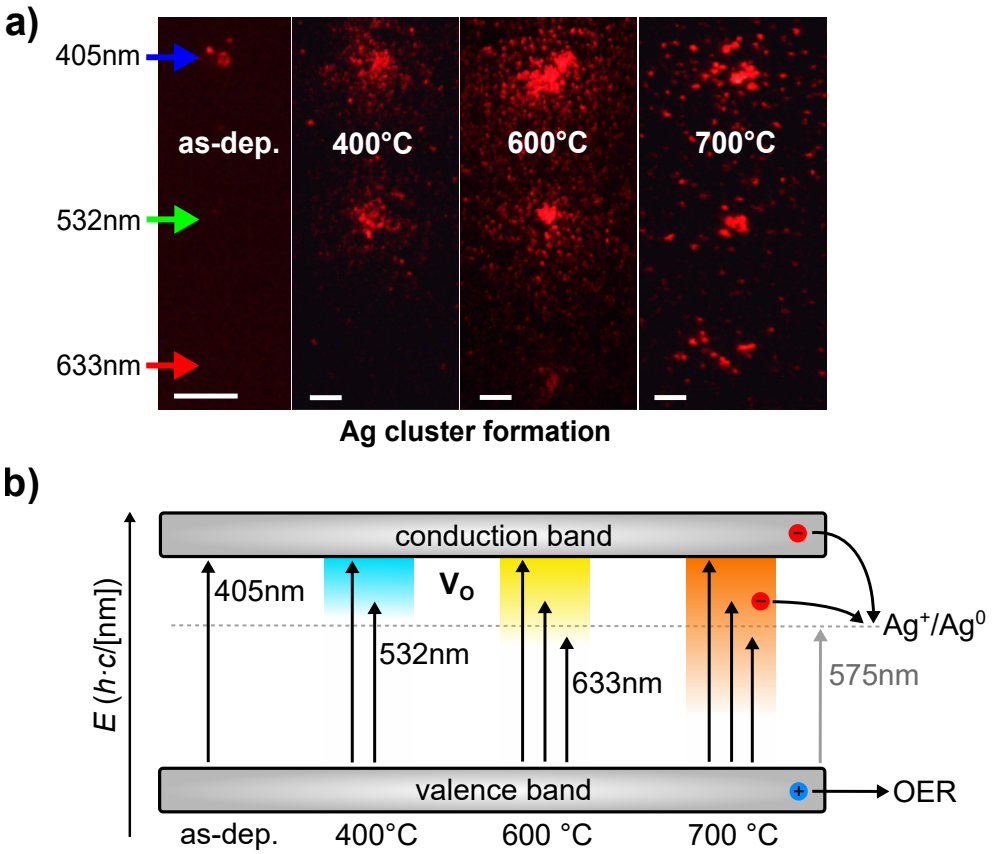

Figure 4.3: a) "Red" dark-field images showing the ability for Ag^+ photoreduction of different TiO_2 films: as-deposited and thermally annealed. The experiments were performed in 1 mM $AgNO_3$ aqueous solution consecutively using focused lasers with wavelengths 405 nm (top), 532 nm (middle) and 633 nm (bottom). The photoreduction generates Ag particles that appear as red spots. A minimum annealing temperature of 400 °C is required to drive photocatalysis at sub-bandgap excitation. The scale bars correspond to 5 µm. b) Energetic localization of V_O-states within the bandgap of TiO_2 and reduction potential for Ag^+ photoreduction and oxygen evolution reaction (OER).

With near-bandgap energy photons of $\lambda_{ex} = 405\,nm$, Ag^+ ions can be reduced to Ag on any film whereas this is only possible with 532 nm excitation on films annealed at $T_{an} \geq 400\,°C$ and with 633 nm excitation on films annealed at $T_{an} \geq 600\,°C$. A scheme of the of the energetic position of the V_O-states within the bandgap of TiO_2 is given in Figure 4.3 b). With increasing annealing temperature more states become available for photon absorption and excited electrons with energy higher than the redox potential of Ag^+ photoreduction drive the chemical reaction. [78] The successful Ag cluster formation with photons of $\lambda_{ex} = 633\,nm$ can be addressed to disorder of electronic surface states.

4.4 Identification of the Anapole Excitation by Dark-Field Spectroscopy

Having investigated the dependence of the absorption of TiO_{2-x} on the annealing temperature, a visible light photocatalytic material was obtained with high degree of control over the optical properties. However, the simulations of Figure 4.1 show that: 1) for the demonstration of the (HO)AE for absorption enhancement, k must not be zero but it should also be small where the effect of the AE is most pronounced and 2) (HO)AEs can be engineered in flat TiO_2 nanodisks even though they possess $n < 3$. This leads to the choice of $k(\lambda_p) \approx 0.03$, which was realized experimentally for $T_{an} = 600\,°C$, and reduced the disk height to 160 nm.

An SEM image of a 600 °C annealed TiO_{2-x} nanodisk array with varying radii is shown in Figure 4.4 a). For the identification of the nanodisk on (HO)AE at λ_p the scattering characteristics of the disks were analyzed with dark-field spectroscopy in water. A dark-field image of the array and the corresponding spectra of each disk are presented in Figures 4.4 b) and c), respectively. As expected, minima of scattering are not strongly pronounced owing to the low refractive index contrast at the TiO_{2-x}/water interface. However, the characteristic red-shifts of scattering minima with increasing r_d indicate that (HO)AEs are observable. [65, 63] Comparison of experimental data to the simulated scattering and absorption spectra presented in 4.4 d) allows to identify one branch of the AEs in disks with r_d ranging from 170 nm to 210 nm and another branch of HOAEs in disks with r_d ranging from 230 nm to 370 nm. In addition, the simulation results of AEs in nanodisks of different refractive indices (see also Fig. 5.2) reveal that the electrical energy/absorption maximum blue-shifts with respect to the AE related scattering minimum, which is consistent with observations in previous studies. [63, 97] In the case of TiO_{2-x}, this blue-shift is approximately 25 nm. Therefore, at λ_p, the disk with $r_d = 270\,nm$ has the HOAE scattering minimum while the disk with $r_d = 290\,nm$ exhibits the HOAE related absorption maximum. The largest disk with $r_d = 310\,nm$ is clearly not on the HOAE at λ_p and will act as a control particle to demonstrate the HOAE absorption enhancement in the single particle photocatalysis experiment.

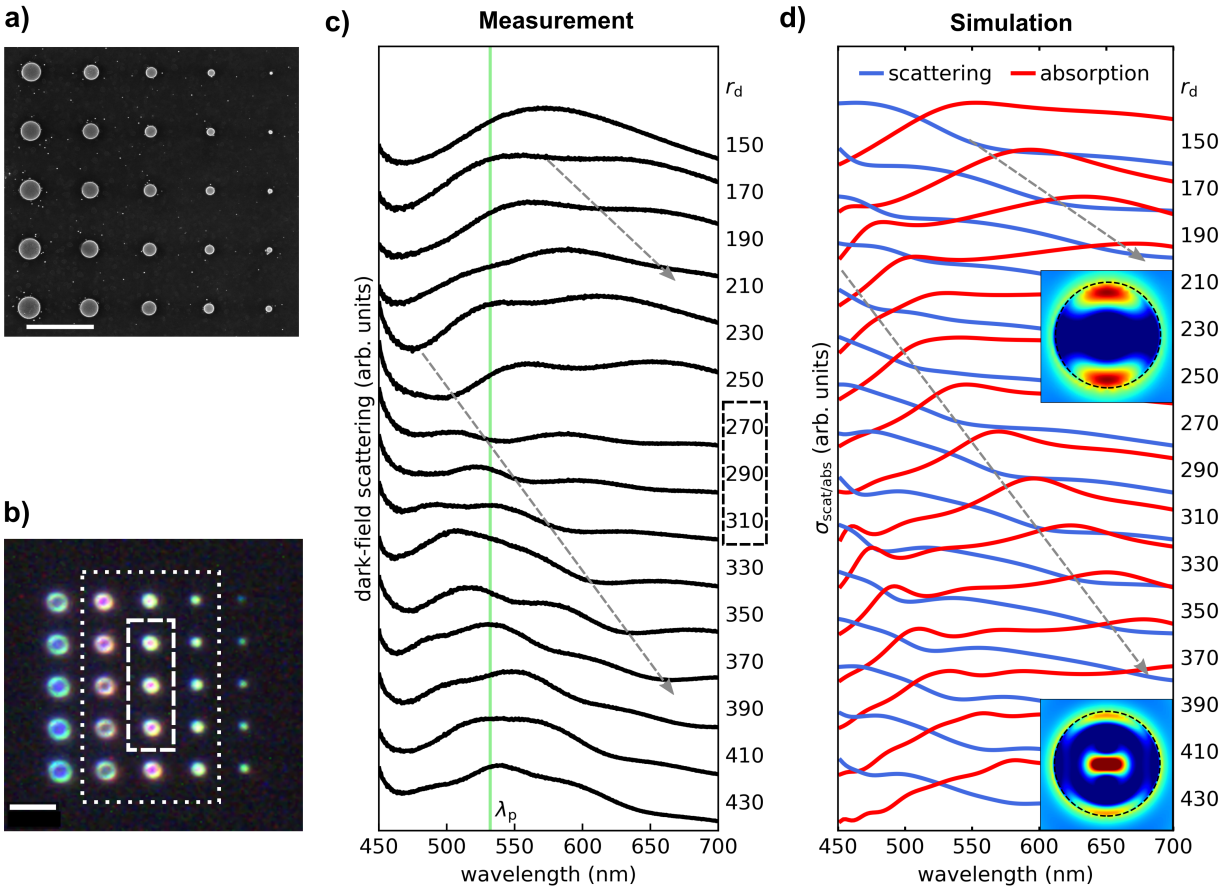

Figure 4.4: a) SEM image of a 600 °C annealed TiO_{2-x} disk array with $h_d = 160$ nm and increasing radius from top to bottom and right to left. b) Dark-field image of the disk array shown in a) in water under white light illumination. The scale bars correspond to 3 µm. c) Dark-field spectra of the disks enclosed by the dotted lines in b) with radii r_d ranging from 150 nm to 430 nm. The green line indicates the probe wavelength $\lambda_p = 532$ nm. The disks considered for the single particle photocatalysis experiments are enclosed by the dashed lines. The presence of (HO)AEs is indicated by two branches of red-shifting scattering minima as same characteristics appear in d): Simulated scattering and absorption spectra of geometrically equivalent disks taking into account the optical constants determined in section 4.2. The insets show the near-field distributions of the respective (HO)AEs.

4.5 Ag^+ Photoreduction on a Single Particle

After identifying that the disk with $r_d = 290\,nm$ has an HOAE-related absorption maximum at λ_p, it was investigated – on the single particle level – to which extent the photocatalytic activity is enhanced compared to a larger disk being off HOAE condition. The following experiment demonstrates that under (HO)AE the increased electron-hole pair generation rate accelerates the Ag^+ photo-reduction. The sample was immersed in 1 mM $AgNO_3$ aqueous solution and the disks with $r_d = (270, 290, 310)\,nm$ were excited through a water immersion objective with a focused laser at $\lambda_p = 532\,nm$ with power of 160 µW for 5 seconds each. Because the AE is robust against incident angle and polarization [65] a significant spectral shift of the HOAE is not expected by changing the irradiation condition from dark-field to a focused laser. After removal of the solution the Ag^+ reduction on the disks was analyzed by dark-field microscopy, in this case using white light illumination. As displayed in Figure 4.5 a), preferred Ag reduction was observed on the surface of the disk with $r_d = 290\,nm$ by the appearance of a bright spot that is clearly absent on disks before excitation. To confirm the reproducibility identical disks of two further arrays were excited under the same conditions. The scattering intensity profile lines across the three arrays are presented in Figure 4.5 b), elucidating enhanced scattering from the respective disks with HOAE-related absorption maximum. For chemical determination of the reaction products a SEM image with a corresponding EDX map of the excited disks was collected (Fig. 4.5 c). First, Ag (orange) as the deposited material could be verify. Second, the largest amount of Ag is located on the disk with $r_d = 290\,nm$, demonstrating its increased catalytic activity compared to the larger disk without HOAE.
To assess the absolute lower bound for the photocatalytic enhancement one can compare the geometrical cross sections A of disks with $r_d = 290\,nm$ and 310 nm. The ratio $A_{310}/A_{290} = 1.14$ indicates that similar quantities of Ag would be observed on the two different disks if the HOAE provided a 14% enhancement of the photocatalytic efficiency. Importantly, significantly more Ag was observed on the smaller disk that is on HOAE condition. This disk array can be taken as a representative indicator as it is commensurate with the optical scattering behavior of the other disk arrays examined. Although EDX is not the appropriate technique for exact elemental quantification the pronounced trend indicates that the HOAE enhancement is significantly larger than this lower bound of 14 %.

Figure 4.6 a) displays a dark-field image of all excited arrays with the top row excited for $t_{ex} = 5\,s$. The Ag coverage on all excited disks in the bottom row where $t_{ex} = 10\,s$ demonstrates a saturation effect of Ag photoreduction, also evident from the scattering profile lines shown in Figure Figure 4.6 b). A cautious assessment of photocatalytic enhancement by the AE is to integrate the EDX Ag signal over the respective disks top face areas (Fig. 4.6 c). Because the center disk (r_2) double the amount of Ag this points towards much higher enhancement factors by the presence of the AE.

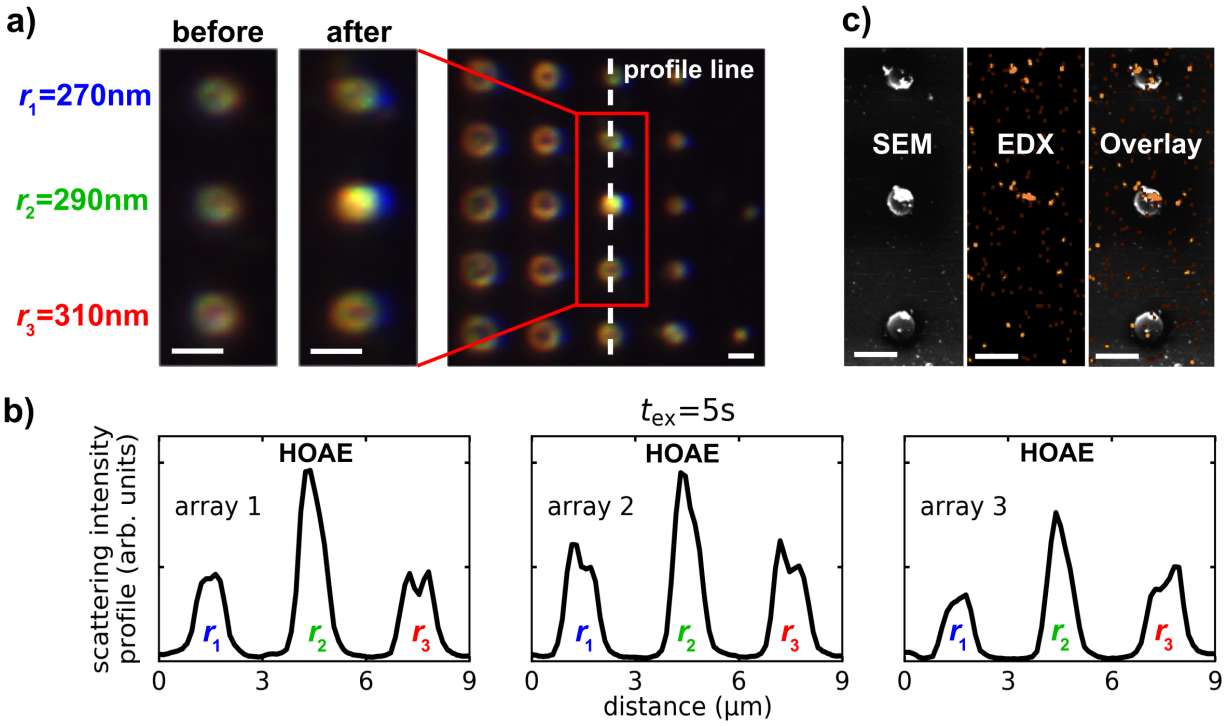

Figure 4.5: a) Dark-field image in air of the TiO_{2-x} disks employed in the single particle photocatalysis experiment before and after excitation at $\lambda_p = 532\,nm$ in 1 mM $AgNO_3$ aqueous solution. The scattering intensity of the center disk with HOAE at λ_p has increased significantly. b) Scattering intensity along the profile line over the three examined disks indicated in a) from array 1. The same experiment was carried out on two more arrays 2 and 3 with equivalent results. The scale bars correspond to 1 μm. c) SEM image and EDX elementary map of Ag (orange) and their resulting overlay of the disks shown in a). These images confirm that the scattering change arises from photoreduced Ag^+ ions and that the largest amount of Ag is observed on the center disk.

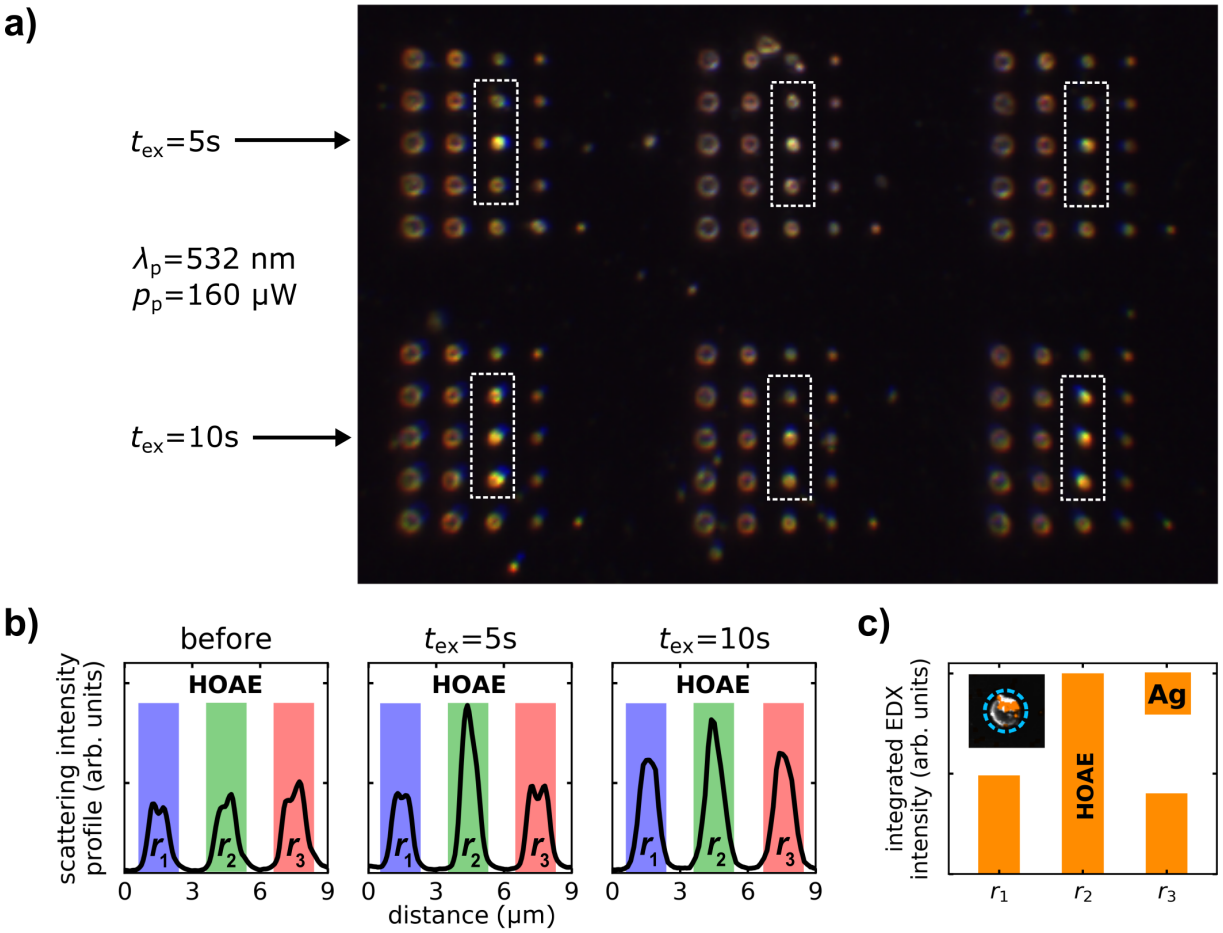

Figure 4.6: a) Dark-field image of TiO_{2-x} disk arrays in air after laser excitation ($\lambda_p = 532\,nm$, $160\,\mu W$) in 1 mM $AgNO_3$ aqueous solution. In the upper row the respective three disks enclosed by the dashed lines ($r_d = 270, 290, 310\,nm$) were excited for $t_{ex} = 5\,s$ each. All three, center disks on HOAE at λ_p exhibit enhanced scattering due to photo-reduced Ag. In the lower row t_{ex} was increased to 10 s. Because of material absorption through V_O-states also the neighboring disks without HOAE evince Ag particles, while the photoreduction starts to saturate on the middle disks once they are gradually covered. b) Scattering intensity along the profile lines according to Figure 4.5. The lines were averaged over the respective three disk arrays before and after excitation for 5 s and 10 s. c) EDX signal from array shown in Figure 4.5 integrated over the respective three disk areas indicated by the blue, dashed circle in the inset.

4.6 Experimental Details of Chapter 4

Sample Characterization The absorption of the films was measured before and after annealing at various temperatures with photothermal deflection spectroscopy (see section 3.1). This technique was employed because it allows for measuring small sub-band-gap optical absorption changes with accuracy and signal-to-noise ratio much higher than that with ellipsometry. Therefore, the extinction coefficient was calculated from the absorption, whereas the real part was measured by ellipsometry. Dark-field microscopy and imaging was performed with a confocal microscope (Witec, Germany) comprising either a water immersion objective (63×, NA = 1.0, Zeiss, Germany) or air objective (100×, NA = 0.9, Zeiss, Germany) to collect the scattered light from single disks. The sample was illuminated from the bottom with a halogen light source through an oil-immersion dark-field ultracondenser (NA = 1.2-1.4, Zeiss, Germany). For photoreduction experiments, a 650 nm long-pass filter was inserted after the light source to avoid photocatalysis driven by the dark-field lamp.

Ag Photoreduction Experiments To investigate the photocatalytic activity of the TiO_2 films before and after annealing, the Ag^+ photoreduction reaction was used, which was explained in section 3.3. The experiments were performed in 1 mM $AgNO_3$ aqueous solution ($AgNO_3$, 99.9999 %, Sigma-Aldrich; dissolved in ultrapure water), and the optical setup described above and sketched in the adjacent Figure was employed. Excitation was performed with the following CW laser: 405 nm (PicoQuant, Germany), 532 nm (Witec, Germany), and 633 nm (Witec, Germany). The CW lasers were focused on the substrate plane. During excitation, the reduced Ag atoms form small nanoparticles on the surface of the films, and they could be clearly observed owing to their large scattering cross sections. The single particle photocatalysis experiments were carried out in the same setup as the Ag photoreduction measurements by exciting single disks with the 532 nm laser and monitoring the Ag growth by dark-field scattering. After removal of the $AgNO_3$ solution, the photoreduction of Ag was confirmed by overlaying an SEM imageof the excited nanodisks with an energy-dispersive X-ray spectroscopy scan.

Simulations The simulations were carried out using Lumerical FDTD software taking into account the measured optical constants. The scattering and absorption spectra were calculated by locating a total-field scattered-field box around the nanodisks on glass and normal incident plane wave illumination.

Chapter 5

Applicability of Anapole-Assisted Absorption to Other Photocatalysts

Published in:
L. Hüttenhofer, F. Eckmann, A. Lauri, J. Cambiasso, E. Pensa, Y. Li, E. Cortés, I. D. Sharp, and S. A. Maier
"Anapole Excitations in Oxygen-Vacancy-Rich TiO_{2-x} Nanoresonators: Tuning the Absorption for Photocatalyis in the Visible Spectrum"
ACS Nano 2020, 14, 2456-2464, reference [47], publisher permission see appendix B

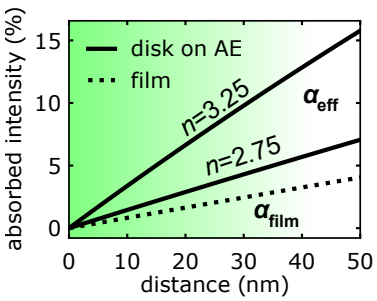

As mentioned from the outset the photocatalytic enhancement of AE in TiO_{2-x} is moderate because of its relatively low refractive index. However, it is particular for TiO_2 to have the freedom to tune the extinction coefficient whereas for other photocatalysts (e.g. GaP or $BiVO_4$) this cannot be easily done. The following analysis demonstrates how the concept of this study can be transferred to other materials.

5.1 Generalization of the Excitation Condition

During the simulation analysis of TiO_{2-x} nanodisks a trend of the anapole excitation wavelength λ_{AE} as a function of disk geometry emerged. The scaling of λ_{AE} with the geometry parameters radius r_d and height r_d is displayed in Figure 5.1 a). Doubling r_d while keeping a fixed ratio with h_d and same n causes also an approximate doubling of the λ_{AE}. Then the slopes of the fitted linear functions m_n in Figure 5.1 b) can be approximated as a multiple of n:

$$\frac{m_n}{n} \approx 1.3 \tag{5.1}$$

This allows for the definition a function for the family of lines for the disk geometry to get an AE at any wavelength and refractive index:

$$r_{\mathrm{d}}(n, \lambda_{\mathrm{AE}}) = \frac{1}{1.3} \cdot \frac{\lambda_{\mathrm{AE}}}{n} \qquad \text{with} \tag{5.2}$$

$$h_{\mathrm{d}} = r_{\mathrm{d}}(n, \lambda_{\mathrm{AE}})/1.5 \tag{5.3}$$

The coefficient in equation 5.2 depends on the ratio between r_{d} and h_{d} in equation 5.3. This ratio is used for the further analysis in this section, however also flatter nanodisks support anapole modes. [65, 63, 97, 98]

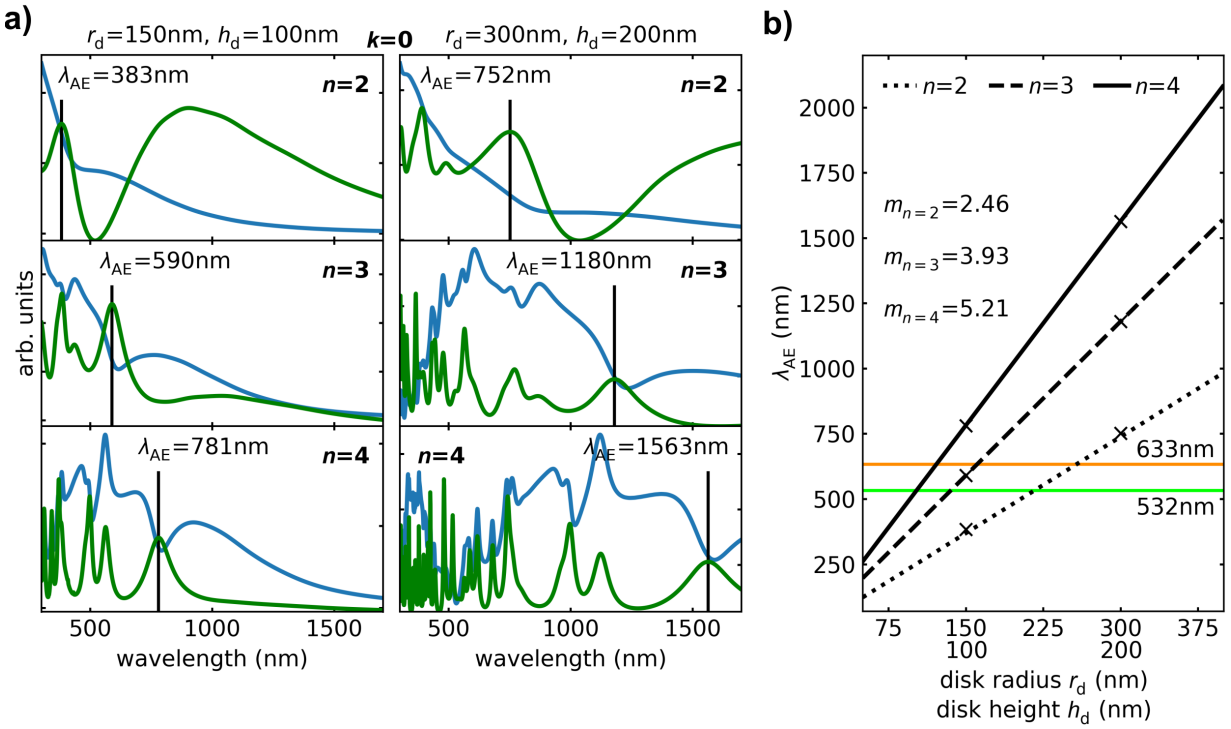

Figure 5.1: a) Simulated scattering (blue) and electric energy (green) spectra of a nanodisk in water on glass with fixed refractive index $n = 2$, 3 and 4 and k set to zero for two disks geometries: left) $r_{\mathrm{d}} = 150\,\mathrm{nm}$ and $h_{\mathrm{d}} = 100\,\mathrm{nm}$; right) the respective doubled values $r_{\mathrm{d}} = 300\,\mathrm{nm}$ and $h_{\mathrm{d}} = 200\,\mathrm{nm}$. Here λ_{AE} denotes the wavelength of the maximum of electric energy corresponding to the scattering minimum. b) Data points of λ_{AE} and disk radius and height fitted with linear functions with slopes m_{n}.

5.2 Validation of the Dependence Function

The linear fitting of the pairs of data points to obtain $\lambda_{AE}(r_d, h_d, n, k)$ is a presumption that needed to verified. As a validity check, Figure 5.2 shows scattering and electric energy spectra of disks with varying parameters. For n = (2, 2.5, 3, 3.5, 4), the geometry of the disk is adjusted such it supports AE at λ_{AE} = 532 nm (a) and 633 nm (b) discernible by a minimum of scattering and maximum of electric energy. If k is increased λ_{AE} does not vary significantly such it is not taken into account in equations 5.2 and 5.3.

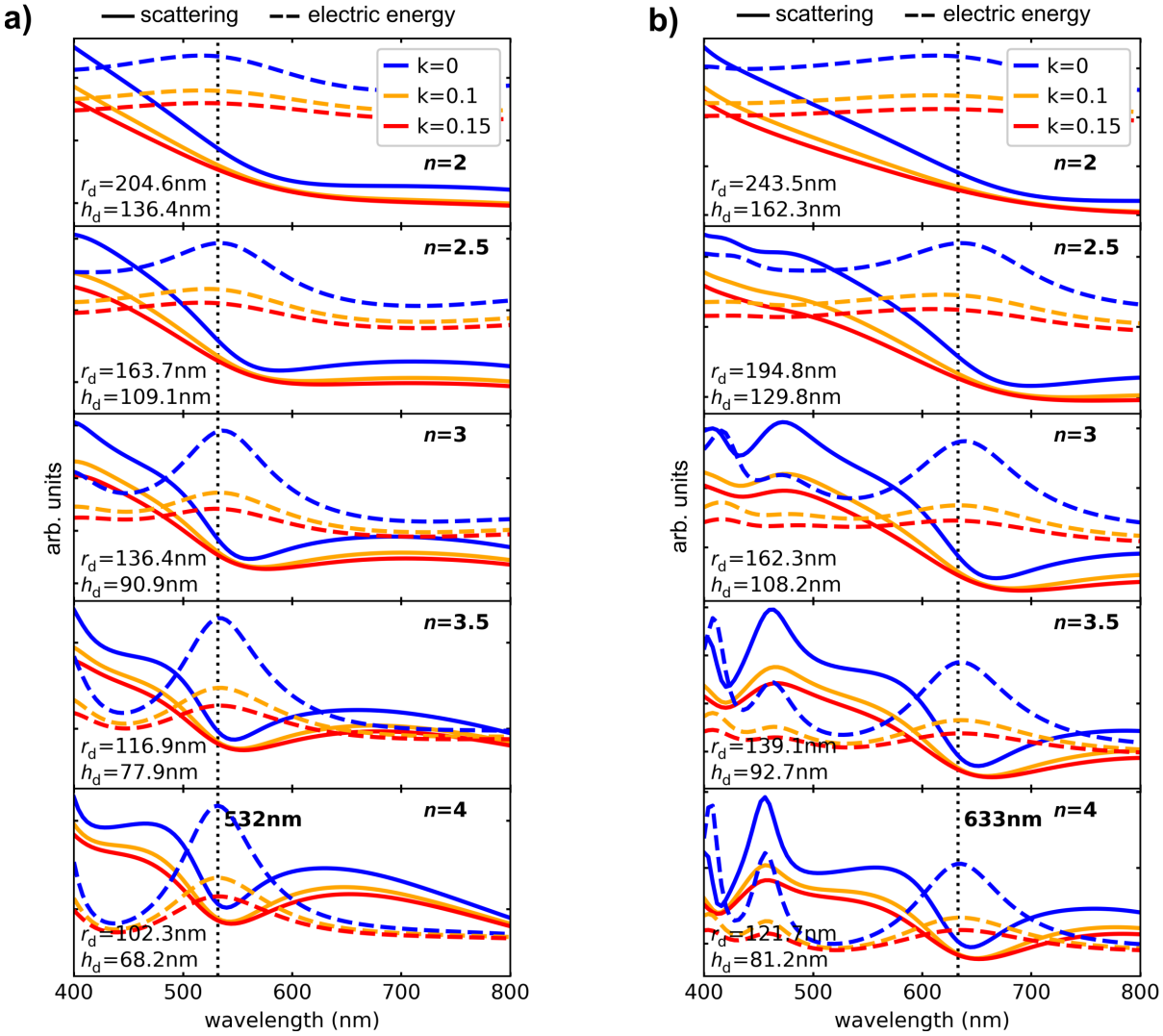

Figure 5.2: a) Test simulations of scattering (solid lines) and electric energy (dashed lines) spectra to confirm validity of equations 5.2 and 5.3. b) Also the design of a disk with λ_{AE} = 633 nm is possible for arbitrary refractive indices.

The tests demonstrate that equations 5.2 and 5.3 are a valid basis for further investigation on anapole assisted absorption enhancement in other photocatalysts.

5.3 Figure of Merit

The extensive numerical simulations presented in the previous sections revealed a simple empirical relationship between the disk geometry and the refractive index such that an AE can be supported at any desired wavelength given by the equations 5.2 and 5.3. These findings allow for calculating the absorption efficiency of a nanodisks on AE at λ_p with arbitrary optical constants on glass ($n = 1.4$) in water (Fig. 5.3 a). As normalization, the simulation was re-performed for a film with the same respective optical constants but with fixed height $h_f = 136\,\text{nm}$ (Fig. 5.3 b). The resulting relative absorption enhancement in Figure 5.3 c) shows that for $n \approx 3.25$ and $k \approx 0.035$ a nanodisk on AE can absorb more than twice as much light as a 50 % thicker film. This is particularly beneficial for photocatalysis with metal-oxides because the majority of electron-hole pairs excited in the bulk of the catalyst do not contribute to photocatalysis due to their typically short carrier diffusion lengths ($\sim 5 - 50\,\text{nm}$) and rapid recombination before reaching the surface, which constitutes a major efficiency limiting factor. [15, 66, 30]

As an alternative measure it is also possible to calculate an effective absorption coefficient α_{eff} of a disk on AE and compare it to the absorption coefficient of the film α_{film} with the same $k = 0.035$ which can be simply calculated by:

$$\alpha_{\text{film}} = \frac{4 \cdot \pi \cdot k}{\lambda_p} = \frac{4 \cdot \pi \cdot 0.035}{532\,\text{nm}} = 8.3 \times 10^3\,\text{cm}^{-1} \tag{5.4}$$

Figure 5.3 c) indicates the relative absorption enhancement (RAE) of the absorption efficiency σ_{abs} as a function of r_d and h_d such

$$A_d(z = h_d) = RAE \cdot A_f(z = h_f) \tag{5.5}$$

with $A_{d/f}$ being the absorbance of the disk/film as a function light propagation depth z Here, arbitrary materials with identical optical constants and geometrical cross sections are compared such film and disk are assumed to have the same reflectance, so A relates to transmittance (T) simply as

$$A = 1 - T \tag{5.6}$$

Inserting equation 5.6 into 5.5 and using the Lambert-Beer-Law for the absoprtion coefficient $T(z) = e^{-\alpha \cdot z}$:

$$1 - T_d(z = h_d) = RAE \cdot (1 - T_f(z = h_f)) \tag{5.7}$$

$$\alpha_{\text{eff}} = -\frac{1}{h_d} \cdot \ln(1 - REA \cdot (1 - e^{-\alpha_f \cdot h_f})) \tag{5.8}$$

For $n = 3.25$, which corresponds to $RAE = 2.5$, $r_d = 135\,\text{nm}$ and $h_d = 90\,\text{nm}$, $\alpha_{\text{eff}} = 34.3 \times 10^3\,\text{cm}^{-1}$ is over four times larger than the absorption coefficient of the film α_f with

the same k. This infers that the AE-assisted confinement of the absorption volume to nanoscaled structures enables enhanced electron-hole pair creation rates close to the catalyst surface (Fig. 5.3 d). In addition, a densely packed resonator metasurface also would exhibit a larger surface area than a film, thereby allowing for greater loading of active sites and higher reaction rates.

To get an overview on the applicability to other materials with photocatalytic potential, the materials ZnO, WO_3, $BiVO_4$, GaP and TaON are inserted onto Figure 5.3 c) according to their known optical constants. The values of n and k are listed in Table 5.1. GaP, TaON and $BiVO_4$ appear to be promising candidates for employing AEs because of their catalytic activity and high refractive index. In particular, GaP has been shown to have reactivity for CO_2 to methanol reduction. [99, 100] Although carrier diffusion lengths in GaP are typically on the order of micrometers [101], photoelectrochemical and photocatalytic conversion efficiencies are restricted by the even larger optical absorption depth due to the indirect bandgap of the material. The confinement of absorption volume into doped GaP nanostructures assisted by resonant coupling of AE to the indirect bandgap electron-hole pair excitation appears as an intriguing way to overcome the mentioned efficiency limitations.

Material	n	k	Ref.
TiO_{2-x}	2.3	0.0-0.1	this work
ZnO	2.15	0.008	[98]
WO_3	2.2	0.1	[15]
$BiVO_4$	2.54	0.013	[102, 103]
GaP	3.5	0005	[104]
TaON	2.7	0.03	[105]

Table 5.1: Values of the refractive index n and the extinction coefficient k of photocatalytic semiconductors at $\lambda = 532\,\text{nm}$. The materials are inserted onto Figure 5.3 c).

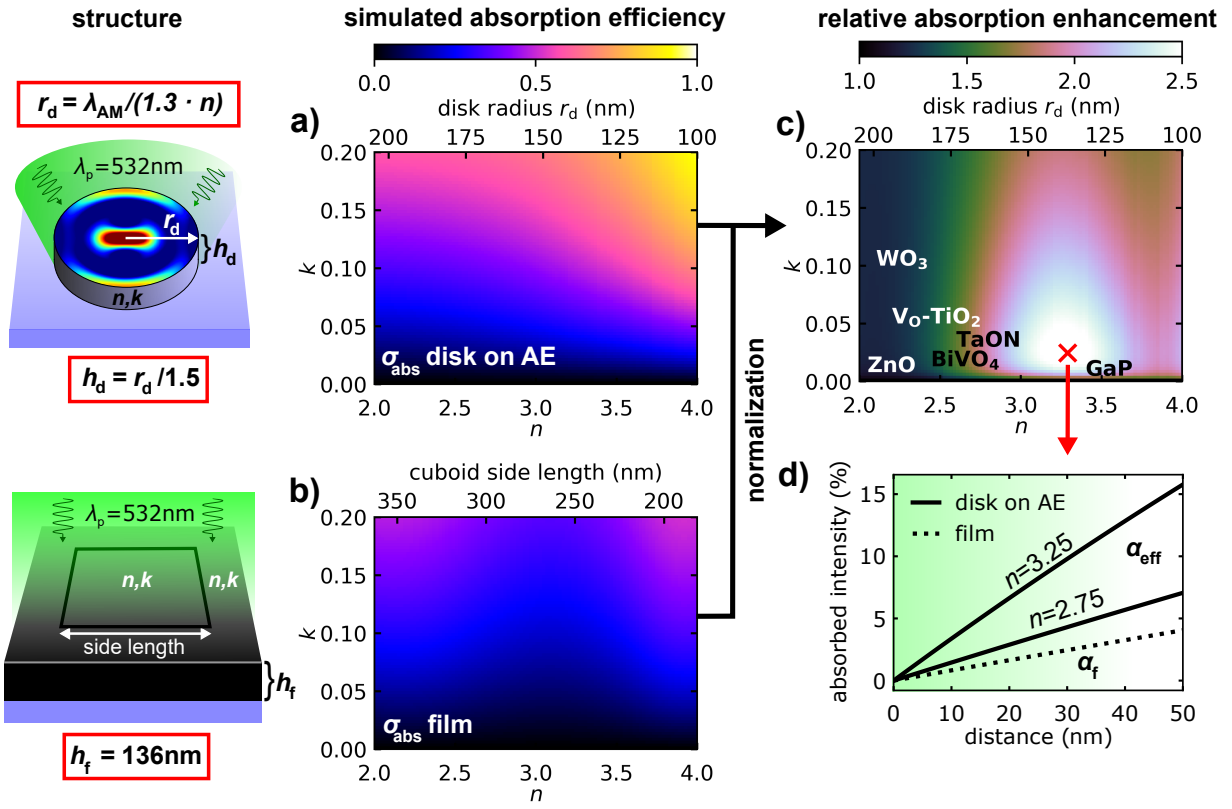

Figure 5.3: a) Simulated absorption efficiency of a nanodisk at λ_p as a function of the optical constants n and k, connected to the disk geometry by equations 5.2 and 5.3. b) Corresponding result for a film with constant height $h_f = 136\,\text{nm}$. c) Relative absorption enhancement computed by the ratio between a) and b). Several catalytic materials are embedded to demonstrate the respective applicability of AE absorption enhancement. d) Light absorption in an exemplary catalyst surface with thickness of typical charge carrier diffusion lengths. α_{eff} and α_{film} denote the effective absorption coefficient of a disk on AE and a film, both materials having the same $k = 0.035$.

5.4 Simulation Details of Chapter 5

The scattering cross sections are determined as described in section 4.6. The electric energy inside the disk was obtained by integrating $W_E = \frac{n^2}{2}\int |E|^2 dV$. For the calculations of a film, the total-field scattered-field box was located within the film and the size was chosen such that it covers the same cross section as the equivalent disk.

Chapter 6

Arrays of Coupled Amorphous Gallium Phosphide Nanodisks

Published in:
L. Hüttenhofer, A. Tittl, L. Kühner, E. Cortés, and S. A. Maier
"Anapole-Assisted Absorption Engineering in Arrays of Coupled Amorphous Gallium Phosphide Nanodisks", *ACS Photonics* 2021, 8, 1469-1476, reference [106], publisher permission see appendix B

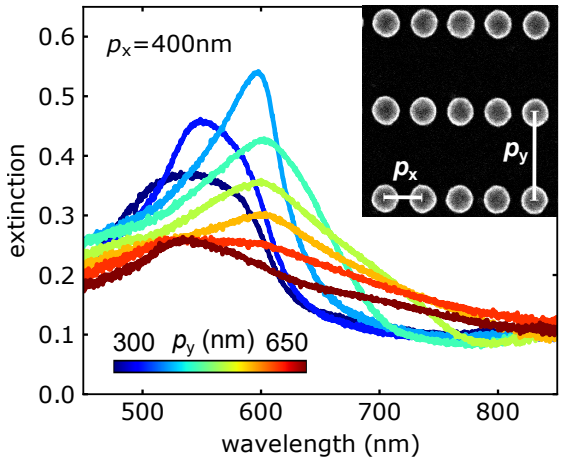

The previous sections demonstrated that if the underlying material exhibits losses, as in the case of TiO_{2-x}, the anapole increases the absorption of individual resonant particles and enhanced photocatalytic activity can be observed at sub-bandgap excitation wavelengths. Furthermore, high index SPCSs undergo stronger AE-assisted absorption enhancement. In order to realize high-efficiency energy conversion for practical applications, these nanophotonic approaches have to be combined with advances in large-area nanofabrication, [107, 108, 109] allowing pushing nanophotonics from the single-particle level to a next generation of microscopically engineered, upscaled devices. [110, 111] High loading of catalytic sides and large active surface demand close spacing of nanoresonators to fully develop their performance in terms of chemical yields, compared to planar films. The influence of lattice effects in arrays of nanoresonators has been subject to previous studies, showing strong impact on the overall optical response. [61, 112, 113, 46] However, only a few studies shed light on interactions between an ensemble of particles – each supporting the anapole – once placed in close vicinity. [114, 115]

This section investigates the effects of lattice coupling on optical anapole supporting nanodisks arranged into rectangular arrays with a gradual variation of the center-to-center spacing with respect to the polarization axis of the incident light. The nanostructures are fabricated from amorphous gallium phosphide (a-GaP), a prominent high-index material with applicability for second-harmonic generation [116, 117] and photocatalysis. [27, 14] The complex refractive index and its dependence from the temperature during sputtering is shown in Figure 6.1. Focusing on the absorption capability, is the system is analyzed by means of extinction spectroscopy and corresponding FDTD simulations in the (lossy) visible spectral regime of a-GaP grown at 350 °C.

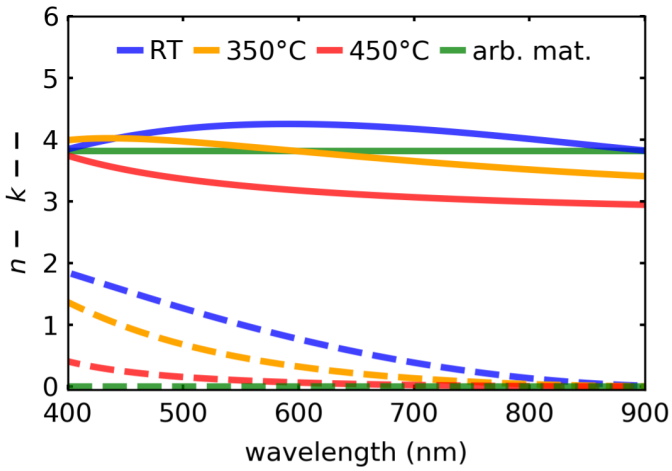

Figure 6.1: Complex refractive index of a-GaP for different growth temperatures during sputtering measured by spectral ellipsometry and arbitrary material (arb. mat.) with non-dispersive optical constants $n = 3.8$ and $k = 0$.

The findings reveal that anapole-assisted absorption of a single nanodisk at λ_{AE}=600 nm is enhanced by up to 300% once embedded in a 2D array with an optimum center-to-center distance of 400 nm. The physical origins of this effect is further analyzed with polarization-dependent spectroscopy on a 1D particle chain, which allows to differentiate between parallel and perpendicular coupling with respect to the light polarization axis. Excellent agreement between measurements and simulations enables the association of the far-field behavior with the lattice influence on the electric and toroidal dipole resonances accessed by multipolar decomposition of the electromagnetic near field inside the nanodisks. By tailoring the spectral position of both the single-particle resonance through material choice and geometry as well as the lattice effect through particle arrangement, this section provides instructive design guidelines and can be extended to a variety of photonic applications that require high-field densities within matter.

6.1 Experimental Setup

First, a system of a two-dimensional, rectangular array of a-GaP nanodisks with varying center-to-center distances (pitches) $p_{x/y}$ along the respective axes is simulated (Fig. 6.2a). A plane wave that is linearly polarized along the x-axis illuminates the structure from the bottom through the SiO_2 substrate. Each nanodisk a has radius $r = 130\,\text{nm}$ and height $h = 50\,\text{nm}$ such that it supports an anapole excitation (AE) at $\lambda_{AE} = 600\,\text{nm}$. More simulation details are given in section 6.5. The intensity profile of the electric field $|E(\lambda_{AE}, x, y, z)|^2$ inside the nanodisks is modified by the strong damping related to the high losses of the material. Taking into account the complex refractive index of a-GaP, it can be visualized by the spatially resolved absorbed power profile calculated by

$$a(\lambda, x, y, z) = -\frac{\pi c}{\lambda} \cdot 2nk \cdot |E(\lambda, x, y, z)|^2 \tag{6.1}$$

with λ being the wavelength of the driving field and c the speed of light (see Eq. 1.3). The anapole-assisted absorption enhancement at λ_{AE} is displayed in Figure 6.2 b) by means of the spatially integrated absorbed power

$$A(\lambda) = \frac{1}{P_{tot}} \int a \, \mathrm{d}V_{disk} \tag{6.2}$$

with P tot being the total power emitted by the source and V_{disk} the volume of the nanodisk, in comparison to an a-GaP film with thickness h. As expected, the intrinsic material losses lead to a broad and weakly pronounced absorption enhancement.

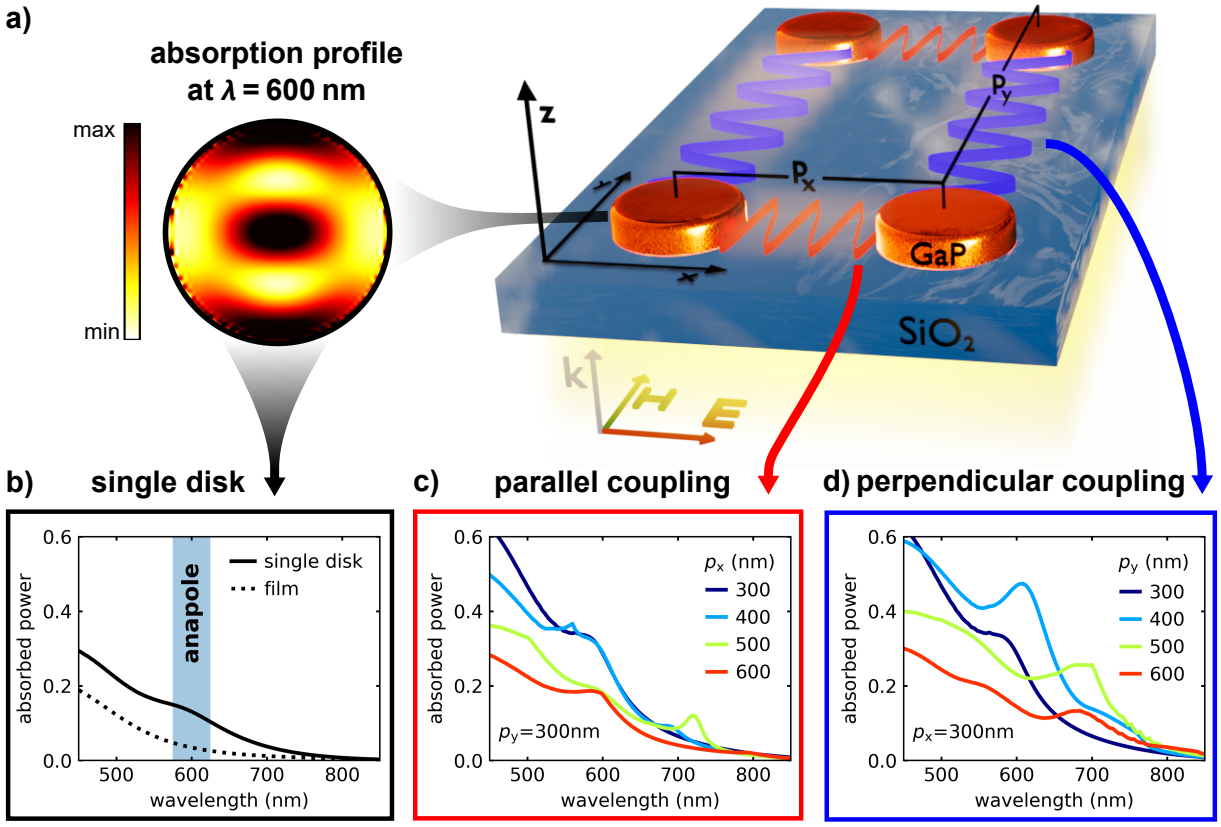

Figure 6.2: a) An infinite array of amorphous GaP nanodisks on a SiO_2 substrate is illuminated by a x-polarized broadband light source from the bottom in the z-direction. A single, isolated disk supports an anapole excitation at $\lambda = 600\,\text{nm}$. The absorption profile of the horizontal cross section at $z = 20\,\text{nm}$ presents the typical electric near-field mode profile of the anapole due to defect-related material losses. In addition to the anapole, the nanodisks interact via parallel and perpendicular coupling with respect to the polarization axis. b) The anapole-mediated electric field enhancement inside the disk increases the particle absorption compared to a nonresonant film. c), d) Effects of array coupling on the absorption spectra of an individual nanodisk embedded in an infinite array. The pitch between the disks $p_{x/y}$ (center-to-center distance in the x- and y-direction, respectively) tunes the coupling modes that interfere with the anapole and lead to further enhanced absorption.

6.2 2D arrays: Observation of Anapole-Anapole Interaction Asymmetry

Arranging the nanodisks in an array causes a drastic change of the absorbed power A. Figure 6.2 c) shows the simulated absorption spectrum of a single particle with constant nearest neighbor spacing $p_y = 300\,\text{nm}$ perpendicular and variable p_x parallel to the polarization axis. Small p_x enhance the lattice-induced absorption, which decreases with particle separation. In turn, if p_x is fixed to 300 nm (Fig. 6.2 d), the variation of p_y causes a strong amplification of the anapole-assisted absorption, which peaks at $p_y = 400\,\text{nm}$. This phenomenon is attributed to grating effects or Rayleigh anomalies, which are well studied for arrays of plasmonic particles with strong dipolar resonances, [118, 119] showing significant increase of the array extinction once the individual resonance of the particle is merged with the grating resonance. [120, 121] In rectangular arrays and at normal incidence of light the additional coupling mode arises at the wavelength

$$\lambda_c = n_s \cdot \left[\left(\frac{i}{p_x} \right)^2 + \left(\frac{j}{p_y} \right)^2 \right]^{-\frac{1}{2}} \tag{6.3}$$

with n_s being the refractive index of the substrate and i, j the grating order. Under this condition, the dipolar fields of the individual particles interfere to form collective oscillations and the in-phase addition of the scattered light fields increases the optical power in the plane of the array. [122, 123] Even though the resonant particles are dielectric in our study, similar behavior is observed, which is assigned to a strong contribution from the ED to the excitation of the anapole state that spectrally overlaps with the TD.

The numerical results are confirmed experimentally by fabricating anapole disk arrays with different pitch variations (see 8.2 and 8.3) and performing optical extinction spectroscopy measurements described in section 6.5. Figure 6.3 a) shows a microscope image of the whole 2D array fabrication design with in total 8×8 arrays of 50×50 nanodisks each, where the values of p_x and p_y gradually increase in steps of 50 nm. Figure 6.3 b) displays scanning electron microscopy (SEM) images of the fabricated GaP nanodisk arrays with the smallest and largest particle pitches of 300 and 650 nm in the x- and y-direction.

The measured extinction integrated from 575 to 625 nm, *i.e.* the spectral range around λ_{AE} in a single GaP nanodisk. Figure 6.4 a) displays the obtained values as a function of p_x and p_y with a color map. The anapole array with p_x=p_y=400 nm clearly exhibits maximum extinction. Furthermore, maintaining $p_y = 400\,\text{nm}$ stabilizes high extinction also for small and intermediate values of p_x , opening up a broad design range for efficiently absorbing anapole arrays. This somewhat asymmetric behavior demonstrates different coupling strengths along the x- and y-axis of the array and clearly indicates the directionality of anapole- anapole interactions, as will be explained in more detail later. For a consistency check the same arrays were measured with the polarization rotated by 90° (Fig. 6.4 b). As

expected, the color maps is mirrored at the diagonal of the plot.

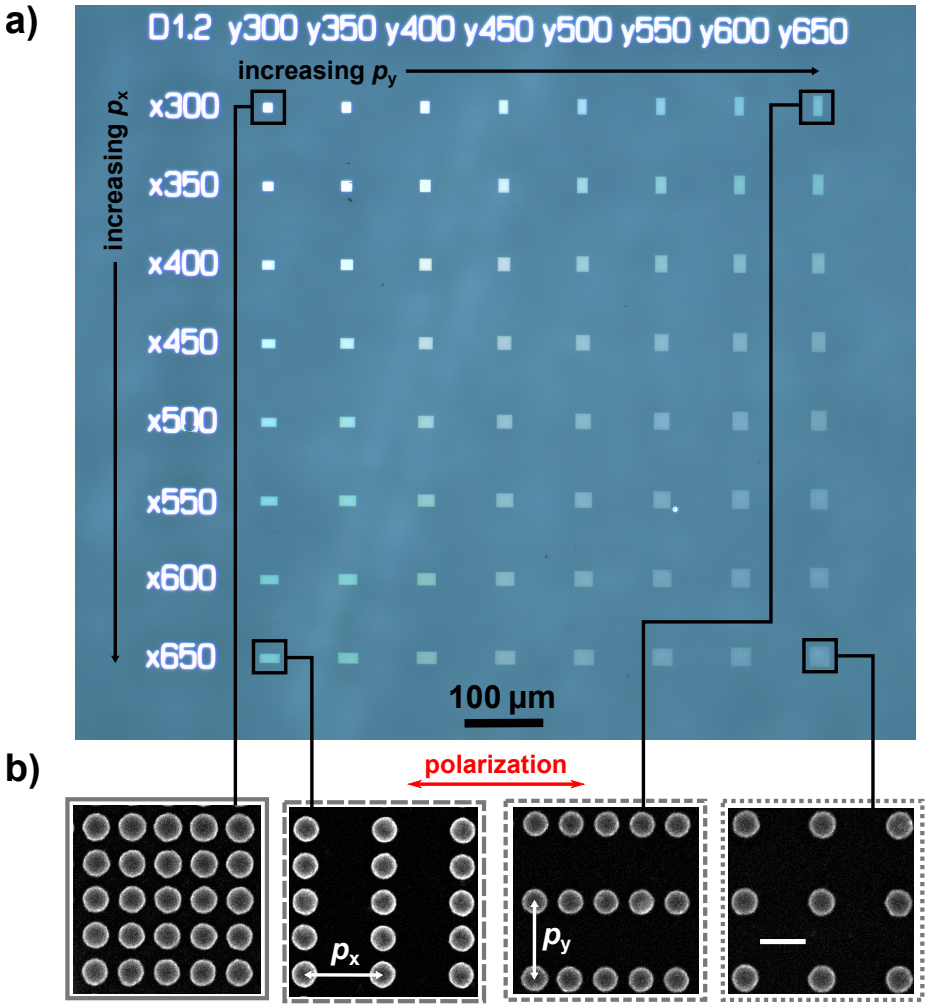

Figure 6.3: a) Microscope image of the sample with all 2D arrays each consisting of 50×50 nanodisks. p_x and p_x denote the center-to-center distance in the x- and y-direction, respectively. b) SEM images of single arrays. In the images p_x and p_y take values of 300 and 650 nm and represent the measured arrays shown at the corners of Figure 6.4 b) indicated by the gray frames. The scale bar corresponds to 500 nm.

The same asymmetry as in a) is also observed in the simulation of integrated absorption of a single nanodisk (A) embedded in an array (Fig. 6.4 c). Although the maxima of the color maps do not fully coincide, the otherwise excellent agreement between measurement and simulation demonstrates that, first, the increased extinction is caused by the lattice-induced amplification of the anapole-assisted absorption enhancement, which is underlined by an exemplary simulation of transmittance, reflectance, and absorbance for p_x=p_y=400 nm (Fig. 6.4 d). Second, the experimentally observed directionality of anapole-anapole interactions is numerically reproducible.

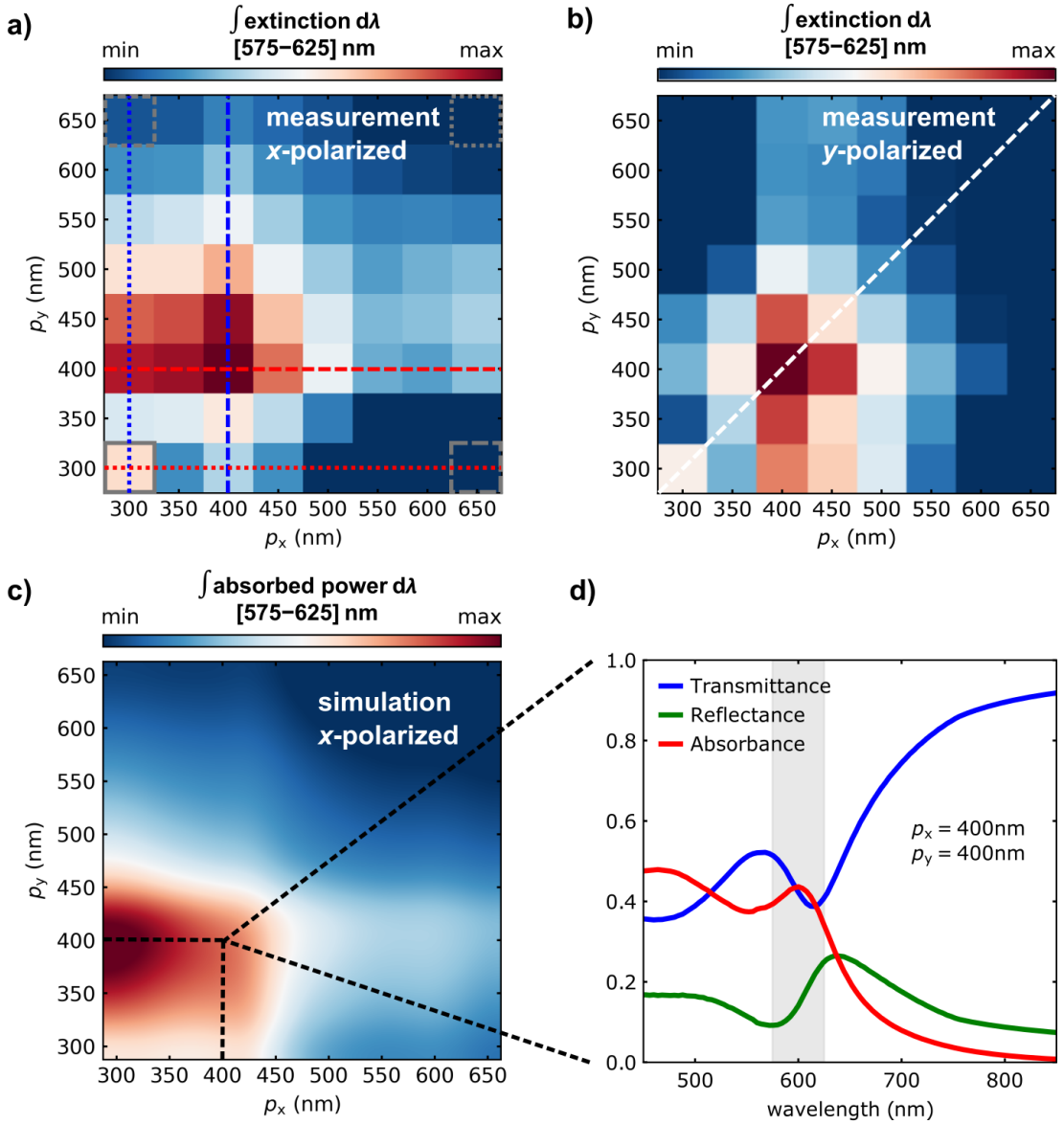

Figure 6.4: a) Color plot of the integrated extinction (1−transmittance) of 2D arrays, each consisting of 50×50 nanodisks, for all permutations of $p_{x/y}$. The dashed lines indicate the series of spectra displayed in Figure 6.5. b) Consistency check by integrated extinction of 2D arrays with polarization rotated by 90°. Compared to polarization of 0° the interaction asymmetry is mirrored at the diagonal (white dashed line). c) Simulation of absorbed power in a single nanodisk embedded in an infinite 2D array. d) Exemplary simulation of transmittance, reflectance and absorbance of an array with $p_x = p_y = 400\,\text{nm}$. The reduced transmission from 575-625 nm is caused by enhanced absorption.

Figure 6.5 shows series of spectra from which the integrated extinction values were obtained, indicated by the dashed lines in Figure 6.4 a). The variation of p_y (Fig. 6.5 a) exhibits a spectrally tunable character of the extinction maximum as λ_c shifts over λ_{AE}. In turn, varying p_x shows a stronger extinction enhancement for small values and less spectral variation of the maxima. The data also reveals that the integrated extinction with $p_x = p_x = 400\,\text{nm}$ nearly doubles the value at the densest spacing of $p_x = p_x = 300\,\text{nm}$ (Fig. 6.5 c, d). This demonstrates that engineering the specific arrangement of the array with respect to the polarization axes allows for tailoring the interactions between the anapoles and opens an additional degree of freedom for controlling light on the nanoscale.

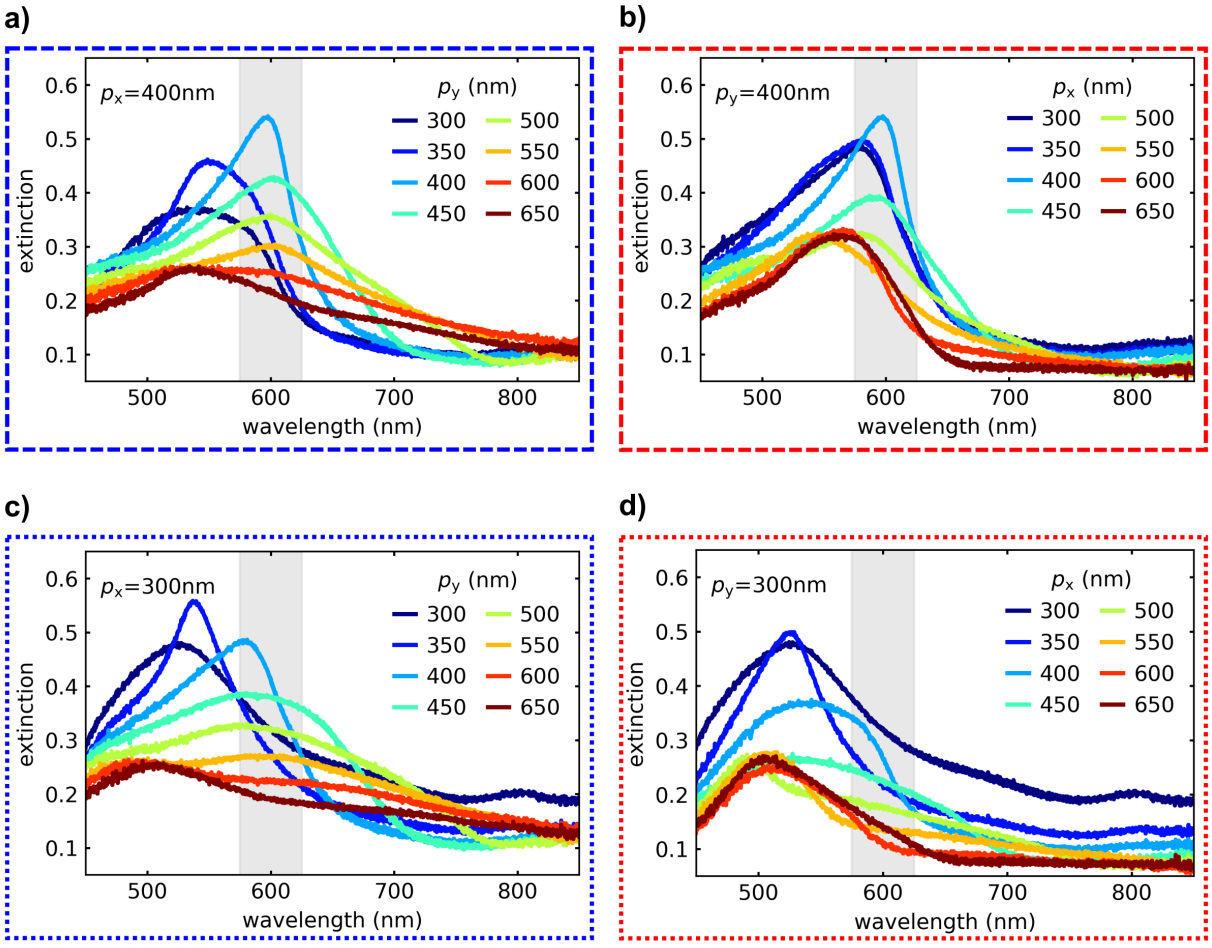

Figure 6.5: a) Extinction spectra of 2D arrays with $p_x = 400\,\text{nm}$ and variation of p_y. The gray-shaded area denotes the integration range used for the calculation of the data presented in Figure 6.4 c). b) Spectra analogous to a), but p_y=400 nm and variation of p_x. The highest extinction within 575-625 nm is achieved by setting $p_x = p_y = 400\,\text{nm}$. c),d) Extinction spectra for $p_{x/y} = 300\,\text{nm}$ and variation of $p_{y/x}$.

Furthermore, one key parameter for photocatalytic energy conversion is the amount of visible light absorbed in the surface layer of the catalyst, with the surface layer being the surface volume with a thickness on the order of the charge carrier diffusion length after photoexcitation. As discussed in chapter 5, apart from c-GaP, [101] this diffusion length of common photocatalysts mentioned above is typically only 5–50 nm [30] such that electron-hole pairs recombine before reaching the surface. Together with the weak visible light absorption, this constitutes one of the main limiting factors for photocatalytic solar energy conversion efficiency in the underlying materials. Integrating the measured extinction with $p_x = p_y = 400\,\text{nm}$ (Fig. 6.5 a) from 400 to 700 nm and normalizing by the terrestrial sunlight spectrum results in $\approx 34\,\%$ of light harvested, neglecting the minor contribution from reflections. Notably, this is achieved with 50 nm thick structures at sub-bandgap illumination, maximizing the production of carriers at the surface and, thus, making the arrays highly reactive compared to a thick film with the same absorption.

6.3 Separating Interaction Mechanisms in 1D chains

For a deeper analysis of anapole-anapole interactions, the dimensionality of the arrays (2D) is reduced to isolated chains (1D) of nanodisks with the same r and h, separated by the pitch p (center-to-center distance), as shown in the SEM images in Figure 6.6 a). This allows for rigorous separation of the coupling mechanisms by changing the polarization between perpendicular and parallel with respect to the chain axis. The measurements on the 1D chains (Fig. 6.6 b) have a similar character as the 2D counterparts: In x-polarization, the extinction exhibits a maximum at $p = 400\,\text{nm}$, whereas in y-polarization, it gradually increases as p is reduced. This effect of the difference of coupling directionality is reproduced in the corresponding simulated spectra of the absorbed power A (Fig. 6.6 c). The dashed lines indicate the theoretical spectral position of $\lambda_c(p)$ to emphasize the different impact of the chain on the anapole-assisted absorption. The nonappearance of the sharp absorption peak for p=350 nm and y-polarization in the extinction spectra is attributed to the relation between high sensitivity of λ_c to the angle of incidence and the slight divergence of the illumination source. This issue is addressed in more detail in section 6.5.

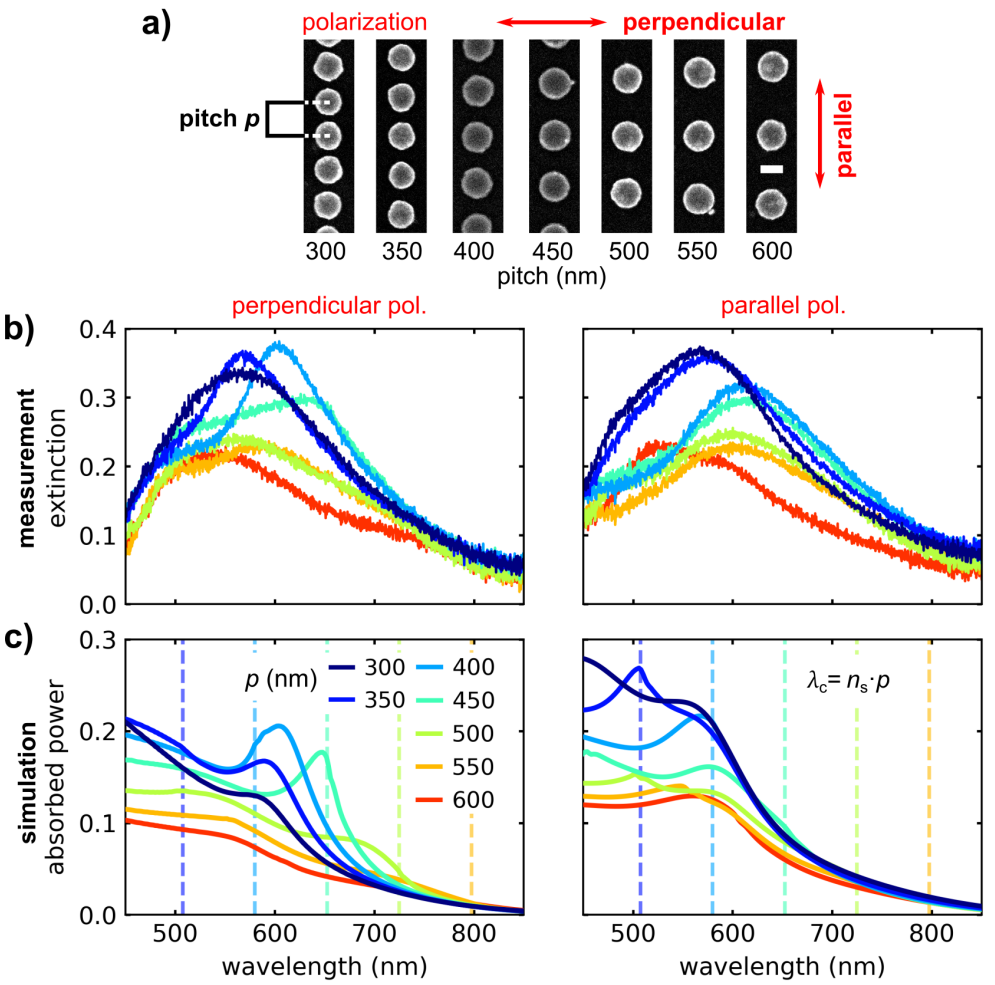

Figure 6.6: a) SEM images of 1D chains of a-GaP nanodisks. The pitch p is varied from 300 to 600 nm nanometers, while the disk radius is unchanged. The red arrows indicate the polarization directions of the incident beam employed in the simulations and extinction experiments. The scale bar corresponds to 200 nm. b) Experimental extinction spectra of the 1D array of disks with different pitches. c) Corresponding simulated absorbed power spectra. The dashed lines indicate the grating coupling wavelength λ_c, color-coded to the respective p. In perpendicular polarization, the highest absorption performance is clearly observed for p = 400 nm, whereas in parallel polarization at the smallest p, indicating a fundamental difference of the type of anapole couplings.

6.4 Multipolar Decomposition in Coupled Nanodisks

The sound agreement between measurement and simulation in the 1D case allows directly connecting macroscopic entities, *i.e.*, absorption and extinction, to the lattice effect on the electric near fields and associated Mie modes. Figure 6.7 a) shows the electric near-field intensity profile at $z = h/2 = 25$ nm and λ_{AE} from the simulations shown in Figure 6.6 c). For large pitches, the nanodisks display the characteristic intensity profile of the anapole.

With perpendicularly polarized light, this profile intensifies with decreasing p, with a maximum at $p = 400\,\mathrm{nm}$. In parallel polarization, there is no maximum, but a strong increase of the near fields at the edges and in between the nanodisks can be observed once they approach the short-range coupling regime. [124]

The simulated near fields are also used to calculate the currents for obtaining the far-field scattering contributions from the fundamental electric, toroidal, and magnetic dipole oscillations, as described in section 2.2. Figure 6.7 b) displays the multipolar decomposition of an isolated nanodisk. In the left panel the underlying material is a-GaP; in the right an arbitrary, lossless (k=0) material with a nondispersive refractive index of $n = 3.8$, corresponding to $n_{\text{a-GaP}}(\lambda_{\text{AE}})$, also illustrated in Figure 6.1. In both cases, the spectral position of the anapole is nearly the same, located at the minimum of the ED and the onset of the TD. [76] The MD is shifted toward the UV due to the low height of the nanodisk, [60] and its contribution can therefore be neglected. The intrinsic material losses of a-GaP blur the Mie modes, but the high refractive index still enables the identification of the anapole state.

To get the full picture of the lattice effect on the Mie modes, colormaps of the ED and TD far-field scattering power of nanodisks embedded in a 1D chain as a function of wavelength and pitch are plotted in Figure 6.7 c). Because of their difference in magnitude, the ED and TD panels are normalized to their respective maxima. For perpendicular polarization (top panels) the lattice effect is most pronounced for the ED. Decreasing p blue-shifts and enhances the long-wavelength ED maximum toward the anapole. Also, the TD gains intensity around $p = 450\,\mathrm{nm}$. This trend becomes more obvious in the corresponding plot for the arbitrary material with $n = 3.8$ and $k = 0$, shown in Figure 6.8. In the lossy case, the lattice-induced scattering enhancement of the ED and TD is attenuated at lower wavelengths by the material losses, which becomes significant for lower values of the pitch. This results in maximum absorption once λ_{c} coincides with λ_{AE}. In parallel polarization (Fig. 6.7 c), bottom) the situation is more complex. Again, the results are compared with studies about interactions of *plasmonic* particles arranged in a 1D chain. [124, 125] Polarization parallel to the chain axis enables efficient energy transfer between the particles involved, which is related to the steady increase of absorption when reducing the particle distance. At the same time, the lattice effects on the ED and TD do not promote an interference of λ_{c} with λ_{AE}, as indicated by the red dashed lines in Figure 6.7 c).

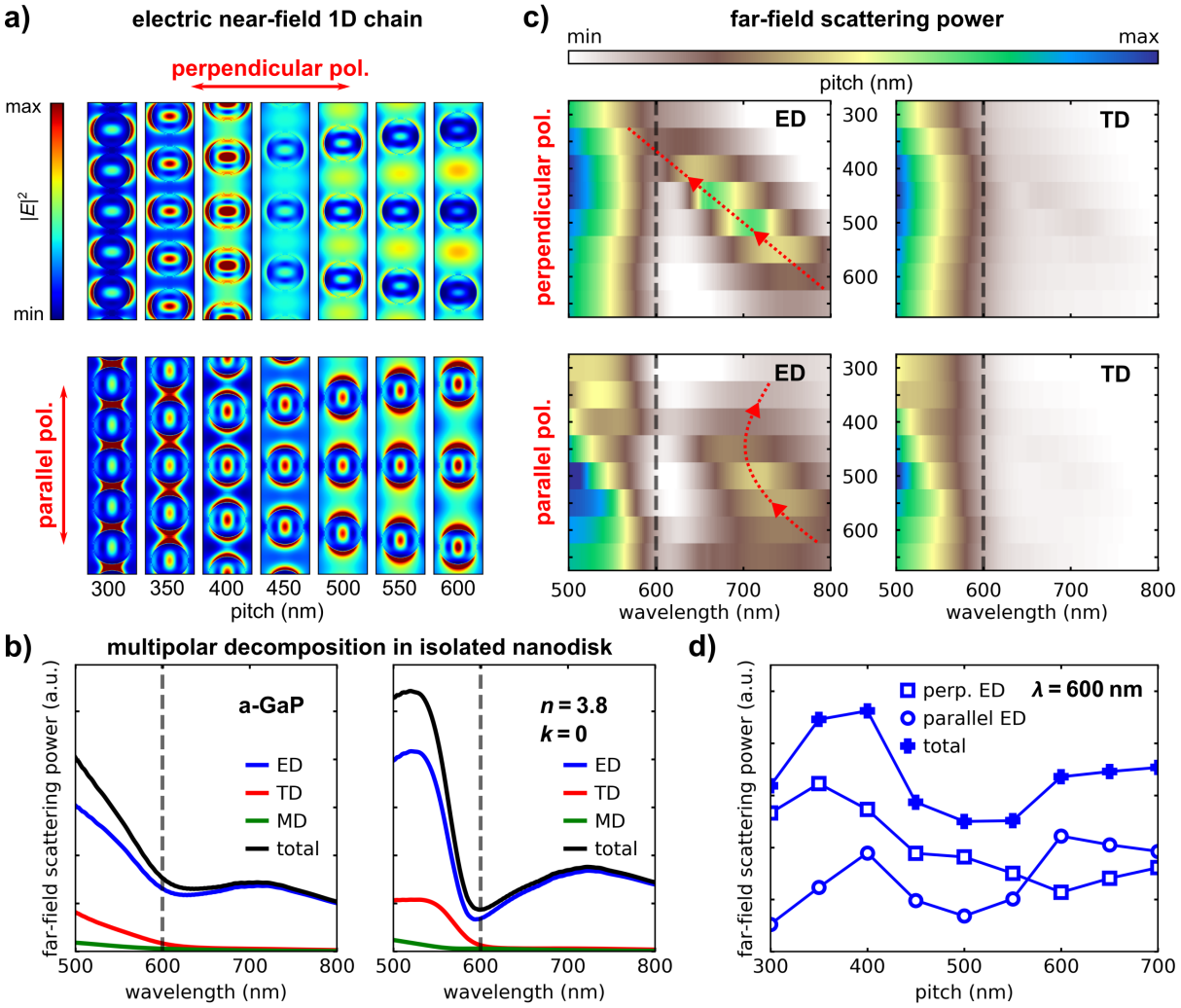

Figure 6.7: a) Electric near-field distribution of a 1D chain of nanodisks for different pitches p at $\lambda = 600\,\text{nm}$. In the top panel, the incident plane wave from the bottom is polarized perpendicular to the chain axis; in the bottom panel the wave is polarized along the chain axis. b) Multipolar decomposition of electric, toroidal, and magnetic dipoles (ED, TD, and MD, respectively) in an isolated nanodisks of (left) a-GaP and (right) an arbitrary, lossless material with nondispersive refractive index $n = 3.8$. The dashed lines indicate the spectral position of the anapole. c) Far-field scattering power of the ED (left) and TD (right) of a disk embedded in an infinite 1D chain at perpendicular and parallel polarized illumination in the top and bottom panel, respectively. d) Cross section along the dashed lines in c) for the electric dipoles.

Therefore, it is concluded that in this case the absorption enhancement is dominated by short-range coupling. Similar to perpendicular polarization, closest spacing does not result in highest absorption because the reduction of the pitch to values less than 400 nm causes a displacement of the fields into the gaps between the disks. This effect is in line with a previous study by Cambiasso et al.,[116] who created electromagnetic hotspots in the center of a GaP dimer for locally enhanced fluorescence. The cross sections through the

ED panels at λ_{AE} (Fig. 6.7 d) give an explanation for the maximum extinction of a 2D array with $p_x = p_x = 400\,\text{nm}$ since the two coupling directions sum up to provide the highest field enhancement. Additionally, grating modes from diagonally located neighbors (Eq.6.2, $i, j \neq 0$) have to be taken into account. Importantly, the presence of the anapole mediates the confinement of the enhanced fields into the resonator and therefore the conversion of electric into absorbed energy. The data demonstrate that the highest absorption performance is achieved by engineering the enhanced lattice coupling strength while maintaining the proper anapole excitation. In particular, it is observed in Figure 6.7 a) and c) that close spacing of the nanodisks causes a breakdown of the anapole, which results in a blurring of the characteristic field pattern and a distorted balance between ED and TD for $p < 400\,\text{nm}$. In perpendicular polarization, the TD onset blue-shifts such that the enhanced ED dominates at λ_{AE}. In the case of parallel polarization, the anapole also tends to an ED but with strong coupling between neighbors and the internal fields pushed into the interparticle volume while the intensity of the internal ED fields as λ_{AE} decreases.

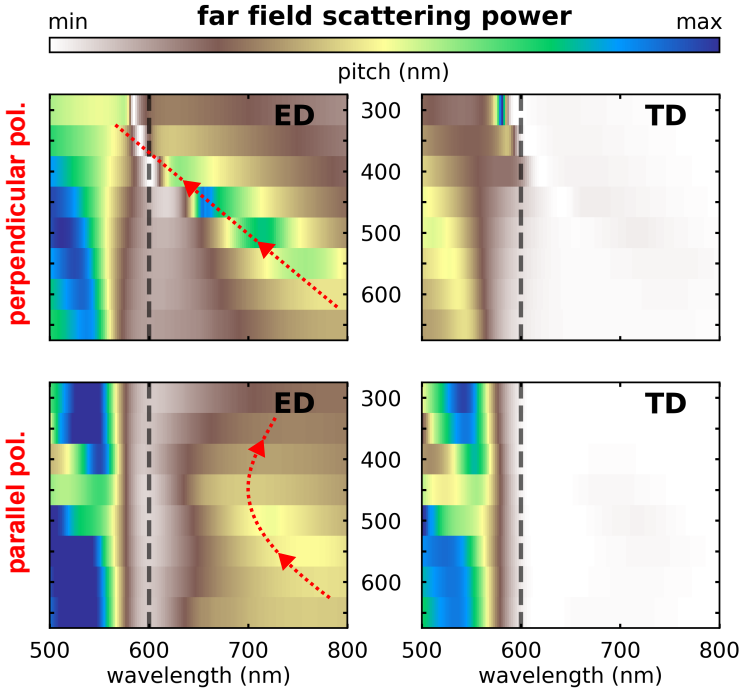

Figure 6.8: Multipolar decomposition of nanodisks of arbitrary lossless material in a 1D chain. The non-dispersive, complex refractive index is $n = 3.8$, $k = 0$.

These results provide a fundamental understanding of the ingredients for manipulating anapole-anapole interactions, which are (1) the particle distances parallel and perpendicular to the polarization axis for short-range and grating coupling, respectively, and (2) the combination of particle geometry with its refractive index for the spectral position of the anapole state. These entities can be experimentally tuned easily to achieve the desired effects throughout a large range of the electromagnetic spectrum. This idea can be transferred to NIR higher-harmonic generation in Ge [63, 97] and absorption enhancement of materials employed in solar energy conversion devices with otherwise weak absorption onsets in the visible spectrum, such as Si. This highly absorbing 2D layer can be important for flow cells in photocatalysis and/or photodetection, avoiding the penetration depth issues of 3D or colloidal solutions.

6.5 Experimental Details for Chapter 6

Transmission Spectroscopy The fabricated samples were illuminated by a nearly collimated broadband light source (OSL2, Thorlabs) from the bottom in a WiTec microscope in transmission configuration. For the 2D arrays the transmitted light was collected with a 10× objective (Olympus, NA = 0.25). For the 1D chains a 100× objective (Olympus, NA = 0.9) was used. The transmission spectra were normalized by the lamp spectrum taken from the glass background, resulting in transmittance spectra. The extinction is calculated by 1−transmittance.

FDTD Simulations To obtain $a(\lambda, x, y, z)$ and the electric near-fields simulations with *Lumerical* FDTD solutions were carried out. In the simulation-setup the substrate was assigned with a constant refractive index $n = 1.45$ and the a-GaP disks with the dispersive, complex refractive index of a-GaP sputtered at 350 °C. To simulate infinite 2D arrays, periodic boundary conditions were employed on the unit cell side walls, whereas for 1D chains only the y-boundaries are periodic and the x-boundaries are perfectly matched layers (PML) with an extent in the x-dimension of 800 nm. The absorbed power A was calculated by the power absorbed analysis tool, which forms a box that encloses the nanodisks. Simple transmission simulations of the 2D arrays were not carried out for all configurations of p because the small extents of the unit cell used for small pitches inhibited setting reasonable spans of a transmission monitor. A plane wave from the bottom was used as a light source spanning the entire FDTD region of the unit cell. In the 2D case, perfectly normal incidence caused unphysical discontinuities in the absorbed power spectra whenever the critical grating periodicity condition was fulfilled (Fig. 6.9 a, b). For better resembling the experimental setup and taking into account the slight divergence of the light source, the shown spectra are each an average of 42 spectra for which the angle of incidence was varied from 0° to 20° with respect to the normal for both, in the plane of polarization and perpendicular to it. For this, the broadband-fixed-angle-source technique (BFAST) was used.

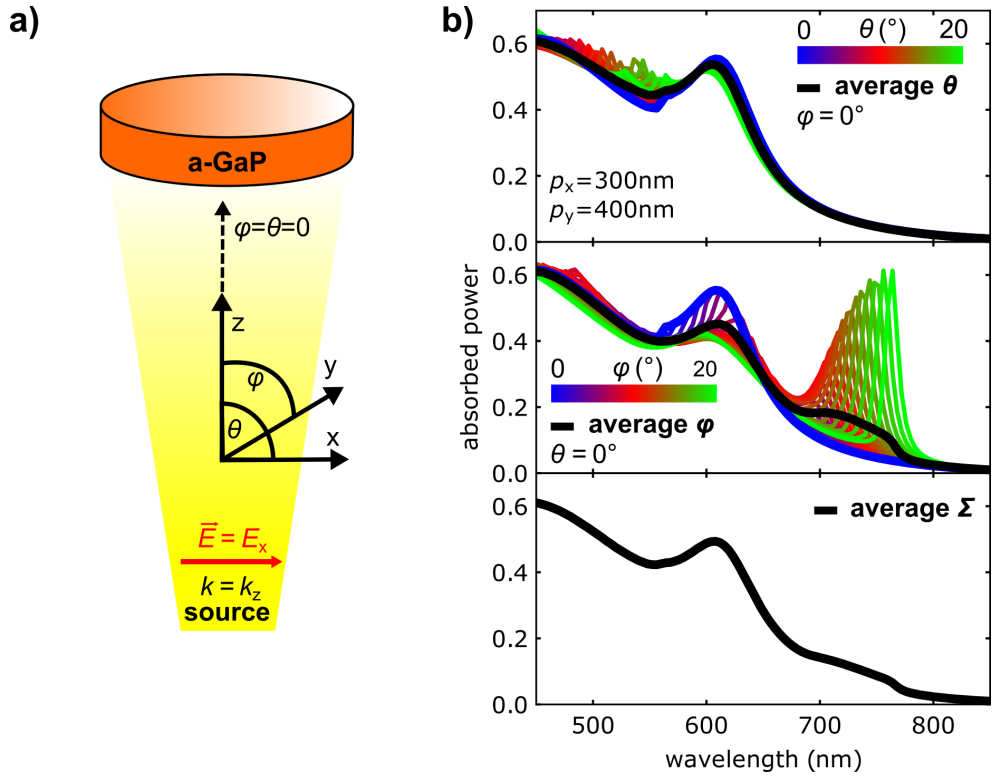

Figure 6.9: a) Sketch of the bottom illumination setup the a-GaP nanodisks. Due to the slight divergence of the source an ensemble of spectra with all combinations of θ and ϕ was simulated for each configuration of $p_{x/y}$ with θ and ϕ being the angles to normal incidence parallel and perpendicular to the plane of polarization, respectively, each ranging from 0° to 20°. b) Full ensemble of spectra using the example p_x = 400 nm and p_y = 300 nm. Perfectly normal incidence (blue lines) causes sharp discontinuities that were not observed in the measurements. The averaging accounts for the strong dependence of the lattice effect on the angle of incidence and allows for more realistic resembling of the experimental setup. The averaging procedure was not applied in the simulations of the 1D chains to facilitate the identification of the coupling effects.

Chapter 7

Metasurface Photoelectrodes

Published in:
L. Hüttenhofer, M. Golibrzuch, O. Bienek, F. J. Wendisch, M. Becherer, I. D. Sharp, S. A. Maier, and E. Cortés
"Metasurface Photoelectrodes for Enhanced Solar Fuel Generation",
Advanced Energy Materials 2021, 2102877, reference [126], open access paper

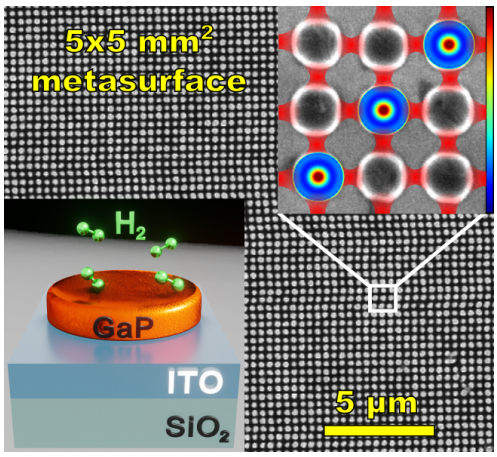

The previous chapter showcased for 2D arrays of dielectric resonators that the placement of the lattice resonance in the spectral vicinity of a single particle anapole excitation causes a strong enhancement of the internal electric fields and thus, of the power absorbed by the material. This strategy for spectrally tunable light trapping facilitates the increase of the optical absorption range in semiconductor photocatalysts, which are typically characterized by weak absorption onsets in the visible and NIR range. This chapter addresses the quantification of the energy conversion enhancement associated with these photonic effects under realistic catalytic conditions. This is made possible by the fabrication of photonically engineered, large-scale photoelectrodes that provide measurable photocatalytic yields. [39, 59, 127]

7.1 Tuning of Single Particle and Lattice Excitations

For identification of the AE in single particles, an ensemble of nanodisks with height $h = 100\,\text{nm}$ and increasing radius r was fabricated from an a-GaP film on SiO_2 by electron beam lithography (sec. 8.2), a SEM image of which is shown in Figure 7.1 a). The disks, which are separated by $2\,\mu\text{m}$ to avoid interparticle coupling, are optically characterized by

dark-field spectroscopy and corresponding FDTD simulations, as shown in Figure 7.1 b).

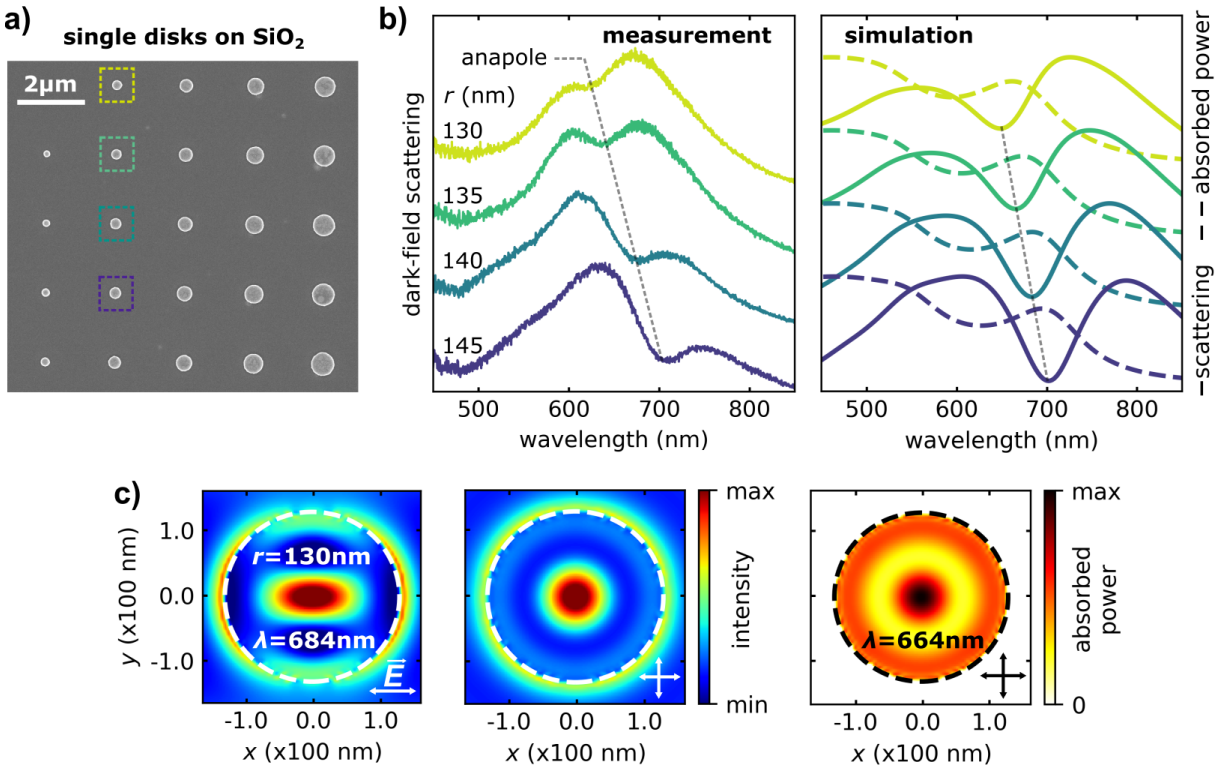

Figure 7.1: a) SEM image of single, uncoupled a-GaP nanodisks with increasing radius from top to bottom and left to right. b) Comparison between dark-field scattering of single disks, indicated by the dashed boxes in a), with FDTD simulations of scattering and absorbed power represented by solid and dashed lines, respectively. c) Near-field analysis of a nanodisk with radius r=130 nm. Typical electric near-field profile of the AE with x-polarized light (left) changes under light depolarization (middle) and converts to the absorbed power profile (right). Most light is absorbed in the center of the disk.

A detailed description of experimental conditions and simulation is provided in section 7.6. The AE-related scattering minimum redshifts as the disk radius is increased from 130 nm to 145 nm. The agreement of this trend with the simulations motivates further analysis of the internal fields of the resonator at λ_{AE}. Figure 7.1 c) (left panel) shows the characteristic intensity profile of the AE at $z = h/2$ under x-polarized illumination for a disk with height $h = 100\,\mathrm{nm}$ and radius $r = 130\,\mathrm{nm}$. By depolarizing the illumination $|E|^2_{\mathrm{depol}} = \frac{1}{2}(|E|^2_{x-\mathrm{pol}} + |E|^2_{y-\mathrm{pol}})$ to create an illumination condition resembling realistic device operating conditions, the light confinement into the resonator manifests in an even more obvious manner through the intensity maximum in the center (middle panel). Because the AE is driven in the lossy regime of the a-GaP ($\mathrm{Im}\{\tilde{n}(\lambda = \lambda_{\mathrm{AE}})\} > 0$) the intensity profile can be recalculated to quantify the absorbed power profile $a(\lambda_{\mathrm{AE}}, x, y, z = 50\,\mathrm{nm})$ using the equations given in chapter 6 with the boundary conditions of zero absorbed power outside of the disk and maximum absorbed power at the center of the disk. Integrating $a(\lambda, x, y, z)$ over the disk volume results in absorbed power spectra $A(\lambda)$, which are plotted

together with the simulated scattering in Figure 7.1 b). This presentation reveals that the scattering minimum at λ_{AE} is coincident with an absorption maximum due to coupling of the AE to the amorphous tail states in the a-GaP, effectively creating a strong edge over an extended spectral range.

The single particle analysis highlights that the AE assisted absorption enhancement within the spectral regime of weak losses of the employed material can be tuned by varying the disk radius r. On the road to upscaling and to guide the choice of the nanoimprint stamp design, a multitude of rectangular arrays of 20×20 a-GaP nanodisks with similar r to the single particles discussed above but with varying center-to-center distance p (pitch) were investigated. The nanodisk arrays were fabricated by electron beam lithography from a sputtered film stack of 100 nm thick a-GaP on 100 nm thick ITO on an a-SiO_2 substrate. Fabrication details are given in sections 8.2-8.4. A SEM image of an exemplary array is presented in Figure 7.2 a). The array sizes are sufficiently large to show clear signatures of collective interaction effects of the single particles, which are observed in the optical transmission measurements displayed in Figure 7.2 b). The upper panel shows the series of spectra from five individual arrays with different r, each having the same p = 350 nm. As explained above, the AE related transmission minimum (*i.e.* absorption maximum) redshifts with increasing r, but with lower total absorption at smaller r due to decreased areal coverage (*i.e.* filling factor) by a-GaP within the array. In addition, a radius-independent transmission minimum arises at 525 nm, which is assigned to the emergence of a lattice resonance (LR). The lower panel of Figure 7.2 b) shows transmission spectra of arrays with the same variation of r, but p = 400 nm. The LR redshifts to 600 nm, whereas the positions of the AE related transmission minima remain nearly unchanged.

Based on this analysis, the nanoimprint stamp is designed with the parameters r = 130 nm and p = 350 nm for the following reasons: First, this configuration separates the AE and the LR, which reduces their spectral overlap and facilitates independent measurement of the respective contribution of each to the photocatalytic enhancement. At the same time, a larger spectral range for solar light harvesting is covered. Second, larger values of p and/or smaller values of r reduce the filling factor of the metasurface, thereby reducing the overall absorption. Third, smaller values of p compromise the nanoimprint stamp fabrication due to proximity effects during electron beam exposure.

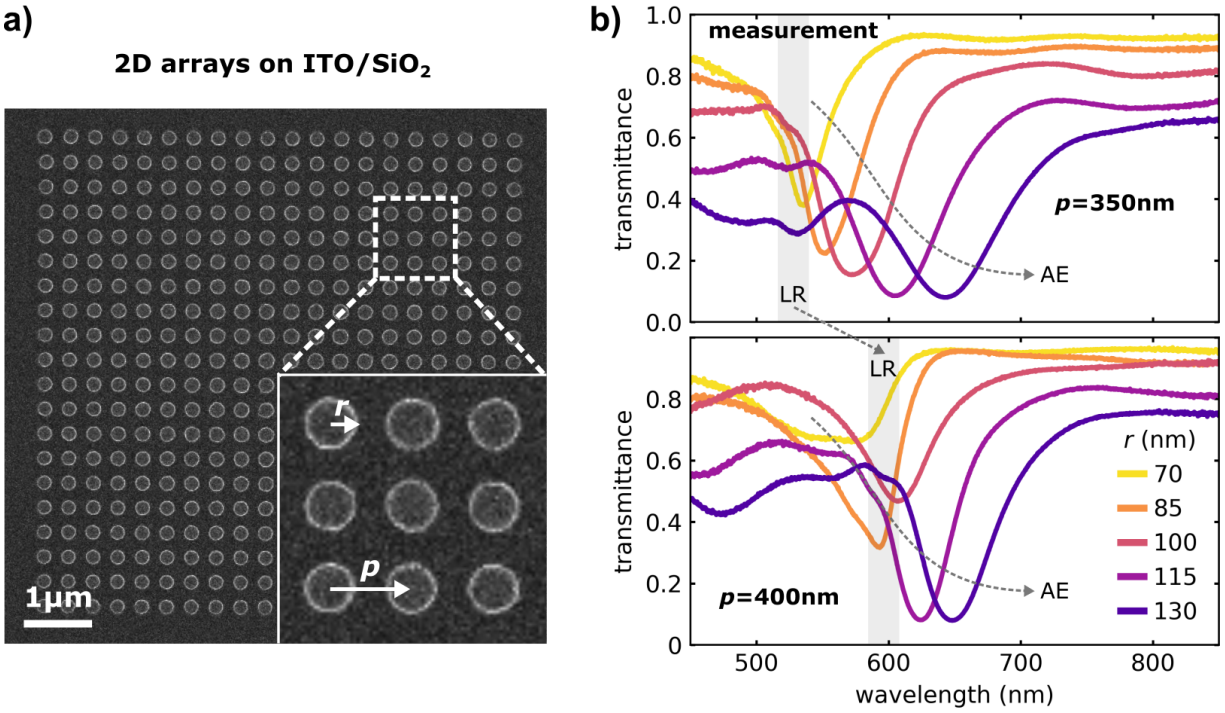

Figure 7.2: a) Rectangular array of nanodisks with r=130 nm and pitch p = 400 nm. b) Series of transmission spectra of arrays with p = 350 nm and 400 nm with several different values of r. The anapole excitation (AE) is tunable by r and the lattice resonance (LR) by p.

7.2 Nanoimprint Fabrication

After determination of the metasurface parameters on small-scale arrays, the nanoimprint stamp was fabricated using a Si wafer and electron beam lithography. Sections 8.5 and 8.6 provide additional details of the stamp fabrication and the imprint procedure. Although electron beam writing for a high resolution surface with a total area of 5×5 mm^2 is time consuming, high sample throughput and excellent reproducibility is achieved once the reusable stamp is produced. A scheme of the imprint procedure is shown in Figure 7.3 a). After spin-coating of the imprint resist, the inverted stamp is pressed onto the sample and leaves a polymer mask with height of approximately 180 nm. This relatively large thickness enables the use of the polymer itself as etching mask, which significantly reduces the temporal and resource expenditure for the metasurface fabrication. Finally, the residues of the polymer mask are removed in acetone and isopropanol. Figure 7.3 b)-d) displays a zoom-out series of images from small to large dimensions, beginning with a scheme of the unit cell of the metasurface illustrating the parameters that are critical for its optical properties, i.e. height, radius, and pitch. The SEM images (Fig. 7.3 c) demonstrate the high homogeneity of the nanostructure, with only minor fabrication defects. In particular, small variations of r among the disks are caused by irregularities of the stamp itself (sec. 8.5). The photograph in Figure 7.3 d) shows the as-fabricated metasurface photoelectrode next

to a continuous film of a-GaP. After dry etching, the ITO is exposed around the edges and is used as the back contact for both types of electrodes.

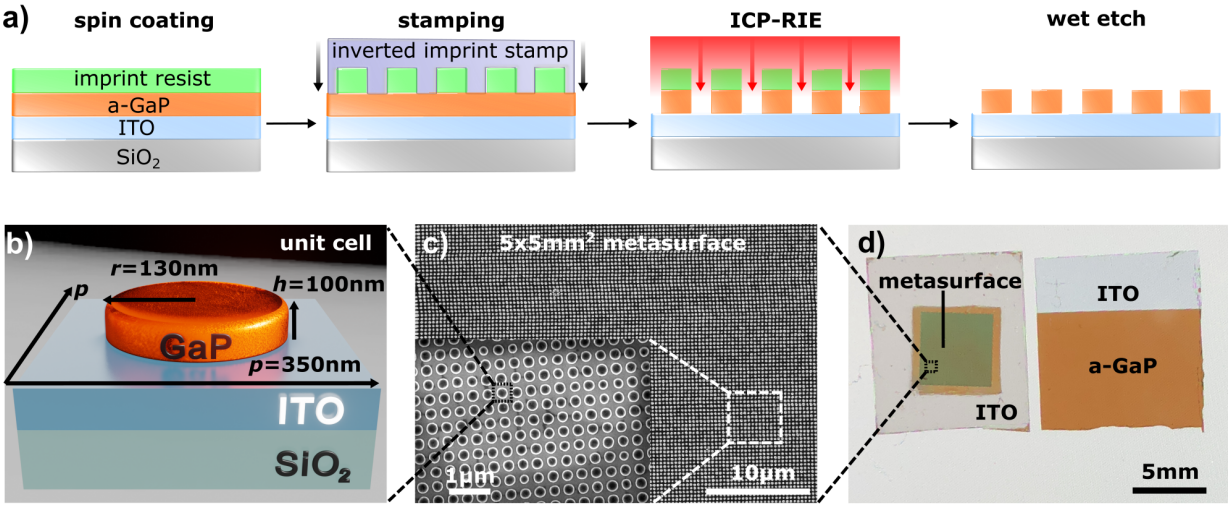

Figure 7.3: a) Fabrication procedure of a-GaP metasurface with nanoimprint lithography. The imprinted polymer structure is used as the etching mask. b) Scheme of the metasurface unit cell. c) SEM image with different zooms into the large-scale nanostructure. d) Photograph of the photoelectrodes with the imprinted metasurface on the left and a 100 nm thick continuous a-GaP film, both on top of a 100 nm thick layer of ITO.

The usage of nanoimprint was not only chosen because of high sample throughput, which was needed to examine physically and chemically fragile photoelectrodes, but also because this technique is also scalable for structuring of much larger surfaces, which is a requirement for commercial applications of this research. This is possible through large-area roll-to-roll and roll-to-plate lithography, which is continuously developed and improved with regard to process and stability control. [?] In addition, as the NIL process is based on direct mechanical deformation, its resolution is not constrained to the limitations of light diffraction or beam scattering factors as observed in conventional nanolithography methods. In terms of patterning capability, various 2D and 3D structures with feature sizes ranging from several micrometersdown to sub-50-nm scale have been demonstrated. [107]

7.3 Mode Analysis of the Metasurface

The metasurface was characterized by optical transmission and reflection spectroscopy (sec. 7.6). Figure 7.4 a) shows the transmission, reflection and absorption spectra of the metasurface on 100 nm thick ITO. The LR and AE signatures are pronounced at 550 nm and 640 nm, respectively, and provide an enhanced extinction across the terrestrial solar spectrum, which is indicated by the grey line. The LR is within the spectral range of 400-600 nm and the AE is covered by $\lambda > 600$ nm, depicted by the turquoise and red shaded areas, which will be used for the later PEC measurements. Particularly instructive for real device applications, the combination of the LR and AE enables a robust suppression of transmission with variation of the angle of incidence (Fig. 7.4 b). The LR redshifts with increasing angle of incidence. [64] However, α>45° is required to push the transmission minimum above 700 nm, which is a typical benchmark for minimum photon energy required for solar water splitting. [17] This good spectral robustness over 90° of total angle of incidence makes this metasurface design attractive for solar energy harvesting without the need of costly tracking systems. The results verify that the optimized 2D array was successfully upscaled with excellent reproduction of its optical properties.

For a thorough analysis of the internal fields of the nanodisks embedded in the metasurface, infinite array FDTD-simulations were performed (sec. 7.6). The calculated transmission, reflection and absorption spectra at normal incidence are presented in Figure 7.4 c). The results provide good agreement with the experimental data. The sharp transmission minimum at 520 nm is attributed to a simulation artifact, which was also previously encountered in infinite array simulations with a plane wave source at normal incidence and is not present in the measurements (see sec. 6.5). The transmission minima at 550 nm and 660 nm are assigned to the measured signatures of the LR and AE, respectively, and it is concluded that they are caused by maxima of absorption. Figure 7.4 d) shows the absorbed power profiles of a nanodisk embedded in the metasurface at the LR and AE wavelengths in top view ($z = h/2$) and side view ($y = 0$ nm) for depolarized excitation, which reveal distinct characters. Whereas at AE the absorption region is located in the lower, center part of the disk, the LR promotes absorption hotspots at the top face and the edges, which is beneficial for optical excitation of the near-surface volume of the a-GaP.

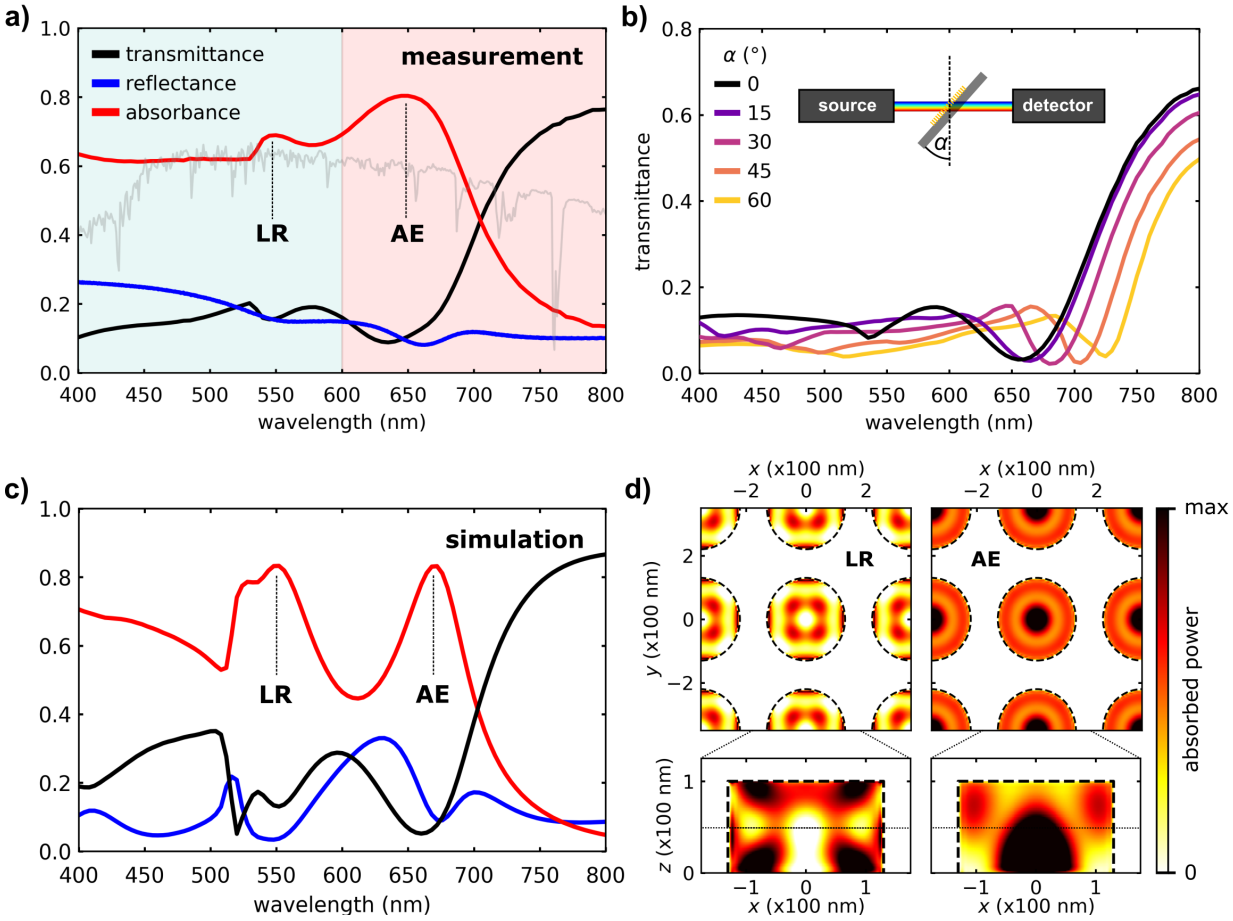

Figure 7.4: a) Measured transmission, reflection and absorption spectra of the metasurface. The turquoise and red shaded areas indicate the spectral regions for covering the LR and the AE. The grey curve represents the terrestrial solar spectrum. b) Transmission through the metasurface under variation of the angle α between normal incidence and sample rotation. c) Simulation of transmission, reflection and absorption by an infinite array at normal incidence. d) Color maps of the absorbed power profile in the nanodisks as horizontal and vertical cross-sections for the LR (left) and AE (right).

7.4 Photoelectrochemical Characterization

Having characterized the fundamental optical characteristics of a-GaP metasurfaces, photoelectrodes were prepared from the nanoimprinted samples and investigated their PEC performance in comparison to flat a-GaP films for the hydrogen evolution reaction (HER). As discussed above, a-GaP is very well suited for photonic engineering of the metasurface. In addition, although crystalline GaP is a well known photoelectrode material for solar water splitting and carbon dioxide reduction, [100, 128, 129, 130] a-GaP has not been investigated in detail. Prior to the characterization, the suitability of the a-GaP was thoroughly evaluated for the oxygen and hydrogen evolution reaction, OER and HER, respectively. Surface photovoltage measurements revealed that the a-GaP shows weak, but measurable upward band bending that is characteristic of unintentional n-type doping (see A.3). Therefore, the a-GaP should be more advantageous for the OER, since n-doping leads to internal electric fields that drive the drift of electrons (holes) away from (towards) the solid/liquid interface. However, measurements performed on flat films with alkaline electrolyte (1 M and 0.1 M KOH) under anodic bias lead to rapid dissolution of the a-GaP, whereas the a-GaP remained stable with acidic electrolyte (1 M $HClO_4$) under cycled cathodic bias for several hours (see A.4 and A.5). Hence, in order to clearly evaluate the contributions of the AE and LR for photocatalytic reactions under stable conditions, the HER was studied and the photocurrent enhancements relative to a bare a-GaP film grown under the same conditions were compared. Although the unintentional n-doping is not favorable for the HER, the approach can be further adapted to intentionally doped GaP films or other high refractive index semiconductors. Thus, the experiments provide valuable insights for the optimization of photocatalytic reactions by photonic engineering.

Figures 7.5 a) and b) show the three electrode photoelectrochemical setup comprising a reactor filled with the electrolyte (1 M $HClO_4$), a Ag/AgCl reference electrode (3 M KCl), and a Pt mesh counter electrode. The working electrode, *i.e.* either the a-GaP film or the metasurface, was contacted via the ITO, while the ITO exposed to the electrolyte was passivated with a non-conductive lacquer. The working electrode was illuminated by a Hg/Xe lamp with a 400 nm long pass filter to block out the UV spectral region, as well as exchangeable short and long pass filters (see A.7). The wavelength ranges cover either the AE (λ>600 nm, red) or the LR (400 nm<λ<600 nm, green) or both (λ>400 nm, orange). For PEC characterization, cyclic voltammetry with a sweep rate of 0.2 V/s was performed.

wavelength range (nm)	power density (mW/cm^2)
>400	1076
400 – 600	207
600 – 1000	780

Table 7.1: Lamp powers for PEC characterization

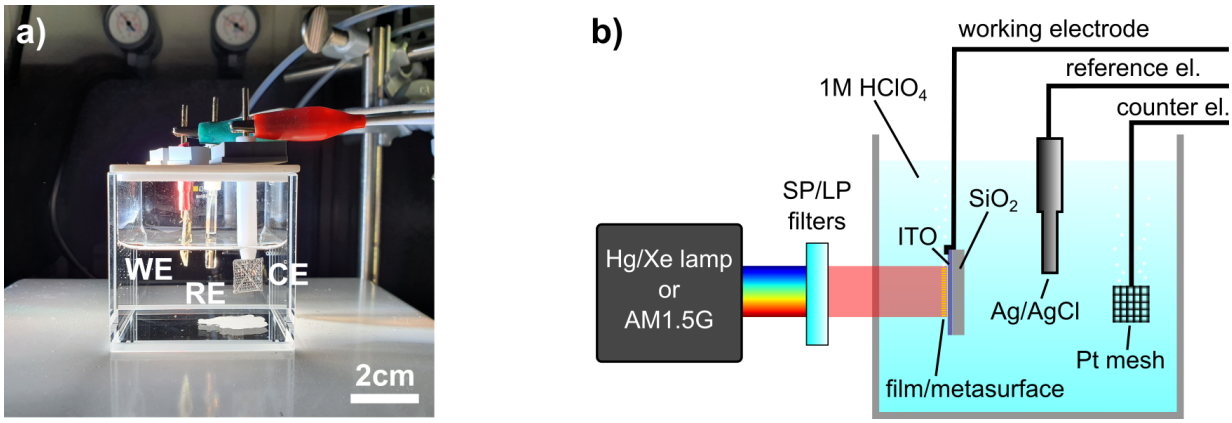

Figure 7.5: a) Photograph of reactor setup for the PEC characterization of the a-GaP film and metasurface with the working, reference and counter electrode (WE, RE and CE, respectively) immersed in the electrolyte. b) Schematic presentation comprising the short and long pass (SP, LP) filters.

The PEC characteristics of bare a-GaP films and metasurface are presented in Figure 7.6. The photoresponse is considerably weak and high illumination powers (see Tab. 7.1) are required to measure sizable photocurrents, which is an indication for extremely short charge carrier diffusion lengths and lifetimes at the catalyst-electrolyte interface.

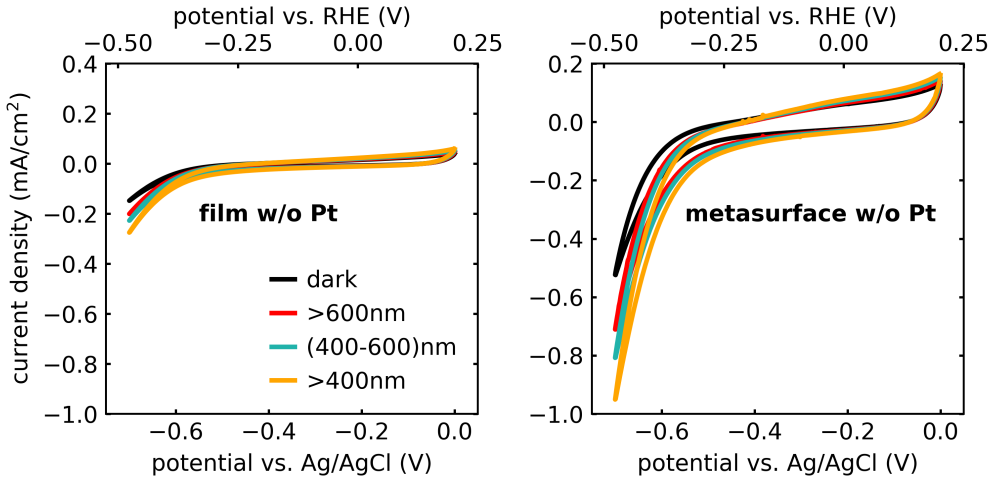

Figure 7.6: *I*-*V*-curves of the last out of ten cycles for the a-GaP film (left panel) and the metasurface (right panel) without the platinum co-catalyst.

To improve the photoresponse of the material, an additional 15 Å Pt layer was used as HER catalyst, which has minor effects on the optical properties (see A.6). The *I*-*V*-curves of the metasurface and the film in dark and under illumination at highest powers are displayed in Figure 7.7. The currents were normalized by the active areas exposed to the electrolyte, *i.e.* 25 mm^2 in the case of the metasurface. Compared to the film, the metasurface promotes a

clear enhancement of the photocurrent density under all illumination conditions. Potential contributions from the bare ITO between the nanodisks can be neglected due to small dark and photocurrents (see A.8).

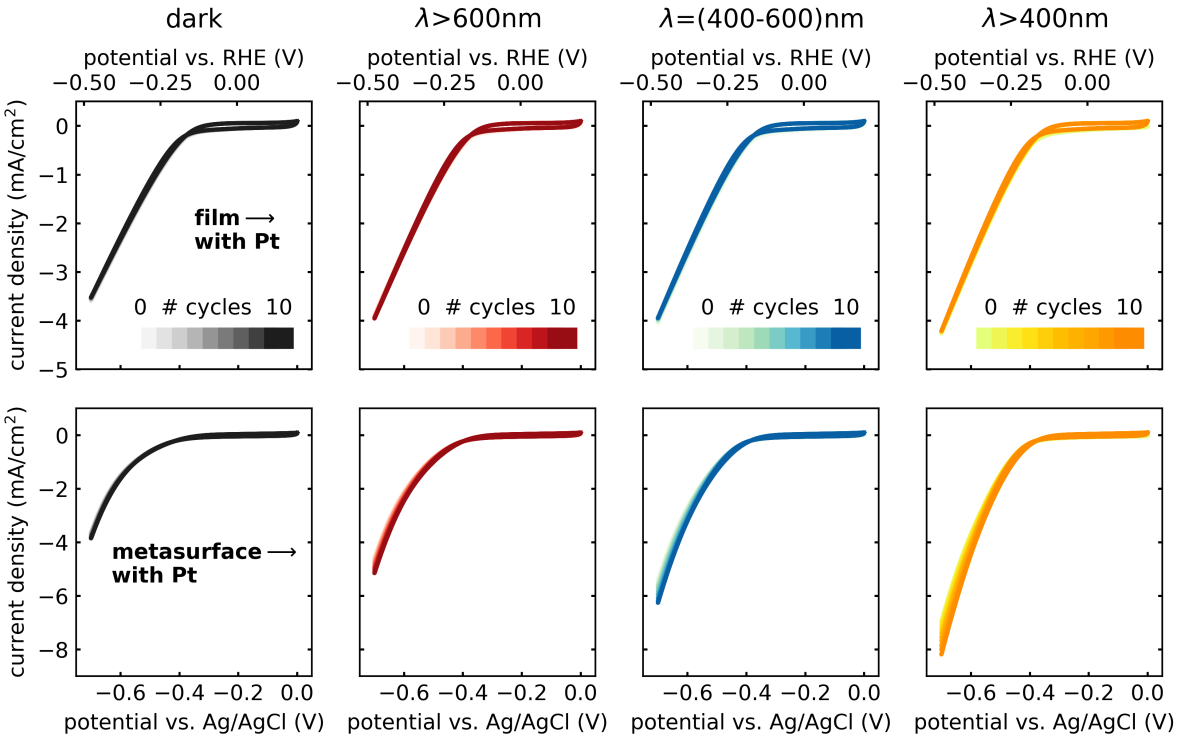

Figure 7.7: Cyclic voltammetry on the photoelectrodes with co-catalyst under dark conditions and red ($\lambda > 600\,\mathrm{nm}$), green ($400\,\mathrm{nm} < \lambda < 600\,\mathrm{nm}$) and white ($\lambda > 400\,\mathrm{nm}$) light illumination.

For better visualization of the metasurface-related photocurrent enhancement, the ratio $I_{\mathrm{light}}/I_{\mathrm{dark}}$ at $V = -0.7\,\mathrm{V}$ vs. Ag/AgCl (photo-enhancement factor, PEF) is plotted in Figure 7.8 a) for the film and the metasurface, illuminated by the three different spectral ranges. The presentation illustrates that the PEF is strongly enhanced by the metasurface for all three wavelength ranges. Power dependent PEC measurements were carried out by defocusing the Hg/Xe lamp and running cyclic voltammetry using the setup illustrated in Figure 7.5. The photo-enhancement factors at low, medium, and high lamp powers in Figures 7.8 b) and c) reveal a linear power dependence, which is less pronounced for the film at low powers. The slopes s of the linear fits to the power-dependent PEF are used to calculate the metasurface to film enhancement (MFE) factor by $\mathrm{MFE} = s_{\mathrm{meta.}}/s_{\mathrm{film}}$ for each wavelength range. Figure 7.8 d) shows the calculated MFE factors of 3.1, 5.3, and 5.7 for red, green and white light, respectively. These values demonstrate an unexpectedly strong contribution from the LR to the overall photocurrent enhancement, which is attributed to the near-surface absorption hot-spots and energetically higher electronic states populated by the LR-assisted absorption compared to the AE.

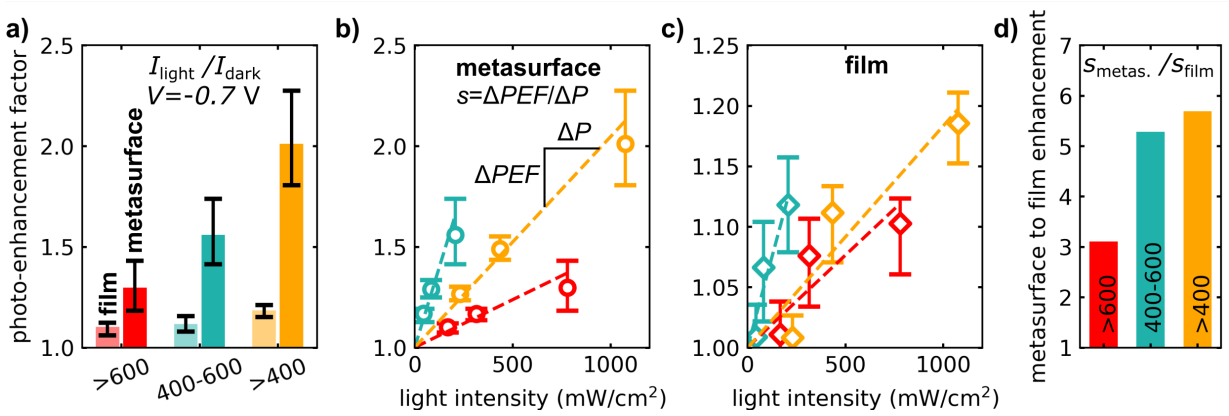

Figure 7.8: Photo-enhancement factor (photo- divided by dark currents) for the three different wavelength ranges in units of nm at $V = -0.7\,\mathrm{V}$ vs. Ag/AgCl. b), c) Linear power dependence of the photo-enhancement factor, with s representing the slope for each of the three investigated illumination conditions. d) Metasurface to film enhancement factors calculated from the data in b) and c) as the ratio between the slopes of power-dependent photo-enhancement factors from metasurfaces and continuous films.

The photoresponse of the photoelectrodes was also determined using a solar light simulator (AM 1.5G, $100\,\mathrm{mW/cm^2}$) to mimic the performance of the metasurface with solar illumination (Fig. 7.9 a-d). Chopped light chronoamperometry measurements at -0.7 V vs. Ag/AgCl shown in Figure 7.9 e) demonstrate a clear photocurrent and a strong enhancement by the metasurface in contrast to the a-GaP film, which exhibited a much weaker photoactivity. These results show that the judicious photonic engineering of anapole excitations and lattice resonances results in a substantial, relative efficiency enhancement through the superior absorption properties. Considering that the absorber volume of the metasurface is less than half of the film, the applied metrics for the calculation of the MFE values provide merely lower bounds of enhancement. Because the solar simulator only provides vertical illumination from the top, the experimental reactor setup was changed to flexible electrode holders and the photoelectrodes were connected to an isolated wire with silver conductive paste (Fig. 7.9 f). The contact was passivated with a non-conductive lacquer.

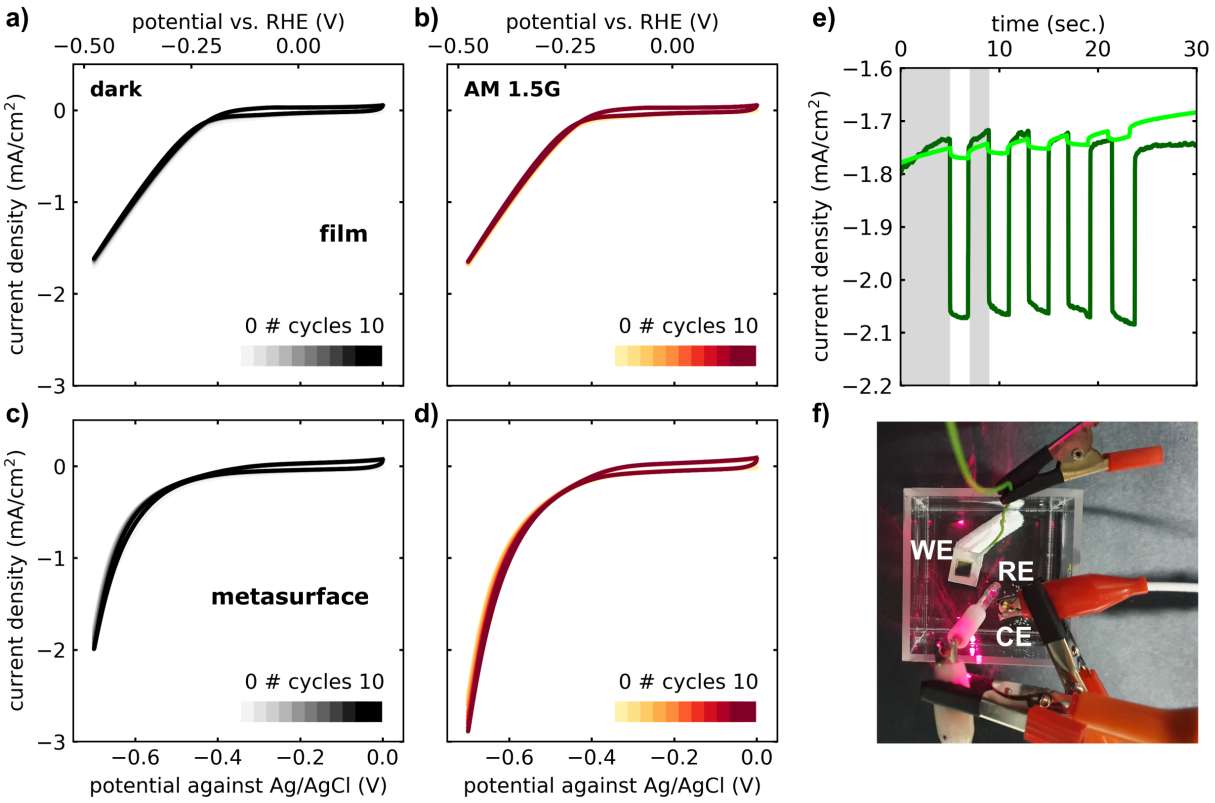

Figure 7.9: *I-V*-curves of with photoelectrodes with the planar a-GaP film (a, b) and the metasurface (c, d) in dark and under AM 1.5G illumination. The nanostructure provides a significant photoresponse by the material. e) Chopped-light chronoamperometry curves for an a-GaP metasurface compared to continuous a-GaP film at a potential of -0.7 V vs. Ag/AgCl under simulated AM 1.5G 1 Sun illumination. f) Top-view photograph of the reactor inserted in the solar light simulator.

7.5 Incident Photon-to-Current Conversion and Internal Quantum Efficiencies

A detailed spectrally-resolved analysis of the photocurrent enhancement was carried out in order to determine the incident photon-to-current conversion efficiency (IPCE) and the internal quantum efficiency (IQE) of the system. Figure 7.10 a) shows the measured absorbance spectra of the metasurface and the film with the Pt cocatalyst. The IPCE (Fig. 7.10 a) is defined as

$$IPCE(\lambda)[\%] = \frac{c \cdot h \cdot I_{\mathrm{ph}}}{\lambda \cdot P_{\mathrm{light}}} \times 100 \tag{7.1}$$

with with c, h, I_{ph} and P_{light} being the speed of light, the Planck constant in eVs, the photocurrent density and the irradiance of photons at the wavelength λ, respectively. [131] The values I_{ph} of were extracted from a set of chronoamperometry measurements under

chopped light with 10 nm bandwidth filters (see A.9). The results confirm the strong photocurrent enhancement for the metasurface across the visible range, consistent with the optical characterization of the photelectrodes (shown in the previous section). From these values, the IQE was calculated by

$$IQE(\lambda)[\%] = \frac{IPCE(\lambda)[\%]}{absorbance(\lambda)} \tag{7.2}$$

and is shown in Figure 7.10 c). The significant IQE enhancement by the metasurface is attributed to the near-surface absorption hot spots in the nanoresonators created by the engineered photonic states, as elaborated in Figure 7.4 d). It is assumed that these hot spots facilitate highly efficient and near-surface generation of electron-hole pairs, thereby reducing their recombination probability during migration on the - now shorter - path to the solid/liquid interface compared with the continuous film counterpart. A comparison of the IQE values reported here with previous studies investigating metallic nanoparticle systems [131, 132, 133] reveals similar to up to two orders of magnitude higher IQE from our electrodes.

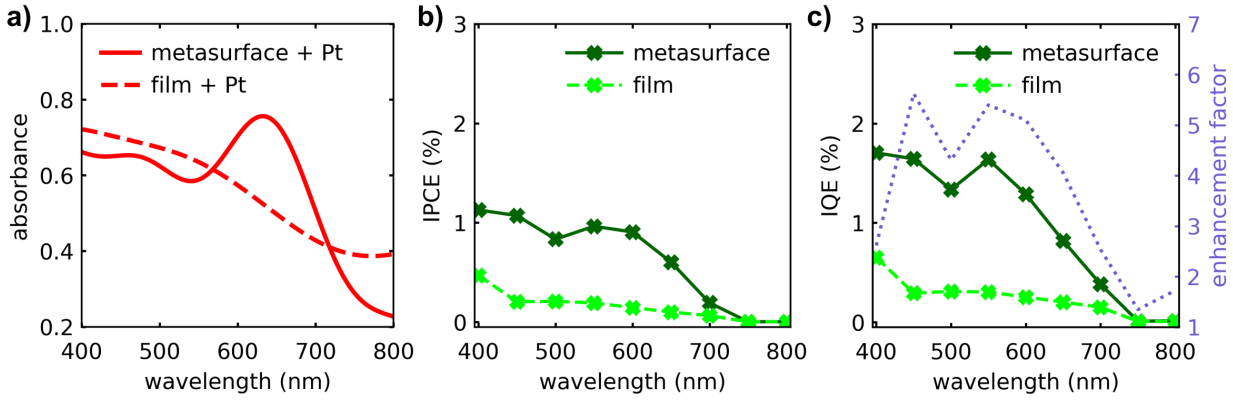

Figure 7.10: a) Absorbance spectra of the metasurface and film with the platinum cocatalyst. b) Incident photon-to-current conversion efficiency (IPCE) of the photoelectrodes. The metasurface provides a strong conversion enhancement at the maximum of the solar spectrum. c) Internal quantum efficiency (IQE) calculated from the values of a) and b).

7.6 Experimental Details of Chapter 7

Methods for Optical Characterization The dark-field spectra of the single nanodisks are measured witch a WiTec microscope in reflection using a dark-field objective (100×, NA = 0.9, Zeiss, Germany) and a halogen lamp. For transmission spectroscopy on the 2D arrays, the sample was illuminated by a nearly collimated halogen lamp (OSL2, Thorlabs) from the bottom, also using a WiTec microscope. The transmitted light was collected with a 10× objective (Olympus, NA = 0.25) and normalized by the lamp spectrum taken from the ITO/SiO_2 background. The reflectance spectra of the metasurface were measured with the same objective and a halogen lamp and the normalization spectrum were taken with an Ag mirror (Thorlabs PF20-03-P01). The angle dependent extinction spectra were taken with a spectral ellipsometer (VASE, LOT Quantum Design) in transmission mode with a collimated beam of diameter $\approx 1\,\mathrm{mm}$.

FDTD-Simulations The simulations were carried out with Lumerical FDTD-solutions. For the single particle analysis a disk with $r = 130\,\mathrm{nm}$ and $h = 100\,\mathrm{nm}$ was placed on a SiO_2 substrate ($n = 1.4$) using a mesh size of 5 nm. The scattering cross-section was calculated with the total-field-scattered-field analysis tool employing a plane wave source from the top. The particle absorption spectra were simulated with a power absorbed monitor that encloses the disk and also enables the display of the absorption profile. The electric near-fields, also used for the multipolar decomposition were obtained from a 3D frequency domain field profile monitor, also enclosing the disk. For the simulation of the metasurface a 100 nm layer of ITO (complex refractive index shown in 8.4) was added between the disk and the SiO_2 substrate together with periodic boundary conditions in x- and y-direction. The transmission (T) and reflection (R) was obtained from two frequency domain field and power monitors and the absorption (A) is calculated by $A = 1 - T - R$.

Chapter 8

Sample Fabrication Recipes

The following chapter provides a concise summary of the nanofabrication recipes used to prepare the measured samples.

8.1 Single TiO_{2-x} Nanodisks

TiO_2 was RF sputtered on SiO_2 coverslips at 5×10^{-7} Torr at a rate of 0.2 Å/s. Using a process similar to a previous study [134], oxygen vacancies were introduced into the as-deposited films with thickness of 200 nm by annealing in a resistively heated high vacuum furnace under a pressure of $\approx 1 \times 10^{-7}$ mbar. The temperature was ramped at a rate of 2 °C/s and then held at annealing temperatures ranging from 300 °C to 900 °C. The annealing times are 5 min for annealing temperatures above 600 °C and 15 min for annealing temperatures below. After completion of the annealing time, power was cut to the heater, causing a slow cooling lasting up to 1 h under vacuum conditions. To fabricate the oxygen-vacancy-rich TiO_{2-x} nanodisks, films with thickness of 160 nm and than patterned by deposition of an 80 nm Au mask using electron beam lithography, after which the films were etched in a RCP-RIE using SF_6/Ar-plasma. Consecutively, the Au mask was removed with potassium iodide Au etchant. Finally, the TiO_2 nanodisks were annealed as described above. The patterning was before annealing because the films suffered from formation of cracks upon annealing at temperatures > 400 °C (Fig. A.2). The fabrication process is illustrated in Figure 8.1 and summarized below.

1. spin-coat PMMA 950k A4.5: acceleration 1000 rpm/s, 3000 rpm for 60 s
2. prebake: 170 °C for 3 minutes
3. espacer: 2000 rpm, 60 s
4. electron beam exposure:
   acceleration voltage: 30 kV
   aperture: 10 µm
   working distance: 10 mm

dose: 400 µC/cm^2
stepsize: 10 nm

5. development in MIBK:IPA 3:1 for 60 s and IPA for 30 s
6. O_2 etch: 20 sccm, power 40 %, duration 15 s, pressure 1.3 mbar
7. mask deposition: 80 nm Au
8. lift-off in acetone for 1h at 55 °C and subsequent acetone rinse-off and IPA cleaning
9. TiO_2 ICP-RIE etching:
   process gases: SF_6 (10 sccm), Ar (7 sccm)
   chamber pressure: 20 mTorr
   RF power: 300 W
   ICP power: 31 W
   etch rate: 370 nm/min
10. Mask removal with potassium iodide Au etchant 3 min

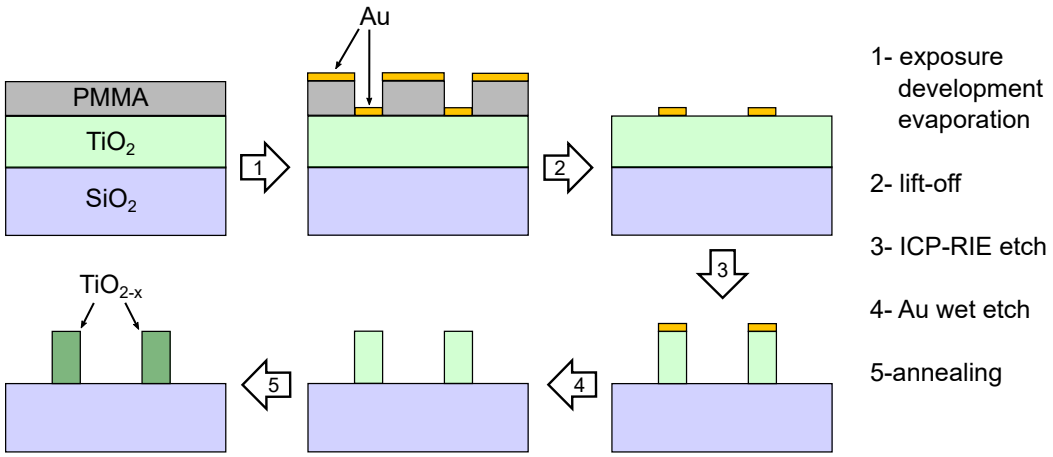

Figure 8.1: Scheme of TiO_{2-x} nanodisk fabrication using a positive resist.

8.2 Single a-GaP Nanodisks

Either 50 nm or 100 nm GaP was RF sputtered on SiO_2 coverslips at 5×10^{-7} Torr at a rate of 1 Å/s while the substrate holder was heated to various temperatures. Depending on the substrate temperature during deposition the optical properties of the material were modified, see spectral ellipsometry measurements in chapter 6. If not mentioned differently the substrate temperature during deposition was kept at 350 °C. After deposition, the GaP film was nano-structured employing the negative resist ma-N 2403 (Microchemicals), electron beam lithography and subsequent dry etching in a ICP-RIE using Cl/Ar-plasma. The fabrication process is illustrated in Figure 8.2 and summarized below.

1. spin-coat ma-N 2403: acceleration 1000 rpm/s, 3000 rpm for 30 s
2. prebake: 100 °C for 3 minutes
3. spin-coat espacer: 2000 rpm, 1 min
4. electron beam exposure:
   acceleration voltage: 20 kV
   aperture: 10 µm
   working distance: 10 mm
   dose: 120 µC/cm^2
   stepsize: 10 nm
5. development in microchemicals maD 525 for 40 s stopped by water rinsing
6. GaP ICP-RIE etching:
   process gases: Cl (10 sccm), Ar (30 sccm)
   chamber pressure: 2 mTorr
   RF power: 240 W
   ICP power: 30 W
   etch rate: 660 nm/min
7. resist removal in microchemicals REM700 for 2 minutes

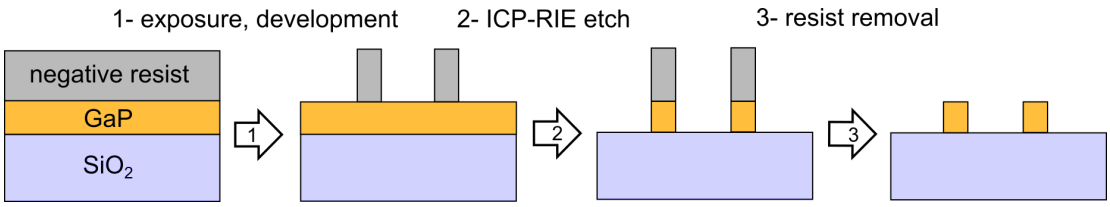

Figure 8.2: Scheme of GaP nanodisk fabrication employing a negative resist.

8.3 GaP Nanodisk Arrays

In principle, the fabrication of GaP arrays follows the same procedure as explained previously for single disks. However, very dense arrays tend to coalesce due to over-exposure during electron beam lithography, which is known as proximity effect (Fig. 8.3 a). The array shown in Figure 8.3 b) was fabricated with a reduced dose such coalescence was minimized albeit exhibiting a small disk radius reduction towards the array edges. Figure 8.3 c) illustrats how the exposure dose was adjusted according to the array periodicity in three steps for dense, intermediate and wide particle spacing.

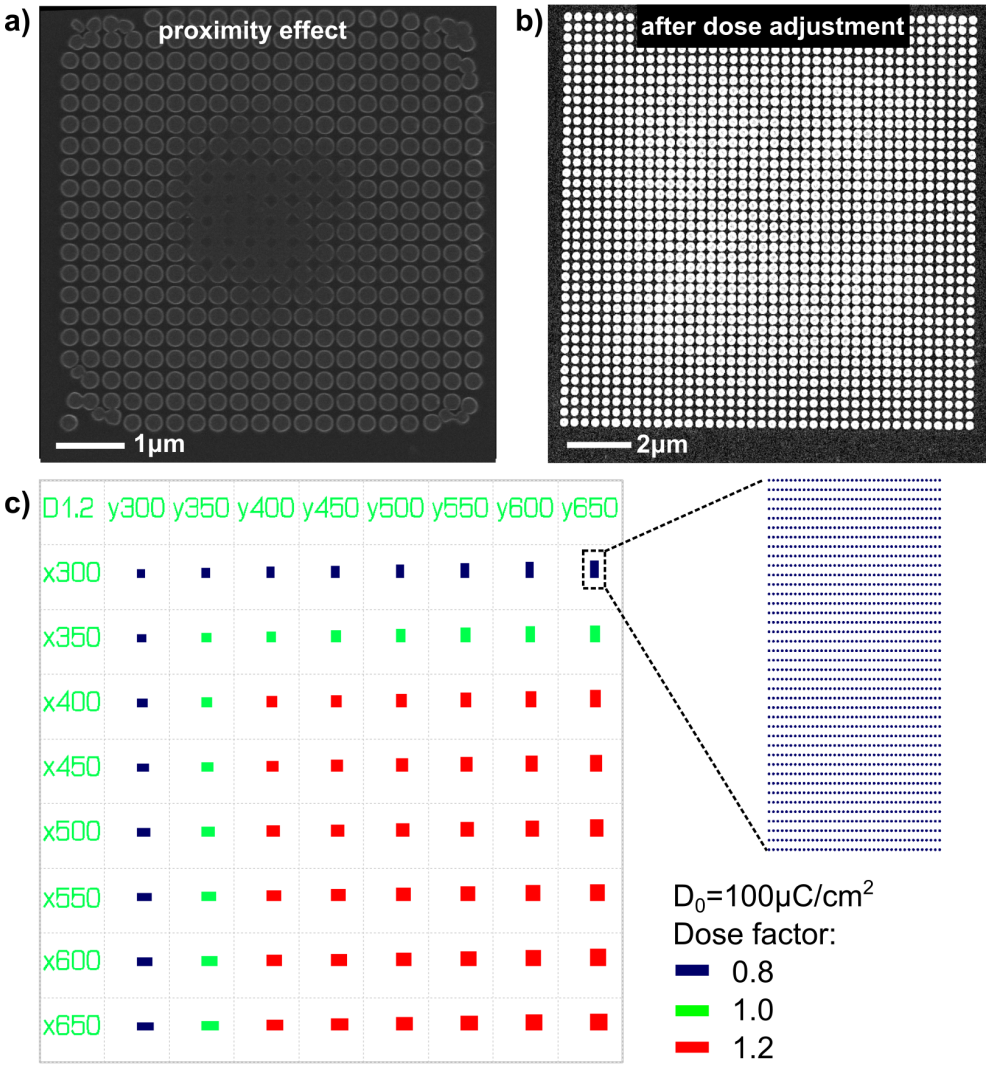

Figure 8.3: a) Array of closely spaced GaP nanodisks with coalescence in the center due to exposure overdose. b) Larger array with same disk parameters but adjusted exposure dose. c) Electron beam lithography design scheme of arrays with color coded exposure dose. For the smallest particle spacing (p_x, p_y = 300 nm) the dose needs to be reduced by 33% compared to single disk fabrication.

8.4 Characterization of ITO films

100 nm ITO was RF sputtered on SiO_2 cover glasses at 5×10^{-7} Torr at a rate of 0.5 Å/s while the substrate holder was heated to various temperatures. Depending on the substrate temperature during deposition the electrical and optical properties of the material were modified, see Figures 8.4 and 8.5. The substrate temperature during deposition was kept at 350 °C to achieve good conductivity and transparency of the material.

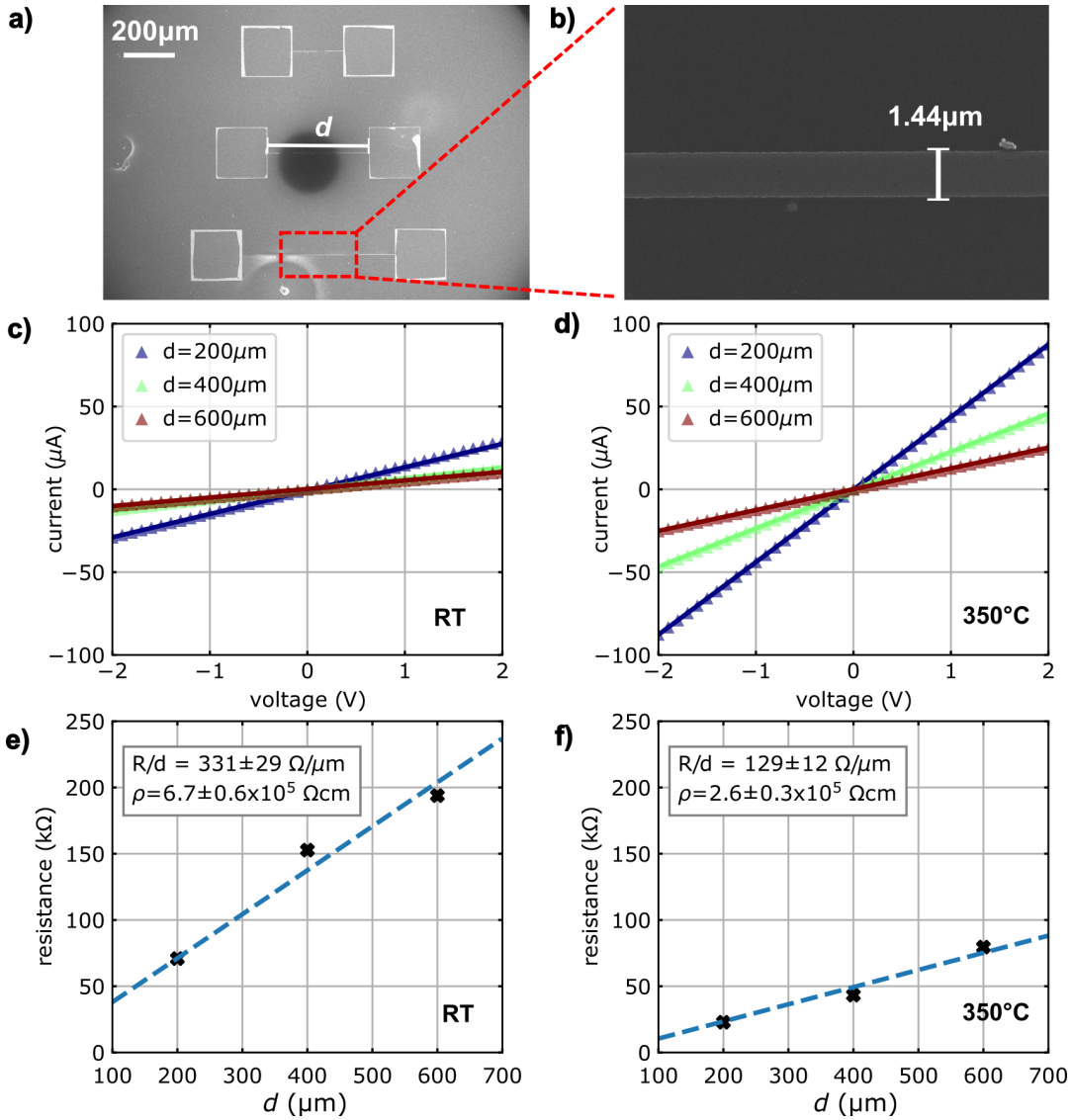

Figure 8.4: Electrical characterization of ITO films: a), b) SEM images of ITO two-point measurement contact pads connected through microwire of length d. c), d) I-V-curves for different d and deposition temperatures. e), f) Linear fit of resistances against d.

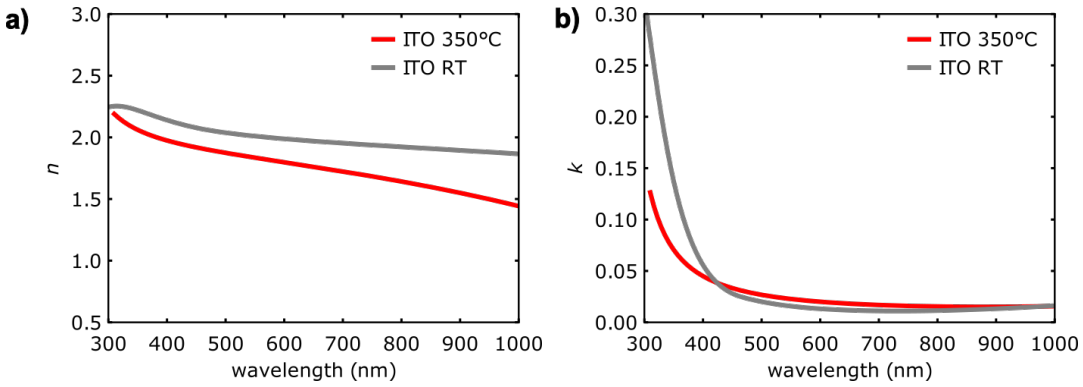

Figure 8.5: Optical characterization of ITO films depending on the deposition temperature: a) Real and b) imaginary refractive indices for different deposition temperatures measured by spectral ellipsometry.

8.5 Nanoimprint Stamp

The master stamp is fabricated from a piece of Si wafer with 200 nm layer of thermal SiO_2 (Fig. 8.6a). After spin-coating a 260 nm layer of PMMA 950k A4 the sample is exposed to electron beam lithography using an acceleration voltage of 20 kV and 30 µm aperture, that facilitated sufficient lateral resolution and a writing time of 50-60 h. The sample is then developed in MIBK:IPA (3:1) for 60 s and consecutively rinsed with IPA for 30 s. A 25 nm layer of Chromium is deposited on the sample by thermal evaporation and lifted off in acetone to generate a robust mask for the subsequent ICP-RIE etching with CHF_3/Ar plasma, achieving a SiO_2 pillar height (etching depth) of $d \approx 190$ nm. Ultimately, the residues of the Cr mask are removed in a 5 min Sigma Aldrich Cr etchant bath ($KMnO_4$ based) and the sample is cleaned with IPA and N_2 dry blowing. SEM images of the as-fabricates stamp are shown in Figures 8.6 b). The procedure is summarized as follows:

1. spin-coat PMMA 950k A4.5: acceleration 1000 rpm/s, 4000 rpm for 60 s, resulting thickness 260 nm
2. prebake: 170 °C for 3 minutes
3. espacer not required for nanoimprint stamp fabrication from n-Si wafer
4. electron beam exposure:
   acceleration voltage: 20 kV
   aperture: 30 µm
   working distance: 10 mm
   dose: 180 µC/cm^2
   stepsize: 20 nm
5. development in MIBK:IPA 3:1 for 60 s and IPA for 30 s
6. O_2 etch: 20 sccm, power 40 %, duration 15 s, pressure 1.3 mbar
7. Cr deposition, 25 nm evaporation

8. lift-off in acetone for 1h at 55 °C
9. SiO_2 ICP-RIE etching:
   process gases: CHF_3 (20 sccm), Ar (30 sccm)
   chamber pressure: 20 mTorr
   RF power: 30 W
   ICP power: 0 W
   etch rate: 6 nm/min
10. wet etch in $KMnO_4$ based Cr etchant and subsequent IPA cleaning

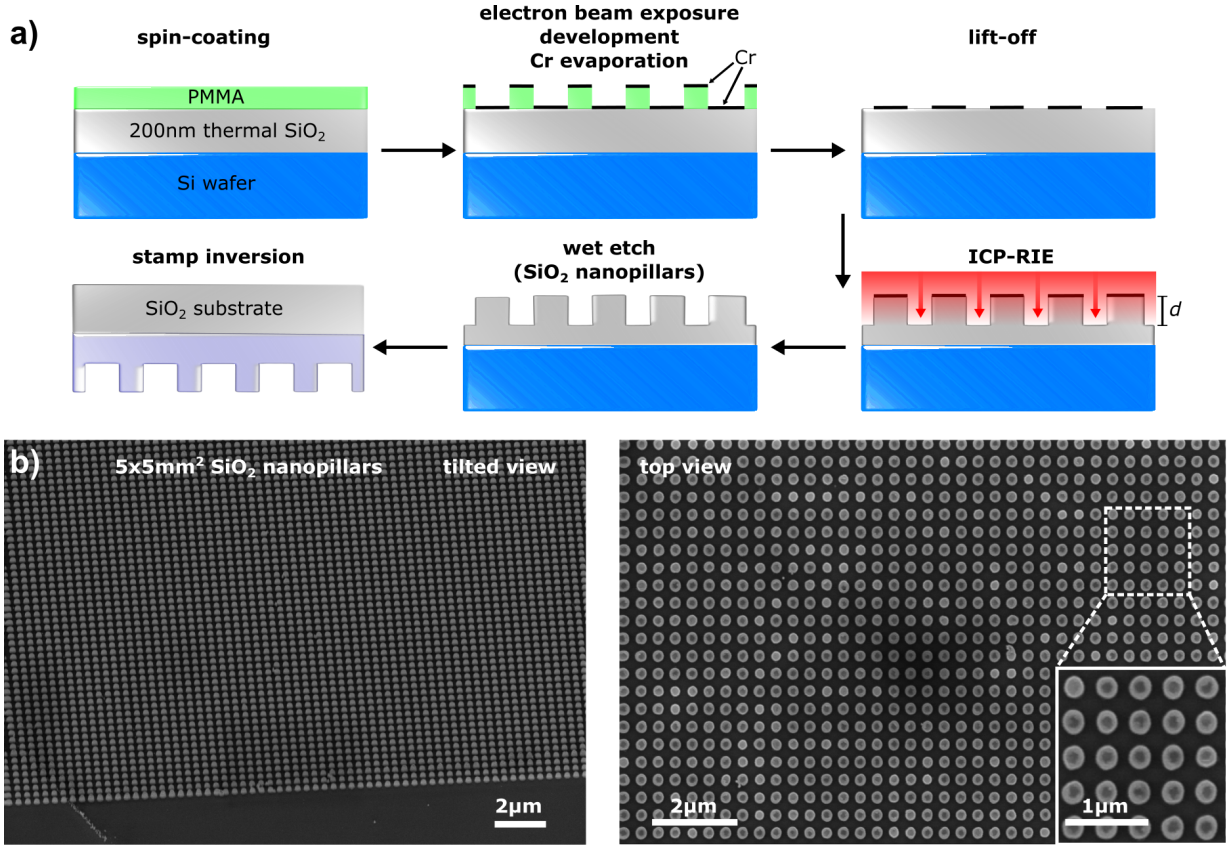

Figure 8.6: a) Scheme of nanoimprint stamp fabrication procedure. The SiO_2 pillar height (etching depth) is denoted as d. b) SEM images of the as-fabricated master stamp (SiO_2 nanopillars) in tilted and top view.

8.6 GaP Nanodisk-Metasurface

A 100 nm thick ITO film was sputtered on a SiO_2 cover glass followed by the sputtering of 100 nm a-GaP, both at 350 °C. The imprinting procedure was carried out by Matthias Golibrzuch from TU München during the collaboration of the project "Metasurface Photoeletrodes for Enhanced Solar Fuel Generation". [126] The goal of the imprint process is to generate a resist pattern that is used as a mask for a subsequent dry etching process to pattern the a-GaP layer. As the dry etching process will transfer the pattern of the resist into the a-GaP, the fabrication of resist pillars on top of the a-GaP film is required. However, an imprinting process with the as-fabricated master stamp would generate a hole pattern in the resist instead of pillars. Therefore, the structure of the stamp was inverted before the imprinting process (Fig. 8.6 b) "stamp inversion"). The replication process was conducted using OrmoPrime®, a commercial UV-curable hybrid polymer (Micro resist technology GmbH, Berlin). With the replication process semiflexible pattern-inverted working stamps were produced for the imprinting process. [135]

For the imprinting process a thin layer of mr-I8020 (Micro resist technology GmbH, Berlin) imprint resist is applied onto the substrates via spin coating. To achieve the best results for the desired geometry the imprint resist layer has a thickness of 55 nm. During the imprinting process, the substrate with applied working stamp is first heated to 165 °C. This temperature is above the resist's glass transition temperature of 115 °C, which allows the resist to become viscous. Now, the stamp is pressed into the resist at a pressure of 30 bar for 3 min. Afterwards, still under pressure, the sample is cooled to 90 °C to solidify the resist again. After the pressure is released, the stamp is carefully removed from the sample. The pattern with resist pillar height of 90 nm is now transferred from the stamp into the imprinting resist and the sample is ready for dry etching.

The imprint resist residuals around the pillars were carefully removed with acetone soaked cotton swabs to uncover the underlying ITO around the metasurface during etching for electrically contacting the electrodes. Than the samples were etched for 9 s with recipe described in 8.2. Ultimately, the resist pillar residues were removed in acetone and subsequent IPA rinse and N_2 dry blow.

For employing the cocatalyst layer on the top face of the nanodisks, 15 Å platinum was sputtered on the a-GaP film prior to the imprinting procedure.

Chapter 9

Conclusion & Outlook

This work demonstrates a strategy for the design of a nanodisk metasurface that drastically increases the photocurrent of moderately photoactive materials with a thickness of only 100 nm over nearly the full visible spectrum. Specifically, the key parameters for spectral tuning of the anapole excitation as well as the lattice resonance were elaborated, and the parameter window for optimal solar light harvesting were discussed in the course of scaling up from single nanoresonators to coupled arrays and metasurfaces. A procedure was proposed to fabricate the photonically engineered metasurfaces at large-scale and with high-throughput for use as photoelectrodes in solar fuel applications. The optical and numerical analysis of single particles, arrays and the metasurface photoelectrode connects the nanophotonic effects to the enhanced photocurrent generation. In particular, the respective contributions of the anapole excitation and the lattice resonance were assigned quantitatively to the overall enhancement by calculating wavelength dependent enhancement factors, which demonstrate an overall photocurrent enhancement factor of 5.7, compared to a continuous planar film, despite the latter possessing a significantly larger absorber volume. Importantly, this concept is not restricted by the use of TiO_{2-x} or a-GaP but is readily applicable to further optimize solar light harvesting in intentionally doped, high-performing semiconductor photocatalysts with more positive onset potentials. [37, 103, 110] Furthermore, ITO is used for electrical contacting the metasurface photoelectrodes while also facilitating optical characterization by transmission spectroscopy. However, a low refractive index substrate is not required for the support of Mie-resonances in dielectrics. [116] This makes this study instructive for direct nanoimprinting of crystalline wafers consisting of established semiconductor photocatalysts without the need for material transfer. Large-area roll-to-roll or roll-to-plate nanoimprinting techniques enable continuous and high-throughput production of large-scale nanopatterned surfaces, thereby providing a viable path from nanophotonic device concept demonstrations to industrially relevant applications. [136] It is stressed that nanophotonic engineering of photoelectrodes can be easily combined with other material-optimization approaches, *i.e.*, improved charge transfer and protective coatings.

Overall, state-of-the-art research provides all crucial requirements for realization of photocatalytic water splitting in a full device, which are broadband solar light harvesting,

high material energy conversion efficiency, material stability and scalability. From this it is concluded, that considerations should be made on apparatus designs that simultaneously enable good solar light collection, efficient hydrogen/oxygen extraction and clean water supply to ultimately transfer photocatalytic water splitting from "lab to reality". Besides these more long-term aspects, three possible routes are proposed for the immediate continuation of this research:

Material Choice As elaborated throughout the scope of this work, there are only two requirements for semiconductor photocatalysts to be optimized by the demonstrated approach: A refractive index larger 2.5 and a spectral region of low (but non-zero) extinction coefficient in which the absorption is to be enhanced. a-GaP meets these requirements as model material but its moderate photoresponse is just enough to demonstrate the catalytic enhancement by photonic modes, but absolute energy conversion efficiency values still fall way below commercial requirements. Therefore, it is obvious to re-build metasurface photoelectrodes with materials, which exhibit a much better intrinsic capability for water splitting and have optical properties similar to a-GaP. This specifically points towards the use of crystalline GaP and InP with suitable doping and protective coatings. As an example, InP coated with a 10 nm layer TiO_2 and 2 nm of Pt exhibits an unassisted short circuit current of $\approx 24\,\mathrm{mA/cm^2}$ under HER and solar light. [37] Multiplying this value by the demonstrated enhancement of 5.7 would lead to current $0.14\,\mathrm{A/cm^2}$. This corresponds to an H_2 amount of $\approx 25\,\mathrm{mol\,h^{-1}\,m^2}$ assuming 100 % Faradaic and extraction efficiency and thus ≈ 50 grams of H_2 per square meter and hour. With this amount, a car with a H_2 consumption of 10 g/km could be fueled for 5 km!

Mode Exploration Besides the anapole excitation there are more photonic modes with a high capability of light confinement. In a very recent study, the excitation of *hybrid* anapoles was shown in Si nanocylinders, which have stronger electric energy densities inside the particles as the "conventional" anapole. [137] Of particular interest for photocatalysis is that these hybid anapoles are supported by nanocylinders which have a much smaller radius to height ratio than nanodisks. This particle geometry would drastically improve the performance of the metasurface photoelectrodes because it creates a much larger catalytically active surface per unit area. Also, methods of light confinement for higher harmonic generation [138] can inspire new approaches for nanophotonic engineering in semiconductor photocatalysts. From a different direction, one suggestion is to use FDTD simulations to run large geometrical parameter sweeps and/or using machine learning methods to explore new forms of excitation, that maximize the figure of merit defined as the electric energy density inside the particle.

Application to Photovoltaics As mentioned in the introduction, there is efficiency limitations that photocatalysis and photovoltaics have in common: Photovoltaic cells should absorb as much sunlight as possible, which would suggest to increase the thickness of the their p-n-junction. However, if the distance between depletion region and electrodes is too

large, migrating charge carriers recombine before reaching the electrodes. Therefore and equivalently to semiconductor photocatalysis, there is the need to absorb as much sunlight within an as thin as possible material system. c-Si is the material closest to the Shockley-Queisser limit maximum but exhibits an indirect bandgap. It is compatible with organic semiconductors to form a p-n-junction. [139] Organic semiconductors have a comparably low refractive index (*e.g.* PDOT:PSS $n \approx 1.5$). Therefore, the material combination of an organic semiconductor with Si nanodisks maintains a high refractive index contrast, thereby enabling the support anapole excitations in the Si, that can be tuned to the indirect bandgap. This could allow for the desired strong solar light absorption within a extremely thin material system. Simultaneously, this would also increase the area of the p-n-interface.

By having shown the power and constraints of the investigated methods for enhanced solar water splitting, the thesis is concluded in the hope of continuation of this work by the succeeding generation of researchers.

Appendix A

Supporting Information

Raw PDS Data of TiO_{2-x} films [47]

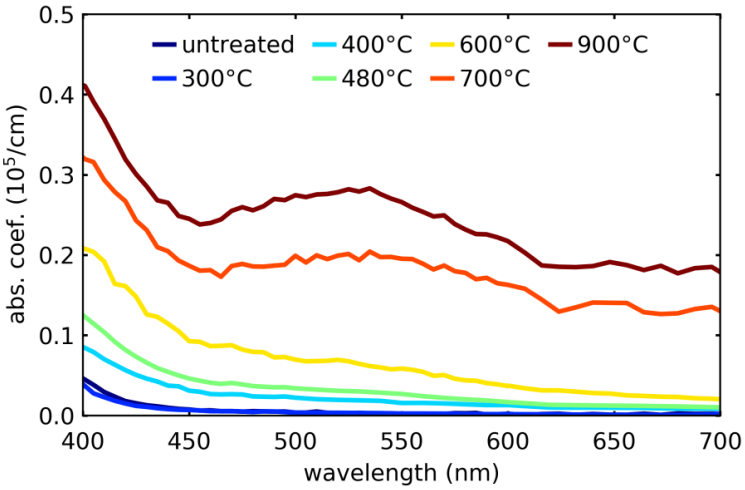

Figure A.1: Raw data of absorption coefficient measured by Photothermal Deflection Spectroscopy.

Crack formation of TiO_2 films upon annealing [47]

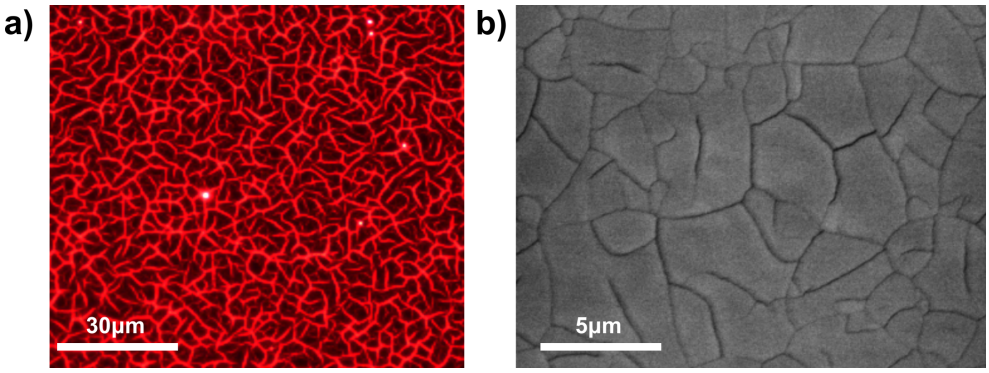

Figure A.2: During annealing the TiO_2 films suffer from crack formation for annealing temperatures $\approx$ 400 °C. (a) Dark-field image ($\lambda_{DF} \geq 650\,nm$) and (b) SEM image showing the crack formation.

Determination of the Doping-Type of a-GaP [126]

The measurement was carried out by Oliver Bienek from TU München. The doping type of the GaP layer was determined by measuring its surface photovoltage (SPV) in a GaP/ITO/glass stack with the underlying ITO serving as an electrical contact to the layer. The measurement was carried out in air using a KPTechnology KP020 Kelvin probe system is equipped with an Au electrode. A 455 nm LED was applied to illuminate the sample. In order to determine the SPV, the contact potential difference (CPD) was recorded in alternating periods of darkness and illumination. The SPV can be calculated by the negative difference of both values: $SPV = -\Delta CPD$ with $\Delta CPD = CPD_{light} - CPD_{dark}$. Figure A.3 displays the CPD measurement. The CPD signal shows a decrease upon illumination corresponding to a positive SPV, which is indicative of an upward surface band bending due to the population of surface states, typically present in n-type semiconductors. Since the photon energy is well below the band gap of ITO of around 4 eV, measuring effects from the buried interface can be excluded. [140] Furthermore, the relatively small SPV suggests a small excess carrier density in the material. This behavior is attributed to the unintentional inhibition of n-doping during sputtering of the material. Driving a bare GaP photoelectrode at anodic bias for the oxygen evolution reaction (OER), where n-doping is favorable, is reported to lead to rapid degradation due to the formation of gallium oxide and consequent blocking of charge carrier transfer to the electrolyte. [141] Thus, for the sake of sample stability the electrode is driven at cathodic bias and examined for the performance of the HER.

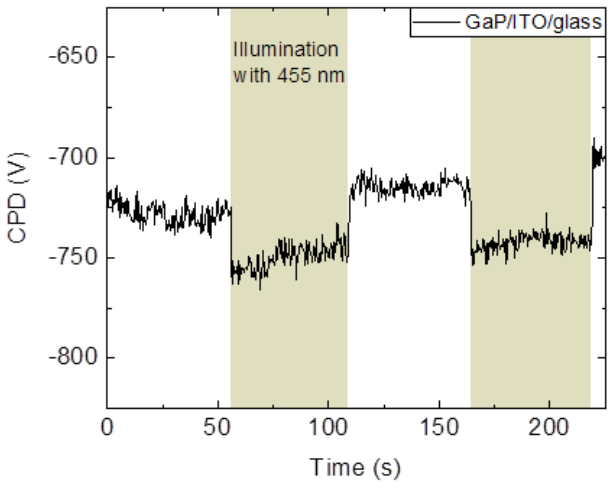

Figure A.3: Contact Potential Difference (CPD) on an a-GaP/ITO stack as a function of time under alternating illumination with 455 nm.

Stability of Bare a-GaP with Alkaline Electrolyte and Anodic Bias [126]

While a-GaP in 1 M KOH remained stable for 2 h without any visible changes, cyclic voltammetry under anodic bias lead to immediate dissolution even with 0.1 M KOH and small anodic potentials of 0.1 V (vs. Ag/AgCl).

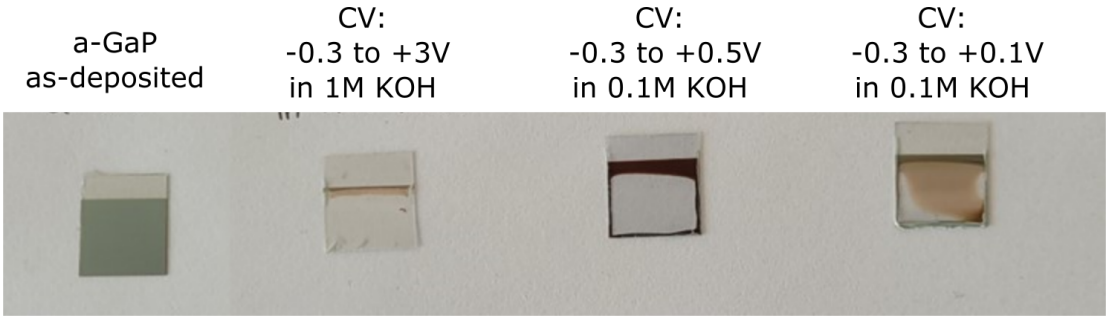

Figure A.4: Photographs of a-GaP substrates after cyclic voltammetry (CV) in alkaline electrolyte with anodic bias. The dissolution occurred immediately when applying anodic potentials. All potentials are vs. Ag/AgCl reference electrode.

Stability of Metasurface under Constant Cathodic Bias [126]

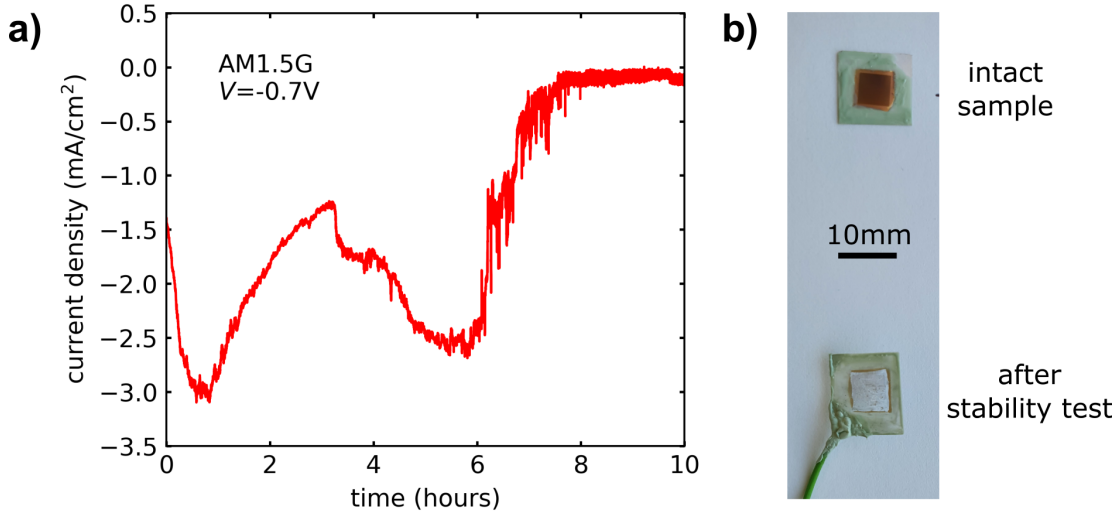

Figure A.5: a) Chronoamperometric (I-t)-curves of a metasurface a-GaP photoelectrode with 15 Å Pt under AM 1.5G illumination and constant applied potential of -0.7 V vs. Ag/AgCl. b) Photograph of (left) intact sample and (right) sample after the stability test. Contact probe measurements on the used electrode showed no conductance on the previously active area. In contrast to voltage cycling, constant cathodic bias leads to degradation of the electrode after 6-7 hours. Despite the observed degradation, future integration of a corrosion protection layer provides a route to long-term operational stability. [142]

Metasurface and Film Transmission with Platinum Coating [126]

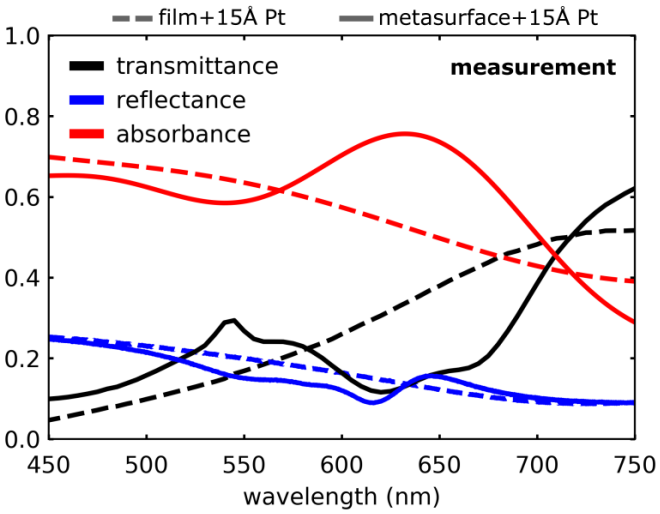

Figure A.6: Transmittance, Reflectance and calculated absorbance ($T + R + A = 1$) of a-GaP film (dashed lines) on ITO and of the metasurface (solid lines) with 15 Å platinum as co-catalyst. For the metasurface, the Pt is sputtered on the a-GaP film before dry etching to guarantee that it is not in contact with the ITO and the Pt is located only on the top face of the disks. The Pt coating leads to a broadening of the resonances but maintains the optical characteristics of the metasurface.

Transmission Curves of Optical Filters in PEC Setup [126]

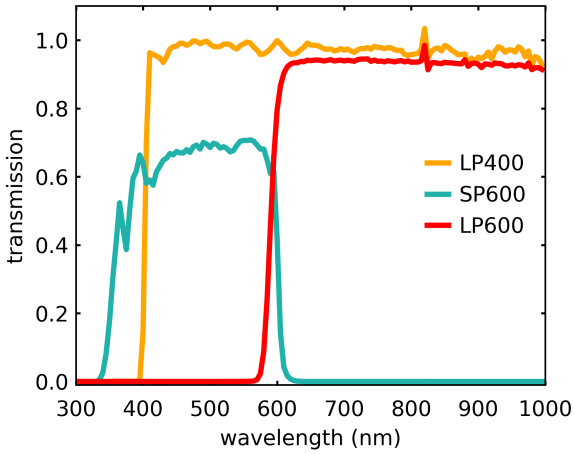

Figure A.7: Measured transmission of the default 400 nm long pass (LP400), 600 nm short pass (SP600) and 600 nm long pass (LP600) filters.

PEC characterization of ITO [126]

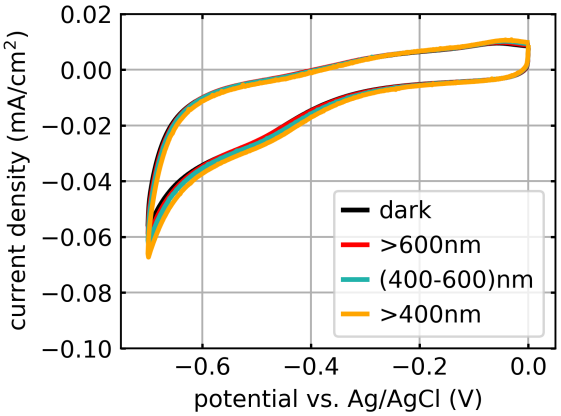

Figure A.8: Cyclic voltammetry of bare ITO in dark and highest illumination powers.

Narrow Band Width Chopped Light Chronoamperometry [126]

To determine the incident photonto-current conversion efficiency (IPCE) the current density of the electrodes with the Pt cocatalyst were measured under applied constant voltage of -0.7 V vs Ag/AgCl and chopped light from a 1000 W Xe/Hg lamp with various band pass filters with a bandwidth of 10 nm (Newport 20BPF10).

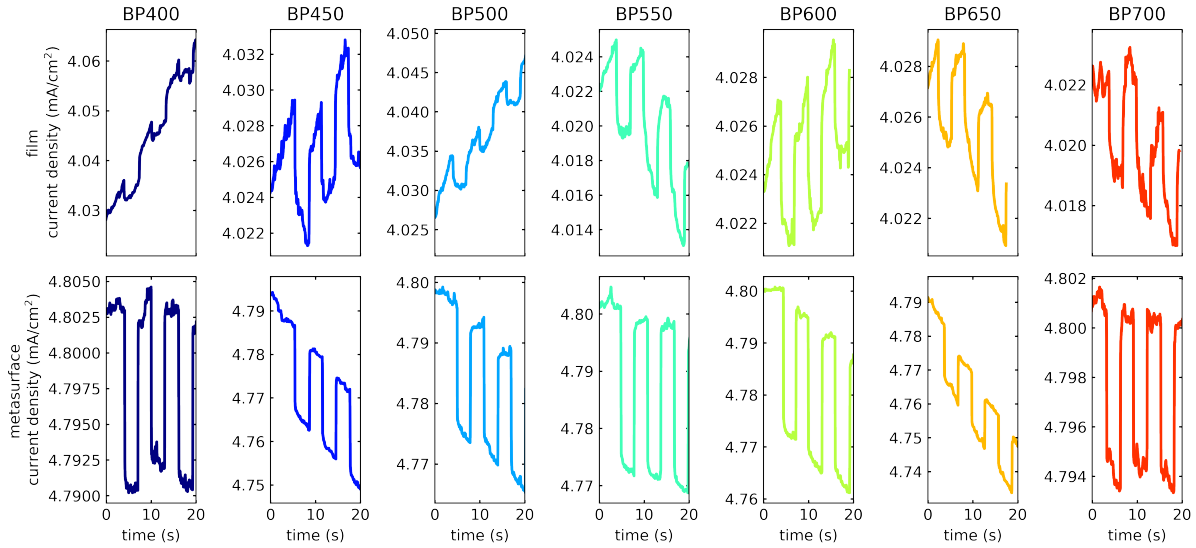

Figure A.9: a, b) Chronoamprometric curves of the photoelectrodes (top: film, bottom: metasurface) under chopped light illumination with 10 nm bandwidth band pass filters (BP).

Appendix B

Publisher Permissions

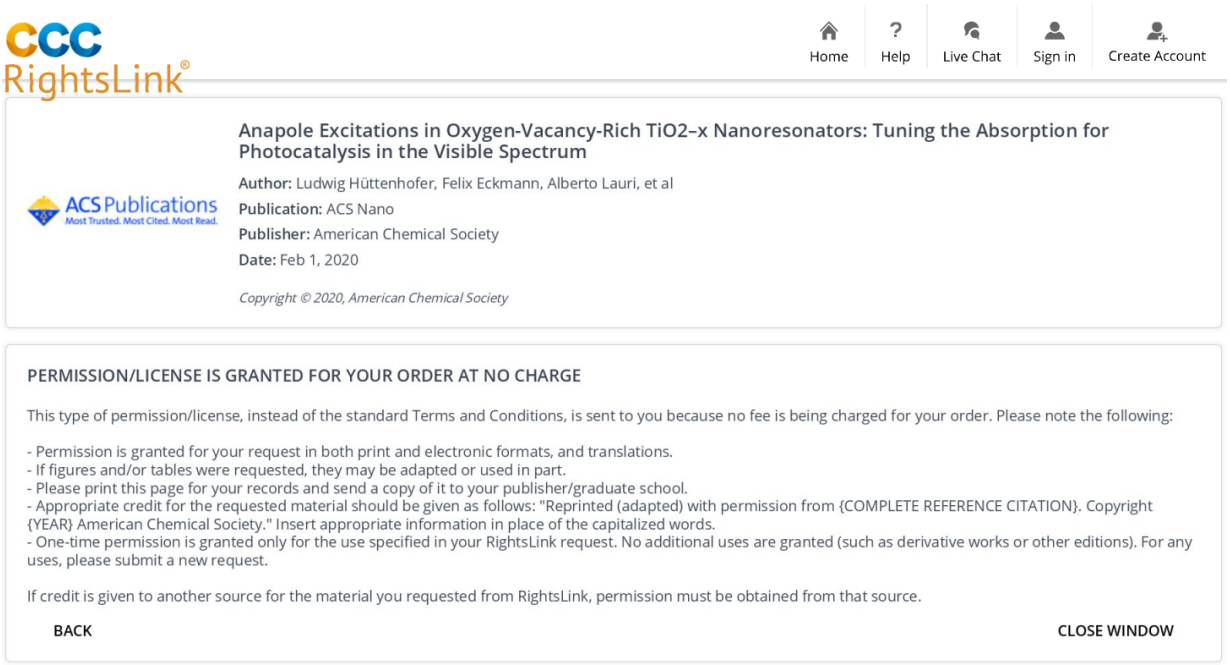

Bibliography

[1] V. Masson-Delmotte, P. Zhai, A. Pirani, S. Connors, C. Péan, S. Berger, N. Caud, Y. Chen, L. Goldfarb, M. Gomis, M. Huang, K. Leitzell, E. Lonnoy, J. Matthews, T. Maycock, T. Waterfield, O. Yelekçi, R. Yu, and B. Zhou. *IPCC, 2021: Climate Change 2021: The Physical Science Basis. Contribution of Working Group I to the Sixth Assessment Report of the Intergovernmental Panel on Climate Change*. Cambridge University Press, 2021.

[2] M. J. Burke and J. C. Stephens. Political power and renewable energy futures: A critical review. *Energy Research and Social Science*, 35, 78–93, 2018.

[3] J. A. Turner. A realizable renewable energy future. *Science*, 285, 5428, 687–689, 1999.

[4] Hydrogen Supply and Transportation using liquid Organic Hydrogen Carriers. www.cordis.europa.eu/project/id/779694/de.

[5] U.S. Department of Energy. www.energy.gov/eere/fuelcells/hydrogen-storage.

[6] K. Mazloomi and C. Gomes. Hydrogen as an energy carrier: Prospects and challenges. *Renewable and Sustainable Energy Reviews*, 16, 5, 3024–3033, 2012.

[7] Technology demonstration of large-scale photo-electrochemical system for solar hydrogen production. www.pecsys-horizon2020.eu.

[8] F. E. Osterloh. Boosting the efficiency of suspended photocatalysts for overall water splitting. *Journal of Physical Chemistry Letters*, 5, 15, 2510–2511, 2014.

[9] S. E. Braslavsky, A. M. Braun, A. E. Cassano, A. V. Emeline, M. I. Litter, L. Palmisano, V. N. Parmon, and N. Serpone. Glossary of terms used in photocatalysis and radiation catalysis (IUPAC recommendations 2011). *Pure and Applied Chemistry*, 83, 4, 931–1014, 2011.

[10] A. Fujishima and K. Honda. Electrochemical Photolysis of Water at a Semiconductor Electrode. *Nature*, 238, 37–38, 1972.

[11] A. J. Bard and M. A. Fox. Artificial Photosynthesis: Solar Splitting of Water to Hydrogen and Oxygen. *Accounts of Chemical Research*, 28, 3, 141–145, 1995.

[12] N. Serpone, A. V. Emeline, V. K. Ryabchuk, V. N. Kuznetsov, Y. M. Artem'Ev, and S. Horikoshi. Why do Hydrogen and Oxygen Yields from Semiconductor-Based Photocatalyzed Water Splitting Remain Disappointingly Low? Intrinsic and Extrinsic Factors Impacting Surface Redox Reactions. *ACS Energy Letters*, 1, 5, 931–948, 2016.

[13] M. G. Walter, E. L. Warren, J. R. McKone, S. W. Boettcher, Q. Mi, E. A. Santori, and N. S. Lewis. Solar water splitting cells. *Chemical Reviews*, 110, 11, 6446–6473, 2010.

[14] F. Opoku, K. K. Govender, C. G. C. E. van Sittert, and P. P. Govender. Recent Progress in the Development of Semiconductor-Based Photocatalyst Materials for Applications in Photocatalytic Water Splitting and Degradation of Pollutants. *Advanced Sustainable Systems*, 1, 7, 1700006, 2017.

[15] J. Li and N. Wu. Semiconductor-based photocatalysts and photoelectrochemical cells for solar fuel generation: a review. *Catalysis Science & Technology*, 5, 1360–1384, 2015.

[16] H. Kisch. *Semiconductor photocatalysis: Principles and applications*. Wiley-VCH Verlag, Weinheim, 2015.

[17] J. K. Stolarczyk, S. Bhattacharyya, L. Polavarapu, and J. Feldmann. Challenges and Prospects in Solar Water Splitting and CO_2 Reduction with Inorganic and Hybrid Nanostructures. *ACS Catalysis*, 8, 4, 3602–3635, 2018.

[18] J. Schneider, M. Matsuoka, M. Takeuchi, J. Zhang, Y. Horiuchi, M. Anpo, and D. W. Bahnemann. Understanding TiO_2 Photocatalysis: Mechanisms and Materials. *Chemical Reviews*, 114, 19, 9919–9986, 2014.

[19] W. Shockley and H. J. Queisser. Detailed Balance Limit of Efficiency of p-n Junction Solar Cells. *Journal of Applied Physics*, 32, 3, 510–519, 1961.

[20] X. Wang, Z. Li, J. Shi, and Y. Yu. One-Dimensional Titanium Dioxide Nanomaterials: Nanowires, Nanorods, and Nanobelts. *Chemical Reviews*, 114, 9385–9454, 2014.

[21] C. Xu, P. Ravi Anusuyadevi, C. Aymonier, R. Luque, and S. Marre. Nanostructured Materials for Photocatalysis. *Chemical Society Reviews*, 48, 14, 3868–3902, 2019.

[22] K. Maeda and K. Domen. New Non-Oxide Photocatalysts Designed for Overall Water Splitting under Visible Light. *Journal of Physical Chemistry C*, 111, 7851–7861, 2007.

[23] X. Yang and D. Wang. Photocatalysis: From Fundamental Principles to Materials and Applications. *ACS Applied Energy Materials*, 1, 12, 6657–6693, 2018.

[24] M. Anpo, Y. Ichihashi, M. Takeuchi, and H. Yamashita. Design of Unique Titanium Oxide Photocatalysts by an Advanced Metal Ion-Implantation Method and Photocatalytic Reactions Under Visible Light Irradiation. *Research on Chemical Intermediates*, 24, 2, 143–149, 1998.

[25] H. Kato and A. Kudo. Visible-Light-Response and Photocatalytic Activities of TiO_2 and $SrTiO_3$ Photocatalysts Codoped with Antimony and Chromium. *Journal of Physical Chemistry B*, 106, 19, 5029–5034, 2002.

[26] D. Dvoranová, V. Brezová, M. Mazúr, and M. A. Malati. Investigations of metal-doped titanium dioxide photocatalysts. *Applied Catalysis B: Environmental*, 37, 91–105, 2002.

[27] A. Standing, S. Assali, L. Gao, M. A. Verheijen, D. Van Dam, Y. Cui, P. H. Notten, J. E. Haverkort, and E. P. Bakkers. Efficient Water Reduction with Gallium Phosphide Nanowires. *Nature Communications*, 6, May, 1–7, 2015.

[28] S. A. Ansari, M. Khan, and O. Ansari. Nitrogen-doped titanium dioxide (N-doped TiO_2) for visible light photocatalysis. *New Journal of Chemistry*, 40, 3000–3009, 2016.

[29] J. Moma and J. Baloyi. Modified Titanium Dioxide for Photocatalytic Applications. In *Photocatalysts - Applications and Attributes*, pages 37–56, DOI: 10.5772/intechopen.79374. IntechOpen, 2019.

[30] L. Mascaretti, A. Dutta, V. M. Shalaev, and A. Boltasseva. Plasmon-Enhanced Photoelectrochemical Water Splitting for Efficient Renewable Energy Storage. *Advanced Materials*, 31, 1805513, 1805513, 2019.

[31] Q. Zhang, D. Q. Lima, I. Lee, F. Zaera, M. Chi, and Y. Yin. A Highly Active Titanium Dioxide Based Visible-Light Photocatalyst with Nonmetal Doping and Plasmonic Metal Decoration. *Angew. Chem. Int. Ed.*, 50, 7088–7092, 2011.

[32] K. Awazu, M. Fujimaki, C. Rockstuhl, and J. Tominaga. A Plasmonic Photocatalyst Consisting of Silver Nanoparticles Embedded in Titanium Dioxide. *Journal of American Chemical Society*, 130, 1676–1680, 2008.

[33] X. Shi, K. Ueno, N. Takabayashi, and H. Misawa. Plasmon-Enhanced Photocurrent Generation and Water Oxidation with a Gold Nanoisland-Loaded Titanium Dioxide Photoelectrode. *The Journal of Physical Chemistry C*, 117, 2494–2499, 2013.

[34] S. Hu, M. R. Shaner, J. A. Beardslee, M. Lichterman, B. S. Brunschwig, and N. S. Lewis. Amorphous TiO_2 coatings stabilize Si, GaAs, and GaP photoanodes for efficient water oxidation. *Science*, 344, 6187, 1005–1009, 2014.

[35] M. Malizia, B. Seger, I. Chorkendorff, and P. C. Vesborg. Formation of a p-n heterojunction on GaP photocathodes for H_2 production providing an open-circuit voltage of 710 mV. *Journal of Materials Chemistry A*, 2, 19, 6847–6853, 2014.

[36] V. N. Rao, S. Pitchaimuthu, P. Ravi, M. Sathish, H. Han, and S. M. Venkatakrishnan. Retorting Photocorrosion and Enhanced Charge Carrier Separation at CdSe Nanocapsules by Chemically Synthesized TiO_2 Shell for Photocatalytic Hydrogen Fuel Generation. *ChemCatChem*, 12, 11, 3139–3152, 2020.

[37] Y. Lin, R. Kapadia, J. Yang, M. Zheng, K. Chen, M. Hettick, X. Yin, C. Battaglia, I. D. Sharp, J. W. Ager, and A. Javey. Role of TiO_2 Surface Passivation on Improving the Performance of p-InP Photocathodes. *Journal of Physical Chemistry C*, 119, 5, 2308–2313, 2015.

[38] S. Sun, X. Yu, Q. Yang, Z. Yang, and S. Liang. Mesocrystals for photocatalysis: A comprehensive review on synthesis engineering and functional modifications. *Nanoscale Advances*, 1, 1, 34–63, 2019.

[39] S. J. Kim, I. Thomann, J. Park, J. H. Kang, A. P. Vasudev, and M. L. Brongersma. Light Trapping for Solar Fuel Generation with Mie Resonances. *Nano Letters*, 14, 3, 1446–1452, 2014.

[40] A. Ghobadi, T. G. Ulusoy Ghobadi, F. Karadas, and E. Ozbay. Semiconductor Thin Film Based Metasurfaces and Metamaterials for Photovoltaic and Photoelectrochemical Water Splitting Applications. *Advanced Optical Materials*, 7, 14, 1–39, 2019.

[41] X. Chen, L. Liu, P. Y. Yu, and S. S. Mao. Increasing Solar Absorption for Photocatalysis with Black Hydrogenated Titanium Dioxide Nanocrystals. *Science*, 331, 746–751, 2011.

[42] S. Assali, I. Zardo, S. Plissard, D. Kriegner, M. A. Verheijen, G. Bauer, A. Meijerink, A. Belabbes, F. Bechstedt, J. E. Haverkort, and E. P. Bakkers. Direct Band Gap Wurtzite Gallium Phosphide Nanowires. *Nano Letters*, 13, 4, 1559–1563, 2013.

[43] Y. C. Yen, J. A. Chen, S. Ou, Y. S. Chen, and K. J. Lin. Plasmon-Enhanced Photocurrent using Gold Nanoparticles on a Three-Dimensional TiO_2 Nanowire-Web Electrode. *Scientific Reports*, 7, 1–8, 2017.

[44] J. K. Kim, X. Shi, M. J. Jeong, J. Park, H. S. Han, S. H. Kim, Y. Guo, T. F. Heinz, S. Fan, C. L. Lee, J. H. Park, and X. Zheng. Enhancing Mo:$BiVO_4$ Solar Water Splitting with Patterned Au Nanospheres by Plasmon-Induced Energy Transfer. *Advanced Energy Materials*, 8, 5, 2018.

[45] www.freepik.com.

[46] J. Li, N. Verellen, and P. Van Dorpe. Engineering electric and magnetic dipole coupling in arrays of dielectric nanoparticles. *Journal of Applied Physics*, 123, 083101, 2018.

[47] L. Hüttenhofer, F. Eckmann, A. Lauri, J. Cambiasso, E. Pensa, Y. Li, E. Cortés, I. D. Sharp, and S. A. Maier. Anapole Excitations in Oxygen-Vacancy-Rich TiO_{2-x} Nanoresonators: Tuning the Absorption for Photocatalysis in the Visible Spectrum. *ACS Nano*, 14, 2, 2456–2464, 2020.

[48] J. H. Kennedy and K. W. Frese. Photooxidation of Water at α-Fe_2O_3 Electrodes. *Journal of The Electrochemical Society*, 125, 5, 709–714, 1978.

[49] A. Paracchino, N. Mathews, T. Hisatomi, M. Stefik, S. D. Tilley, and M. Grätzel. Ultrathin films on copper(I) oxide water splitting photocathodes: A study on performance and stability. *Energy and Environmental Science*, 5, 9, 8673–8681, 2012.

[50] H. Dotan, O. Kfir, E. Sharlin, O. Blank, M. Gross, I. Dumchin, G. Ankonina, and A. Rothschild. Resonant light trapping in ultrathin films for water splitting. *Nature Materials*, 12, 2, 158–164, 2013.

[51] S. Nishimura, N. Abrams, B. A. Lewis, L. I. Halaoui, T. E. Mallouk, K. D. Benkstein, J. Van de Lagemaat, and A. J. Frank. Standing Wave Enhancement of Red Absorbance and Photocurrent in Dye-Sensitized Titanium Dioxide Photoelectrodes Coupled to Photonic Crystals. *Journal of the American Chemical Society*, 125, 20, 6306–6310, 2003.

[52] J. I. Chen, G. Von Freymann, S. Y. Choi, V. Kitaev, and G. A. Ozin. Amplified Photochemistry with Slow Photons. *Advanced Materials*, 18, 14, 1915–1919, 2006.

[53] M. Curti, J. Schneider, D. W. Bahnemann, and C. B. Mendive. Inverse Opal Photonic Crystals as a Strategy to Improve Photocatalysis: Underexplored Questions. *Journal of Physical Chemistry Letters*, 6, 19, 3903–3910, 2015.

[54] N. I. Landy, S. Sajuyigbe, J. J. Mock, D. R. Smith, and W. J. Padilla. Perfect Metamaterial Absorber. *Physical Review Letters*, 100, 20, 1–4, 2008.

[55] C. M. Watts, X. Liu, and W. J. Padilla. Metamaterial Electromagnetic Wave Absorbers. *Advanced Materials*, 24, OP98–OP120, 2012.

[56] J. Hao, J. Wang, X. Liu, W. J. Padilla, L. Zhou, and M. Qiu. High performance optical absorber based on a plasmonic metamaterial. *Applied Physics Letters*, 96, 25, 10–13, 2010.

[57] F. Tan, N. Wang, D. Y. Lei, W. Yu, and X. Zhang. Plasmonic Black Absorbers for Enhanced Photocurrent of Visible-Light Photocatalysis. *Advanced Optical Materials*, 5, 2, 2017.

[58] W. Liu, J. Zhang, B. Lei, H. Hu, and A. E. Miroshnichenko. Invisible nanowires with interfering electric and toroidal dipoles. *Optics Letters*, 40, 10, 2293, 2015.

[59] Y. Wu, W. Yang, Y. Fan, Q. Song, and S. Xiao. TiO_2 metasurfaces: From visible planar photonics to photochemistry. *Science Advances*, 5, eaax0939, 2019.

[60] S. Kruk and Y. Kivshar. Functional Meta-Optics and Nanophotonics Governed by Mie Resonances. *ACS Photonics*, 4, 11, 2638–2649, 2017.

[61] I. Staude, A. E. Miroshnichenko, M. Decker, N. T. Fofang, S. Liu, E. Gonzales, J. Dominguez, T. S. Luk, D. N. Neshev, I. Brener, and Y. Kivshar. Tailoring directional scattering through magnetic and electric resonances in subwavelength silicon nanodisks. *ACS Nano*, 7, 9, 7824–7832, 2013.

[62] A. I. Kuznetsov, A. E. Miroshnichenko, M. L. Brongersma, Y. S. Kivshar, and B. Luk'yanchuk. Optically resonant dielectric nanostructures. *Science*, 354, 6314, 846, 2016.

[63] G. Grinblat, Y. Li, M. P. Nielsen, R. F. Oulton, and S. A. Maier. Enhanced Third Harmonic Generation in Single Germanium Nanodisks Excited at the Anapole Mode. *Nano Letters*, 16, 7, 4635–4640, 2016.

[64] A. Tittl, M. G. Harats, R. Walter, X. Yin, M. Schäferling, N. Liu, R. Rapaport, and H. Giessen. Quantitative Angle-Resolved Small-Spot Reflectance Measurements on Plasmonic Perfect Absorbers: Impedance Matching and Disorder Effects. *ACS Nano*, 8, 10, 10885–10892, 2014.

[65] A. E. Miroshnichenko, A. B. Evlyukhin, Y. F. Yu, R. M. Bakker, A. Chipouline, A. I. Kuznetsov, B. Luk'yanchuk, B. N. Chichkov, and Y. S. Kivshar. Nonradiating anapole modes in dielectric nanoparticles. *Nature Communications*, 6, 8069, 2015.

[66] S. Kment, P. Schmuki, R. Zboril, F. Riboni, S. Pausova, L. Wang, and L. Wang. Photoanodes based on TiO_2 and a-Fe_2O_3 for solar water splitting – superior role of 1D nanoarchitectures and of combined heterostructures. *Chemical Society Reviews*, 46, 3716–3769, 2017.

[67] A. Taflove and S. C. Hagndess. *Computational Electrodynamics*. Artech House, INC, Boston, London, 3rd editio edition, 2005.

[68] K. S. Yee. Numerical Solution of Initial Boundary Value Problems Involving Maxwell's Equation in Isotropic Media. *IEEE Transactions on Antennas and Propagation*, 14, 3, 302–307, 1966.

[69] B. Jean-Pierre. A Perfectly Matched Layer for the Absorption of Electromagnetic Waves. *Journal of Computational Physics*, 114, 2, 185–200, 1994.

[70] N. Rotenberg and L. Kuipers. Mapping nanoscale light fields. *Nature Photonics*, 8, 12, 919–926, 2014.

[71] G. Mie. Beiträge zur optik trüber Medien, speziell kolloidaler Metallösungen. *Annalen der Physik*, 3, 330, 377–445, 1908.

[72] C. F. Bohren and D. R. Huffman. *Absoprtion and Scattering of Light by Small Particles*. Wiley-VCH Verlag, 1983.

[73] W. Wiscombe. Mie scattering calculations: advances in techniques and fast, vector-speed computer codes. *(No. NCAR/TN-140+STR). University Corporation for Atmospheric Research.*, , June, 98, 1979.

[74] J. D. Jackson. *Classical Electrodynamics*. John Wiley and Sons, Inc„ 1999.

[75] E. E. Radescu and G. Vaman. Exact calculation of the angular momentum loss, recoil force, and radiation intensity for an arbitrary source in terms of electric, magnetic, and toroid multipoles. *Physical Review E*, 65, 4, 47, 2002.

[76] R. Wang and L. Dal Negro. Engineering non-radiative anapole modes for broadband absorption enhancement of light. *Optics Express*, 24, 17, 19048, 2016.

[77] W. B. Jackson, N. M. Amer, A. C. Boccara, and D. Fournier. Photothermal deflection spectroscopy and detection. *Applied Optics*, 20, 8, 1333–1344, 1981.

[78] M. I. Litter. Heterogeneous photocatalysis: Transition metal ions in photocatalytic systems. *Applied Catalysis B: Environmental*, 23, 2-3, 89–114, 1999.

[79] S.-I. Nishimoto, B. Ohtani, H. Kajiwara, and T. Kagiya. Photoinduced Oxygen Formation and Silver-metal Deposition in Aqueous Solutions of Various Silver Salts by Suspended Titanium Dioxide Powder. *Journal of the Chemical Society, Faraday Transactions 1*, 79, 2685–2694, 1983.

[80] Y. Oosawa and M. Gratzel. Effect of Surface Hydroxyl Density on Photocatalytic Oxygen Generation in Aqueous TiO_2 Suspensions. *Journal of the Chemical Society, Faraday Transactions 1*, 84, 1, 197–205, 1988.

[81] P. D. Fleischauer, H. K. Alan Kan, and J. R. Shepard. Quantum Yields of Silver Ion Reduction on Titanium Dioxide and Zinc Oxide Single Crystals. *Journal of the American Chemical Society*, 94, 1, 283–285, 1971.

[82] R. Quesada-Cabrera, C. Sotelo-Vazquez, J. C. Bear, J. A. Darr, and I. P. Parkin. Photocatalytic Evidence of the Rutile-to-Anatase Electron Transfer in Titania. *Advanced Materials Interfaces*, 1, 1400069, 2014.

[83] X. Shi, L. Cai, M. Ma, X. Zheng, and J. H. Park. General Characterization Methods for Photoelectrochemical Cells for Solar Water Splitting. *ChemSusChem*, 8, 19, 3192–3203, 2015.

[84] R. Memming. *Semiconductor Electrochemistry*. Wiley-VCH Verlag, 2nd edition, 2015.

[85] K. Hashimoto, H. Irie, and A. Fujishima. TiO_2 Photocatalysis: A Historical Overview and Future Prospects. *Japanese Journal of Applied Physics*, 44, 12, 8269–8285, 2006.

[86] X. Chen, L. Liu, and F. Huang. Black titanium dioxide (TiO_2) nanomaterials. *Chemical Society Reviews*, 44, 7, 1861–1885, 2015.

[87] S. G. Ullattil, S. B. Narendranath, S. C. Pillai, and P. Periyat. Black TiO_2 Nanomaterials: A Review of Recent Advances. *Chemical Engineering Journal*, 343, 708–736, 2018.

[88] S. Ben-Jaber, W. J. Peveler, R. Quesada-Cabrera, E. Cortés, C. Sotelo-Vazquez, N. Abdul-Karim, S. A. Maier, and I. P. Parkin. Photo-induced enhanced Raman spectroscopy for universal ultra-trace detection of explosives, pollutants and biomolecules. *Nature Communications*, 7, 12189, 2016.

[89] X. Pan, M. Q. Yang, X. Fu, N. Zhang, and Y. J. Xu. Defective TiO_2 with oxygen vacancies: Synthesis, properties and photocatalytic applications. *Nanoscale*, 5, 9, 3601–3614, 2013.

[90] A. Sarkar and G. G. Khan. The formation and detection techniques of oxygen vacancies in titanium oxide-based nanostructures. *Nanoscale*, 11, 3414–3444, 2019.

[91] J. S. T. Gongora, A. E. Miroshnichenko, Y. S. Kivshar, and A. Fratalocchi. Anapole nanolasers for mode-locking and ultrafast pulse generation. *Nature Communications*, 8, 15535, 2017.

[92] D. Glass, E. Cortés, S. Ben-jaber, T. Brick, W. J. Peveler, C. S. Blackman, C. R. Howle, R. Quesada-Cabrera, I. P. Parkin, and S. A. Maier. Dynamics of Photo-Induced Surface Oxygen Vacancies in Metal-Oxide Semiconductors Studied Under Ambient Conditions. *Advanced Science*, 6, 1901841, 2019.

[93] S. Sahoo, A. K. Arora, and V. Sridharan. Raman Line Shapes of Optical Phonons of Different Symmetries in Anatase TiO_2 Nanocrystals. *Journal of Physical Chemistry C*, 113, 39, 16927–16933, 2009.

[94] J. Yan, G. Wu, N. Guan, L. Li, Z. Li, and X. Cao. Understanding the effect of surface/bulk defects on the photocatalytic activity of TiO_2: anatase versus rutile. *Physical Chemistry Chemical Physics*, 15, 10978–10988, 2013.

[95] G. Nagaraj, R. A. Senthil, and K. Ravichandran. Firmness and bandgap engineered anatase TiO_2 nanoparticles for enhanced visible light photocatalytic activity. *Materials Research Express PAPER*, 6, 095049, 2019.

[96] J. Park, S. K. Ozdemir, F. Monifi, T. Chadha, and S. H. Huang. Titanium Dioxide Whispering Gallery Microcavities. *Advanced Optical Materials*, 2, 711–717, 2014.

[97] G. Grinblat, Y. Li, M. P. Nielsen, R. F. Oulton, and S. A. Maier. Efficient Third Harmonic Generation and Nonlinear Subwavelength Imaging at a Higher-Order Anapole Mode in a Single Germanium Nanodisk. *ACS Nano*, 11, 1, 953–960, 2017.

[98] Y. Yang, V. A. Zenin, and S. I. Bozhevolnyi. Anapole-Assisted Strong Field Enhancement in Individual All-Dielectric Nanostructures. *ACS Photonics*, 5, 5, 1960–1966, 2018.

[99] S. Xu and E. A. Carter. 2-Pyridinide as an Active Catalytic Intermediate for CO_2 Reduction on p-GaP Photoelectrodes: Lifetime and Selectivity. *Journal of the American Chemical Society*, 140, 8732–8738, 2018.

[100] E. E. Barton, D. M. Rampulla, and A. B. Bocarsly. Selective Solar-Driven Reduction of CO_2 to Methanol Using a Catalyzed p-GaP Based Photoelectrochemical Cell. *Journal of the American Chemical Society*, 130, 20, 6342–6344, 2008.

[101] M. Levinshtein, S. Rumyantsev, and M. Shur. Handbook Series on Semiconductor Parameters. volume 1, pages 104–124. World Scientific Publishing Co. Pte. Ltd., London, 1996.

[102] J. K. Cooper, S. Gul, F. M. Toma, L. Chen, Y.-s. Liu, J. Guo, J. W. Ager, J. Yano, and I. D. Sharp. Indirect Bandgap and Optical Properties of Monoclinic Bismuth Vanadate. *Journal of Physical Chemistry C*, 119, 2969–2974, 2015.

[103] I. D. Sharp, J. K. Cooper, F. M. Toma, and R. Buonsanti. Bismuth Vanadate as a Platform for Accelerating Discovery and Development of Complex Transition-Metal Oxide Photoanodes. *ACS Energy Letters*, 2, 139–150, 2017.

[104] G. Jellison Jr. Optical functions of GaAs, GaP, and Ge determined by two-channel polarization modulation ellipsometry. *Optical Materials*, 1, 151–160, 1992.

[105] D. Cristea, D. Constantin, A. Crisan, C. S. Abreu, J. R. Gomes, N. P. Barradas, E. Alves, C. Moura, F. Vaz, and L. Cunha. Properties of tantalum oxynitride thin films produced by magnetron sputtering: The influence of processing parameters. *Vaccum*, 98, 100, 63–69, 2013.

[106] L. Hüttenhofer, A. Tittl, L. Kühner, E. Cortés, and S. A. Maier. Anapole-Assisted Absorption Engineering in Arrays of Coupled Amorphous Gallium Phosphide Nanodisks. *ACS Photonics*, 8, 1469–1476, 2021.

[107] N. Kooy, K. Mohamed, L. T. Pin, and O. S. Guan. A review of roll-to-roll nanoimprint lithography. *Nanoscale Research Letters*, 9, 1, 1–13, 2014.

[108] B. Ai, H. Möhwald, D. Wang, and G. Zhang. Advanced Colloidal Lithography Beyond Surface Patterning. *Advanced Materials Interfaces*, 4, 1600271, 2017.

[109] W. B. Jung, S. Jang, S. Y. Cho, H. J. Jeon, and H. T. Jung. Recent Progress in Simple and Cost-Effective Top-Down Lithography for 10 nm Scale Nanopatterns: From Edge Lithography to Secondary Sputtering Lithography. *Advanced Materials*, 32, 35, 1–22, 2020.

[110] S. M. Choudhury, D. Wang, K. Chaudhuri, C. Devault, A. V. Kildishev, A. Boltasseva, and V. M. Shalaev. Material platforms for optical metasurfaces. *Nanophotonics*, 7, 6, 959–987, 2018.

[111] O. Quevedo-Teruel, H. Chen, A. Díaz-Rubio, G. Gok, A. Grbic, G. Minatti, E. Martini, S. Maci, G. V. Eleftheriades, M. Chen, N. I. Zheludev, N. Papasimakis, S. Choudhury, Z. A. Kudyshev, S. Saha, H. Reddy, A. Boltasseva, V. M. Shalaev, A. V. Kildishev, D. Sievenpiper, C. Caloz, A. Al, Q. He, L. Zhou, G. Valerio, E. Rajo-Iglesias, Z. Sipus, F. Mesa, R. Rodríguez-Berral, F. Medina, V. Asadchy, S. Tretyakov, and C. Craeye. Roadmap on metasurfaces. *Journal of Optics*, 21, 073002, 2019.

[112] O. Yavas, M. Svedendahl, P. Dobosz, V. Sanz, and R. Quidant. On-a-chip Biosensing Based on All-Dielectric Nanoresonators. *Nano Letters*, 17, 7, 4421–4426, 2017.

[113] V. E. Babicheva and J. V. Moloney. Lattice effect on electric and magnetic resonance overlap in periodic array. *Nanophotonics*, 7, 10, 1663–1668, 2018.

[114] V. Mazzone, J. S. T. Gongora, and A. Fratalocchi. Near-field coupling and mode competition in multiple anapole systems. *Applied Sciences (Switzerland)*, 7, 542, 2017.

[115] H. Hasebe, H. Sugimoto, T. Hinamoto, and M. Fujii. Coupled Toroidal Dipole Modes in Silicon Nanodisk Metasurface: Polarization Independent Narrow Band Absorption and Directional Emission. *Advanced Optical Materials*, 8, 22, 1–9, 2020.

[116] J. Cambiasso, G. Grinblat, Y. Li, A. Rakovich, E. Cortés, and S. A. Maier. Bridging the Gap between Dielectric Nanophotonics and the Visible Regime with Effectively Lossless Gallium Phosphide Antennas. *Nano Letters*, 17, 2, 1219–1225, 2017.

[117] B. Tilmann, G. Grinblat, R. Berté, M. Özcan, V. F. Kunzelmann, B. Nickel, I. D. Sharp, E. Cortés, S. A. Maier, and Y. Li. Nanostructured amorphous gallium phosphide on silica for nonlinear and ultrafast nanophotonics. *Nanoscale Horizons*, 5, 11, 1500–1508, 2020.

[118] S. Bagheri, K. Weber, T. Gissibl, T. Weiss, F. Neubrech, and H. Giessen. Fabrication of Square-Centimeter Plasmonic Nanoantenna Arrays by Femtosecond Direct Laser Writing Lithography: Effects of Collective Excitations on SEIRA Enhancement. *ACS Photonics*, 2, 6, 779–786, 2015.

[119] V. G. Kravets, A. V. Kabashin, W. L. Barnes, and A. N. Grigorenko. Plasmonic Surface Lattice Resonances: A Review of Properties and Applications. *Chemical Reviews*, 118, 12, 5912–5951, 2018.

[120] A. Abass, S. R. K. Rodriguez, J. Gómez Rivas, and B. Maes. Tailoring Dispersion and Eigenfield Profiles of Plasmonic Surface Lattice Resonances. *ACS Photonics*, 1, 1, 61–68, 2014.

[121] M. E. Nasir, A. V. Krasavin, R. M. Córdova-Castro, C. P. T. McPolin, J. G. Bouillard, P. Wang, and A. V. Zayats. Mode Engineering in Large Arrays of Coupled Plasmonic–Dielectric Nanoantennas. *Advanced Optical Materials*, 9, 2001467, 2021.

[122] B. Lamprecht, G. Schider, R. T. Lechner, H. Ditlbacher, J. R. Krenn, A. Leitner, and F. R. Aussenegg. Metal Nanoparticle Gratings: Influence of Dipolar Particle Interaction on the Plasmon Resonance. *Physical Review Letters*, 84, 20, 4721–4724, 2000.

[123] M. Meier, P. F. Liao, and A. Wokaun. Enhanced fields on rough surfaces: dipolar interactions among particles of sizes exceeding the Rayleigh limit. *Journal of the Optical Society of America B*, 2, 6, 931, 1985.

[124] M. Quinten, A. Leitner, J. R. Krenn, and F. R. Aussenegg. Electromagnetic energy transport via linear chains of silver nanoparticles. *Optics Letters*, 23, 17, 1331, 1998.

[125] S. A. Maier and H. A. Atwater. Plasmonics: Localization and guiding of electromagnetic energy in metal/dielectric structures. *Journal of Applied Physics*, 98, 1, 1–10, 2005.

[126] L. Hüttenhofer, M. Golibrzuch, O. Bienek, F. J. Wendisch, R. Lin, M. Becherer, I. D. Sharp, S. A. Maier, and E. Cortés. Metasurface Photoelectrodes for Enhanced Solar Fuel Generation. 2102877, 2021.

[127] S. Deng, B. Zhang, P. Choo, P. J. Smeets, and T. W. Odom. Plasmonic Photoelectrocatalysis in Copper-Platinum Core-Shell Nanoparticle Lattices. *Nano Letters*, 21, 3, 1523–1529, 2021.

[128] J. Sun, C. Liu, and P. Yang. Surfactant-Free, Large-Scale, Solution-Liquid-Solid Growth of Gallium Phosphide Nanowires and Their Use for Visible-Light-Driven Hydrogen Production from Water Reduction. *Journal of the American Chemical Society*, 133, 48, 19306–19309, 2011.

[129] G. F. Moore and I. D. Sharp. A Noble-Metal-Free Hydrogen Evolution Catalyst Grafted to Visible Light-Absorbing Semiconductors. *Journal of Physical Chemistry Letters*, 4, 4, 568–572, 2013.

[130] A. Krawicz, J. Yang, E. Anzenberg, J. Yano, I. D. Sharp, and G. F. Moore. Photofunctional Construct That Interfaces Molecular Cobalt-Based Catalysts for H_2 Production to a Visible-Light-Absorbing Semiconductor. *Journal of the American Chemical Society*, 135, 32, 11861–11868, 2013.

[131] K. Song, H. Lee, M. Lee, and J. Y. Park. Plasmonic Hot Hole-Driven Water Splitting on Au Nanoprisms/P-Type GaN. *ACS Energy Letters*, 6, 4, 1333–1339, 2021.

[132] X. Shi, K. Ueno, T. Oshikiri, Q. Sun, K. Sasaki, and H. Misawa. Enhanced water splitting under modal strong coupling conditions. *Nature Nanotechnology*, 13, 10, 953–958, 2018.

[133] J. S. Duchene, G. Tagliabue, A. J. Welch, W. H. Cheng, and H. A. Atwater. Hot Hole Collection and Photoelectrochemical CO_2 Reduction with Plasmonic Au/p-GaN Photocathodes. *Nano Letters*, 18, 4, 2545–2550, 2018.

[134] A. Manjavacas, N. J. Halas, M. McClain, B. Y. Zheng, H. Zhao, and P. Nordlander. Distinguishing between plasmon-induced and photoexcited carriers in a device geometry. *Nature Communications*, 6, 8797, 2015.

[135] R. D. Nagel, T. Haeberle, M. Schmidt, P. Lugli, and G. Scarpa. Large Area Nanotransfer Printing of Sub-50-nm Metal Nanostructures Using Low-cost Semi-flexible Hybrid Templates. *Nanoscale Research Letters*, 11, 143, 2016.

[136] S. H. Ahn and L. J. Guo. Large-area roll-to-roll and roll-to-plate Nanoimprint Lithography: A step toward high-throughput application of continuous nanoimprinting. *ACS Nano*, 3, 8, 2304–2310, 2009.

[137] A. Canós Valero, E. A. Gurvitz, F. A. Benimetskiy, D. A. Pidgayko, A. Samusev, A. B. Evlyukhin, V. Bobrovs, D. Redka, M. I. Tribelsky, M. Rahmani, K. Z. Kamali, A. A. Pavlov, A. E. Miroshnichenko, and A. S. Shalin. Theory, Observation, and Ultrafast Response of the Hybrid Anapole Regime in Light Scattering. *Laser and Photonics Reviews*, , 2100114, 2021.

[138] L. Bonacina, P. F. Brevet, M. Finazzi, and M. Celebrano. Harmonic generation at the nanoscale. *Journal of Applied Physics*, 127, 23, 2020.

[139] J. He, P. Gao, Z. Yang, J. Yu, W. Yu, Y. Zhang, J. Sheng, J. Ye, J. C. Amine, and Y. Cui. Silicon/Organic Hybrid Solar Cells with 16.2% Efficiency and Improved Stability by Formation of Conformal Heterojunction Coating and Moisture-Resistant Capping Layer. *Advanced Materials*, 29, 15, 1–7, 2017.

[140] H. Kim, C. M. Gilmore, A. Piqué, J. S. Horwitz, H. Mattoussi, H. Murata, Z. H. Kafafi, and D. B. Chrisey. Electrical, optical, and structural properties of indium-tin-oxide thin films for organic light-emitting devices. *Journal of Applied Physics*, 86, 11, 6451–6461, 1999.

[141] M. Alqahtani, S. Ben-Jabar, M. Ebaid, S. Sathasivam, P. Jurczak, X. Xia, A. Alromaeh, C. Blackman, Y. Qin, B. Zhang, B. S. Ooi, H. Liu, I. P. Parkin, and J. Wu. Gallium Phosphide photoanode coated with TiO_2 and CoO_x for stable photoelectrochemical water oxidation. *Optics Express*, 27, 8, A364–A371, 2019.

[142] S. Hu, N. S. Lewis, J. W. Ager, J. Yang, J. R. McKone, and N. C. Strandwitz. Thin-Film Materials for the Protection of Semiconducting Photoelectrodes in Solar-Fuel Generators. *Journal of Physical Chemistry C*, 119, 43, 24201–24228, 2015.

Acknowledgments

My first and biggest thanks goes to my supervisor **Prof. Stefan A. Maier**. I appreciated his confidence in me to conduct the moving of the chair from London to the Nanoinstitut from the Munich end as well as his strengthening of my necessary self-confidence for the vibrant discussions in the "Baumeetings". I also enjoyed his fashion of supervising my scientific projects, in particular his right balance between encouragement and freedom. I could rely on his advice and he always had a sympathetic ear when needed.
I equally want to thank **Prof. Emiliano Cortés** for his complementary supervision with hands-on recommendations in the laboratory and for the handling of the daily business as a PhD student.
I also enjoyed the fruitful collaboration with the group of **Prof. Ian D. Sharp**, for which I want to greatly thank him. I was very happy to have him as a "secret supervisor" as he gave me extremely valuable suggestions during my first and third project, and shared his unexpected knowledge about nail polish. Special thanks also goes to his PhDs **Felix Eckmann** and **Oliver Bienek**.
I want to express huge thanks **Matthias Golibrzuch** from TU München for being the imprinter in chief.
My next acknowledgment goes to **Prof. Yi Li**, **Dr. Fedja J. Wendisch** and **Dr. Andreas Tittl** for supporting me on the way to publishing my results.
I want to thank my colleagues **Andrea Mancini**, **Benjamin Tilmann**, **Matías Herran** and **Lucca Kühner** for the vibrant scientific exchange and the celebrations once something in the lab finally worked out or even got published, and also if not. A special thanks goes to **Simone Ezendam** who was willing to share with me the pleasures of being IT administrator of the chair.
As I learned, handling research projects is a tricky task. But it is *as* tricky to handle researchers. This was greatly achieved by **Namvar Jahanmehr**, **Reinhold Rath** and **Martina Edenhofer**, to which I want to thank.
I also want to acknowledge the help of **Christian Obermayer** and **Philipp Altpeter** from the Kotthaus chair for supporting me with sample processing and valuable tips for recipes for nanofabrication.
Least, great thanks go to my friends and family for the persistent encouragement and necessary distractions, especially to my girlfriend Sonja Lachenmayr.